University of Alberta

TUMOR INVASION MARGIN FROM DIFFUSION WEIGHTED IMAGING

by

Parisa Mosayebi

A thesis submitted to the Faculty of Graduate Studies and Research
in partial fulfillment of the requirements for the degree of

Master of Science

Department of Computing Science

Spring 2010
Edmonton, Alberta

Examining Committee

Martin Jagersand, Computing Science

Dana Cobzas, Computing Science

External, Thomas Hillen, Mathematical and Statistical Sciences

Examiner 2, Russell Greiner, Computing Science

To my parents and my family for their love, inspiration, wisdom and guidance.

Abstract

Glioma is one of the most challenging types of brain tumors to be treated or controlled locally. One of the main problems is to determine which areas of the apparently normal brain contain glioma cells, as gliomas are known to infiltrate several centimetres beyond the clinically apparent lesion that is visualized on standard CT or MRI. To ensure that radiation treatment encompasses the whole tumor, including the cancerous cells not revealed by MRI, doctors treat the volume of brain that extends 2cm out from the margin of the visible tumor. This approach does not consider varying tumor-growth dynamics in different brain tissues, thus it may result in killing some healthy cells while leaving cancerous cells alive in other areas. These cells may cause recurrence of the tumor later in time which limits the effectiveness of the therapy.

In this thesis, we propose two models to define the tumor invasion margin based on the fact that glioma cells preferentially spread along nerve fibers. The first model is an anisotropic reaction-diffusion type tumor growth model that prioritizes diffusion along nerve fibers, as given by DW-MRI data. The second proposed approach computes the tumor invasion margin using a geodesic distance defined on the Riemannian manifold of brain fibers. Both mathematical models result in Partial Differential Equations (PDEs) that have to be numerically solved. Numerical methods used for solving differential equations should be chosen with great care. A part of this thesis is dedicated to discuss in detail, the numerical aspects such as stability and consistency of different finite difference methods used to solve these PDEs. We review the stability issues of several 2D methods that discretize the anisotropic diffusion equation and we propose an extension of one 2D stable method to 3D. We also analyze the stability issues of the geodesic model. In comparison, the geodesic model is numerically more stable than the anisotropic diffusion model since it results in a first-order PDE. Finally, we evaluate both models on actual DTI data from patients with glioma by comparing our predicted growth with follow-up MRI scans. Results show improvement in predicting the invasion margin when using the geodesic distance model as opposed to the 2cm conventional Euclidean distance.

Acknowledgements

I would like to express my sincere appreciation and gratitude to Dr. Dana Cobzas and Dr. Martin Jagersand for their supervision and constant support during my studies and in developing this thesis. I also acknowledge all members of the Brain Tumor Analysis Project (BTAP), Dr. Russ Greiner, Dr. Albert Murtha, Dr. Jörg Sanders and Bret Hohen for their useful inputs on my research. Thanks also go to all members of my research group and friends particularly Neil Birckbeck, Karteek Popuri and David Israel. It was really a pleasure working and learning side by side of them.

Parisa Mosayebi
Edmonton, AB, Canada
January 2010

Table of Contents

List of Tables

List of Figures

Chapter 1

Introduction

Primary brain tumors are tumors that start from a glial cell in the nervous system. High grade variations of these tumors grow very fast, often leading to a life-threatening condition. Current imaging techniques such as Computer Tomography (CT) or Magnetic Resonance Imaging (MRI) detect only the part of the tumor with a high concentration of tumor cells. The conventional medical practice is to perform maximally safe surgical resection and then irradiate the remaining tumor cells (visible and occult). The radiotherapy is conventionally applied to a margin of about 2cm around the visible tumor, which is a very rough approximation of the probable location of occult tumor cells. This approach does not consider tumor growth dynamics in different brain tissues, thus it may result in killing some healthy cells while leaving alive cancerous cells in other areas. These cells may cause re-occurrence of the tumor later in time, which limits the effectiveness of the therapy. To improve the therapeutic outcome, more accurate prediction of the tumor invasion margin is necessary. The question that we intend to answer in this thesis is: *How can we define this invisible extension based on the visible part of the tumor by applying mathematical models to patient data?*

Mathematical models are made based on a solid knowledge of physical and biological behaviour of tumor growth process. The physical behaviour of glioblastoma growth leads to a well known mathematical formulation, the Reaction-Diffusion (RD) equation. Solving this equation is the main focus of most studies in the area of glioma modeling. Based on the generally accepted belief, glioma cells preferentially spread along nerve fibers [64]. Incorporating this belief into mathematical modeling is a fairly new idea, which makes use of a certain type of imaging technique, Diffusion Weighted Magnetic Resonance Imaging (DW-MRI). The first step of this thesis solves the Reaction-Diffusion equation in a numerically stable manner, taking into account the nerve fiber direction determined by using DW-MRI data. This solution is then used to find the tumor invasion margin.

In the second part, we propose a new approach for computing the tumor invasion margin that makes use of a geodesic distance defined on a manifold of brain fibers. This formulation is very easily transferable to radiation therapy software by replacing the uniform (Euclidean) distance currently used to define the 2cm invasion margin (that will be radiated) with the geodesic distance. Both mathematical models result in Partial Differential Equations (PDEs) that are then numerically solved. Numerical

methods used for solving differential equations should be chosen with great care. A part of this thesis is dedicated to discuss, in detail, the numerical aspects such as stability and consistency of finite difference methods used to solve these PDEs. Finally, we evaluate the proposed models on real patient DWI data, which is a major contribution compared to previous works that were only evaluated on synthetic data or one real datum. We summarize the main contributions of this thesis as follows:

- Introducing the use of geodesic distance on the Riemannian manifold of brain fibers to replace the Euclidean distance used in clinical practice to identify the tumor invasion margin [14].
- Assessing the numerical aspects of different finite difference methods used to solve the final PDEs of geodesic distance and anisotropic diffusive models. Also, extending a 2D stable method of solving the anisotropic parabolic diffusion equation to 3D and defining the stability conditions.
- Evaluating the proposed models on real DTI data of several patients. While all the existing models in literature are either tested on synthetic data or on one real data set ([36], [13], [40]), this is the first time that the models are evaluated on data from multiple patients.

1.1 Organization of the Thesis

This thesis addresses the problem of finding the brain tumor invasion margin from MRI and DTI data of patients. We start from a general description about different types of brain tumors and specifications of gliomas. We follow by providing information about diffusion weighted imaging technique and also tumor appearance in MRI images. After a review on existing models on tumor growth modeling, we present our new approaches to define the tumor invasion margin. Stability issues of numerical methods used in our mathematical formulations is further assessed in detail. Finally, we apply our models on synthetic data and several real datasets and compare the result with ground truth. A more detailed description of the material covered in each chapter is given below.

Chapter 2: In this chapter, we first provide some information about different classes of brain tumors and tumor characteristics in each class. The focus of this project is on a particular type of glioma called glioblastoma multiforme. The shortcomings of current methods of glioblastoma treatment and suggestions for improvements are discussed after. In the rest of the chapter, we will explain two fundamental brain tumor imaging techniques, MRI and Diffusion Weighted MRI. MRI provides information about the brain geometry, tissues and tumor location. DW-MRI, which is relatively a new technique, provides information about the motility of water molecules which in turn is used to define diffusion of tumor cells. The tumor appearance in different MRI modalities and parameters extracted from DW-MRI data are other material discussed in this chapter.

Chapter 3: In this chapter, we provide an overview on mathematical modeling of brain tumor growth. The numerous approaches in the literature can be classified based in different taking into account the scale of model, the main medical and biological focus of the model and the degree of complexity of each model. The most conventional classification, which is based on the scale of observation, classifies the models in literature into two general microscopic and macroscopic categories. Models using medical images as observation are classified under the macroscopic class. Each class is in turn subdivided into subclasses. This area of research is vast and our goal in this chapter is to highlight only those approaches that are most relevant to our project.

Chapter 4: In this chapter, we propose the theory and mathematical formulation of two different tumor growth models for defining the tumor invasion margin. The first model is based on solving the general reaction-diffusion equation with a stable numerical method. The resulting tumor cell density map is used to define the isocontours of same concentration around the tumor. These isocontours correspond to the later time tumor delineation area observed in MRI images. Our other proposed method links the tumor diffusion to a Riemannian manifold on brain fibers and defines the isocontours of tumor growth as geodesic distances on the manifold. We also survey different functions used in literature to map water diffusion tensors to tumor diffusion tensors and introduce our new approach of mapping.

Chapter 5: In this chapter, the numerical aspects of solving partial differential equations (PDEs) is discussed in details. PDEs are the final equations of our proposed tumor growth mathematical modeling. Numerical methods should be chosen with great care and not considering certain aspects such as stability, consistency and wellposed-ness would result in erroneous solutions. Our first growth model, the anisotropic diffusive approach results in second order parabolic PDE. Special conditions should be satisfied to guaranty the spatial stability of this kind of PDE. We will extend an existing 2D discretization model to obtain a stable 3D one. The other growth model, the Geodesic distance on Riemannian manifolds, ends in a first order hyperbolic differential equation. In contrast to parabolic PDEs, this PDE is well studied in literature and stable discretization models are available for that. We finally compare the two models taking into account the numerical issues.

Chapter 6: In this final chapter, we evaluate our proposed methods of finding the tumor invasion margin and the stability issues of each model using synthetic and real data. First, we validate the stability issues of numerical methods given in Chapter 5 for solving second-order parabolic PDE. For this mean, we generate a variety of synthetic 2D and 3D test models. The examples are ordered from easy to difficult to test where each model gets instable. The second part of the chapter describes a system for validating both geodesic and anisotropic diffusive models given in Chapter 4 on real patient DTI data. The validation procedures include some pre-processing steps such as seg-

mentation, registration and tensor extraction followed by the main simulation process. The results of simulations are then compared visually and numerically with the ground truth (patient data). We explain each of these steps in details in this chapter.

Chapter 2

Review of Brain Tumors and Medical Imaging

2.1 Introduction

To improve the treatment of glioma tumor, a clear definition of the tumor growth process and the problems of current treatment methods is necessary. To address these issues, in this chapter, we first explain different categories of brain tumors and tumor characteristics in each category. The focus of this project is on a particular type of glioma called glioblastoma multiforme. The shortcomings of current treatment methods of glioblastoma and also suggestion for improvements are discussed after. The rest of the chapter is dedicated to explain brain tumor imaging techniques. For the case of brain tumors, the two core imaging methods are MRI and Diffusion Weighted MRI. MRI provides information about the brain geometry, different tissues and tumor location. DW-MRI, which is relatively a new technique, provides information about the motility of water molecules which in turn is used to define diffusion of tumor cells.

2.2 Brain Tumors

Brain tumors are divided into two categories based on their origin and degree of aggressiveness. In terms of aggressiveness, brain tumors are classified in two groups of *benign* and *malignant*. *Benign* brain tumors grow very slowly and they rarely infiltrate into the surrounding tissue. They are usually completely removed by surgery, due to the distinct borders between them and the brain tissue. On the other hand, *malignant* tumors grow rapidly and infiltrate to the surrounding healthy tissues. Their invasive behaviour prevents a complete removal by surgery. Moreover, their cells can travel through cerebrospinal fluid to other parts of the brain [6]. In terms of origin, brain tumors are divide into two groups of *primary* and *metastatic*. *Primary* brain tumors start from the brain and remain in the brain. They usually occur in children and older adults. *Metastatic* brain tumors are formed by cancerous cells that have traveled to the brain from another part of the body. The majority of brain tumors of this type are metastasized to the brain from a lung or breast cancer [18]. They are the most

common brain tumors and by nature *malignant*. The most commonly used grading system proposed by World Health Organization (WHO) categorizes tumors into four groups:

1. Grade I : Slow proliferation, cells look like normal, long survival rate
2. Grade II : Relatively slow proliferation, cells look like almost normal, may invade, may recur as grade II or higher grades
3. Grade III : Rapidly producing, cells look like normal, vascular proliferation, invade surrounding tissue, tends to recur
4. Grade IV: Very rapid proliferation, very abnormal appearance of cells, invade to large areas, recurs, necrotic core, forms new vascularisation to support growth.

The grading is based on different factors including mitotic index, vascularity, and presence of necrotic core, invasion potential and similarity to normal cells. This kind of grading helps to expedite prognosis and therapy planning.

2.2.1 Gliomas

Gliomas are the most common *primary* tumor of the brain. Gliomas start from glial cells that protect and nourish nerve cells in the central nervous system. The cause of this type of tumor is still unknown and the only so far identified risk is ionizing radiations [18]. Gliomas have a variety of grades and rates of aggressiveness. They are typically subdivided into low grade *benign* gliomas (i.e. grade I and II) or high-grade *malignant* gliomas (i.e. grade III or IV). Grade I gliomas named piolcytic astrocytomas belong to the circumscribed category and are different from the three other grades. They do not infiltrate into the surrounding tissue and grow very slowly. This type of tumor is usually seen among children and is curable in most cases [6]. Higher grade gliomas (grade II to IV) are tumors of adult patients and share common characteristics. They belong to the diffuse category since they invade into the healthy neighbouring brain tissue. Grade II gliomas grow slowly but they tend to progress into high grade tumors despite therapy. Studies show that they return in the format of highly invasive tumors (grade IV) after 5 to 10 years of the original diagnosis and subsequent treatments.

Grade III (anaplastic astrocytomas) and grade IV gliomas (glioblastoma multiforme) grow very fast and infiltrates to the brain parenchyma. Both types are usually surrounded by edema and the grade IV forms a network of blood vessels and a necrotic core. Due to the high growth rate of glioblastoma, tumor cells compete for nutrition and oxygen. They get the necessary nutrition from the periphery. The cells in the center of the tumor get less amount of nutrition in the competition and start to die. The dead cells form a necrotic area which is only observed in grade IV gliomas. In addition, due the high demand for nutrition, tumor needs more blood flow. So it starts the process of forming new network of blood vessels which is called vascularisation. Vascularisation is the second feature

of glioblastoma. Also, glioblastoma are usually surrounded by extensive amount of fluid called vasogenic edema. The rapid growth and the edema exert pressure to the brain tissue, which results in their compression against skull. This compression causes local deformation of the tissue called mass effect [60] [6].

Diffusive gliomas infiltrate into the neighbouring tissues. Tumor cells diffuse mostly in white matter fibers but they also diffuse into cerebrospinal fluid and the vascular conduits [6]. Study shows that although they rise from white matter, but they can infiltrate into gray matter as well. However, the rate of the growth in gray matter is lower. A glioblastoma can also diffuse to the adjacent hemisphere of the brain through the corpus callosum. Tumors of this case have a symmetric shape which resembles a butterfly and are commonly referred to as butterfly gliomas [60].

2.2.2 Gliomas Therapy

The treatment of gliomas include surgery, radiation therapy and chemotherapy [53]. In this project, we mainly focus on treatment of grade IV gliomas (glioblastoma), which is a fairly difficult task. The first step of treatment is to apply maximally safe surgical extraction. But, the total resection of the tumor is not possible due to the infiltrative behaviour of gliomas. Therefore, the process is followed by high dose radiotherapy and supplementary chemotherapy. Despite this aggressive approach, the reported median survival is only 14.6 months [24], although a percentage of patients may survive more than 5 years. Those patients who choose only supportive therapy usually survive for only a few weeks to months.

In contrast to most fatal malignancies that belong to *metastatic* type of tumors, gliomas are *primary* tumors and they remain in the brain. So if we can locally control the tumor growth, we may directly impact the rate of survival of patients. In addition, any improvement in local control can certainly improve the quality of life of patients since it prevents or delays the subsequent neurological deterioration associated with uncontrolled disease. Therefore any effort to make an improvement in control of glioma is of great value. An effective step to improve glioma control is to better localize the radiation therapy.

Gliomas infiltrate for several centimetres beyond the clinically apparent lesion visualized on standard CT or MRI. If these infiltrated cells are not destroyed timely, they will divide into new cells and diffuse to other tissues which will result in tumor recurrence and growth. Radiation therapy is an effective non-invasive method to attack these infiltrated cells. State of the art techniques, such as intensity modulated radiation therapy (IMRT) or proton therapy, have vastly improved the ability to deliver sophisticated treatments. These technologies enable radiation oncologists to apply extremely high doses to identified targets, while still respecting the radiation tolerances of adjacent critical regions. This advantage is particularly important in the brain, where the identified target is often separated from other critical regions by only a few millimetres. Although these new technologies enable radiation oncologists to apply delicate treatment, the lack of knowledge on ”where” the

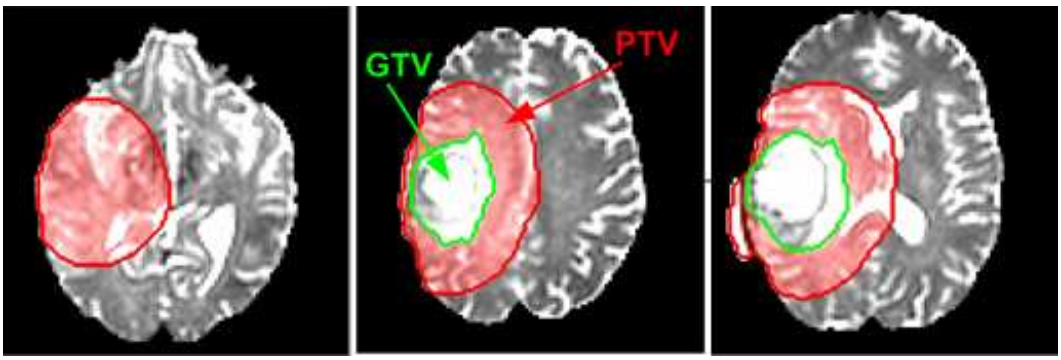

Figure 2.1: Gross Tumor Volume and planning Target Volume. Slices from an MRI T2 scan showing the gross tumor volume (GTV) in green, which together with the 2cm margin forms the planning target volume (PTV) to be radiated. The PTV is about $500cm^3$, representing 27% of the total brain and about 4 times more than the visible GTV.

infiltrated tumors reside prevents utilizing the full capacity of these new tools.

In conventional therapy, the radiation target consists of the gross tumor volume (GTV) which is the apparent lesion identified in standard computer tomography (CT) or magnetic resonance imaging (MRI) scan, and a 2cm margin around GTV known as the planning target volume (PTV), which accounts for infiltrated occult cells. Figure 2.1 shows these two volumes. This additional margin results in a PTV, which is often 4 or more times the volume of the original GTV. Figure 2.1 provides a good illustration of how large PTV is compared to GTV. Hence, PTV usually incorporates a large number of critical brain regions and applying radiation to these regions can result in irrecoverable damage. The conventional approach of adding a 2 cm Euclidean margin to the GTV to construct a PTV is based on limited and specific scientific evidence [70], [31], [27] that may have been incorrectly generalized. In these studies radiographic/pathologic correlations showed that usually gliomas had clinically occult tentacles that extended (along nerve tracts) from the GTV for distances of up to 2-3 cm. In addition, these studies showed that recurrences tend to first occur within a distance of 2 cm from the original GTV boundary. However, this does not imply that all regions within 2 cm of the original GTV boundary contain clinically-occult glioma cells or that these cells could not be more than 2 cm away. Furthermore this approach does not take account of the highly complicated, three-dimensional structure of the brain. If clinically occult glioma cells existed with the same probability in all directions from the GTV margin, then the tumors would grow spherically, rather than the typical ”cloud-like” shape. This ”cloud-like” appearance shows the existence of some forces to facilitate glioma cell motion in certain directions (along nerve fibers), and prevent them in other directions (skull, tentorium, falx, perpendicular nerve bundles, etc.). These evidences suggest that the 2cm Euclidean margin may not be a correct way of defining PTV.

If we could identify PTV volume with more confidence, we could apply more effective therapy by radiating the truly occult parts and protecting the critical noncancerous tissues of the brain from unnecessary radiation. Unfortunately, there is no robust method to identify all regions of clinically-

occult glioma cells. Even with the application of advanced imaging technologies such as magnetic resonance spectroscopy (MRS) or positron emission tomography (PET), frequent false positive and false negative results are produced. Therefore, radiation oncologists still continue to treat all areas within the 2 cm margin equally. In this project we plan to identify the true PTV by mathematical modeling the growth process using the knowledge of biological behaviour of tumor growth and new imaging techniques.

2.3 MRI Modalities

Magnetic Resonance Imaging (MRI) is a useful imaging technology to visualize and distinguish different soft tissues. MRI images are classified into two main categories based on the dominant signal (whether it is the T1 time or the T2 time) measured to produce the contrast observed in the image. In T2-weighted images, free water and water embedded in the tissue is enhanced and appears bright while in T1-weighted images, fat tissue is enhanced and bright and water remains dark. Although these two modalities are very useful in discriminating between brain tissues, they might not differentiate between brain tissue and abnormalities accurately. In order to increase the contrast of abnormalities, a contrast agent, usually Gadolinium, is injected to the patient and some post-injection T1-weighted images are acquired. The areas that absorb the contrast agent are enhanced and visualized brightly in the image. These are the regions of the brain that contain 'leaky' blood cells (where blood moves through the brain-blood barrier). Therefore, tumors and other lesions are enhanced in these images [60]. Another imaging modality is Fluid Attenuated Inversion Recovery (FLAIR), which differs from T2-weighted images in the sense that it does not enhance cerebrospinal fluid (CSF), which will result in dark ventricles. So, lesions adjacent to CSF are visualized more clearly.

Appearance of the glioma tumors in MR images depend on the type of the tumor and the modality of image. The most important property of a glioblastoma visualized on MR images is a heterogeneous mass with central regions of necrosis surrounded by extensive water of edema [60] . A necrotic area, located within the tumor is displayed as a dark region in T1 and bright region in T2 and FLAIR magnetic resonance images. Necrosis is usually surrounded by a thick and wavy ring that is visualized in T1 post-injection images [62]. The necrotic region is dark and not contrast-enhancing. The enhancing ring around the necrotic region has the highest concentration of leaky blood cells which is the reason it enhances [62]. Edema contains fluid, which appears bright in T2 and FLAIR images and a dark region in T1 images. Since T2 images enhance water (no matter if it is free water or not), edema and ventricles appear with the same brightness. However, the ventricles appear dark in FLAIR images since they contain free water in contrast to edema that stays dark. In figure 2.2, all these modalities and the appearance of different structures of tumor on each modality is visualized. In general, edema and border definition are best observed on FLAIR and T2-weighted images. Mass effect can be seen on all modalities as the deformed tissues adjacent to tumor. These areas are

deformed due to the pressure of the expanding tumor and surrounding edema which pushes them against the skull. An example of mass effect can be seen in figure 2.3

2.4 Diffusion Magnetic Resonance Imaging

Diffusion MRI is a unique non-invasive technique for probing the random diffusion-driven displacement of water molecules in the body. The displacement statistics of water molecules provides information about the direction of their diffusion. By mathematically modeling the diffusion process, it becomes possible to recover the structure and geometric organization of tissues. One application of diffusion MRI is to identify the directionality of white matter tracts in brain tissue. Figure 2.4 shows an example of showing white matter tracts on MRI images. In the concept of glioma growth, this information helps to predict the preferential paths of tumor cell invasion and thus indicates growth direction.

2.4.1 Physical Principles of Diffusion Weighted Imaging (DWI)

In Nuclear Magnetic Resonance Imaging (NMR), the measured signal is obtained through a spin-echo process. Here, we briefly explain the spin-echo process. The MRI scanner maintains a constant and approximately homogeneous magnetic field $\mathbf{H}_0$. The spins align in the direction of $\mathbf{H}_0$. A 90 degrees radio-frequency pulse at time zero tips the spins into the transverse plane perpendicular to $\mathbf{H}_0$. Right after the pulse, spins precess about $\mathbf{H}_0$ with Larmor frequency that depends on the type of nuclei and is proportional to $\mathbf{H}_0$.

$$f = \gamma \mathbf{H}_0 \tag{2.1}$$

where γ is called the gyromagnetic ratio of the spins. Hydrogen, which is usually the spin object in biomedical imaging, has a gyromagnetic ratio of 42.58 MHz/T. The precessing of spins produce a net magnetization $\mathbf{M}$ of Larmor frequency, which in turn induces a current in the coil of the MRI scanner. The magnitude of the induced current is directly proportional to the net magnetization $\mathbf{M}$. The detected magnetic energy is based on the number of protons, which corresponds to the amount of water in the tissue. The T1 signals measure the longitudinal components of $\mathbf{M}$ after the relaxation time "T1", and T2 signals measure the transversal components of $\mathbf{M}$ after time "T2". In addition to the constant magnetic field $\mathbf{H}_0$, there are three magnetic field gradients to provide spatial information. Hence, MR imaging visualizes different tissues by detecting the amount of water molecules in each voxel location.

Water molecules move freely and collide with each other in an isotropic medium according to a Brownian motion. This motion can be detected by using additional magnetic field gradients in MR image capturing sequence. These new gradients allow capturing signals of nuclei displacement that can be used to form diffusion weighted images. To measure diffusion of water molecules in a given direction $\mathbf{g}_i : i = 1, ..., N$, the Stejskal-Tanner [63] imaging sequence is used (See figure 2.5). In

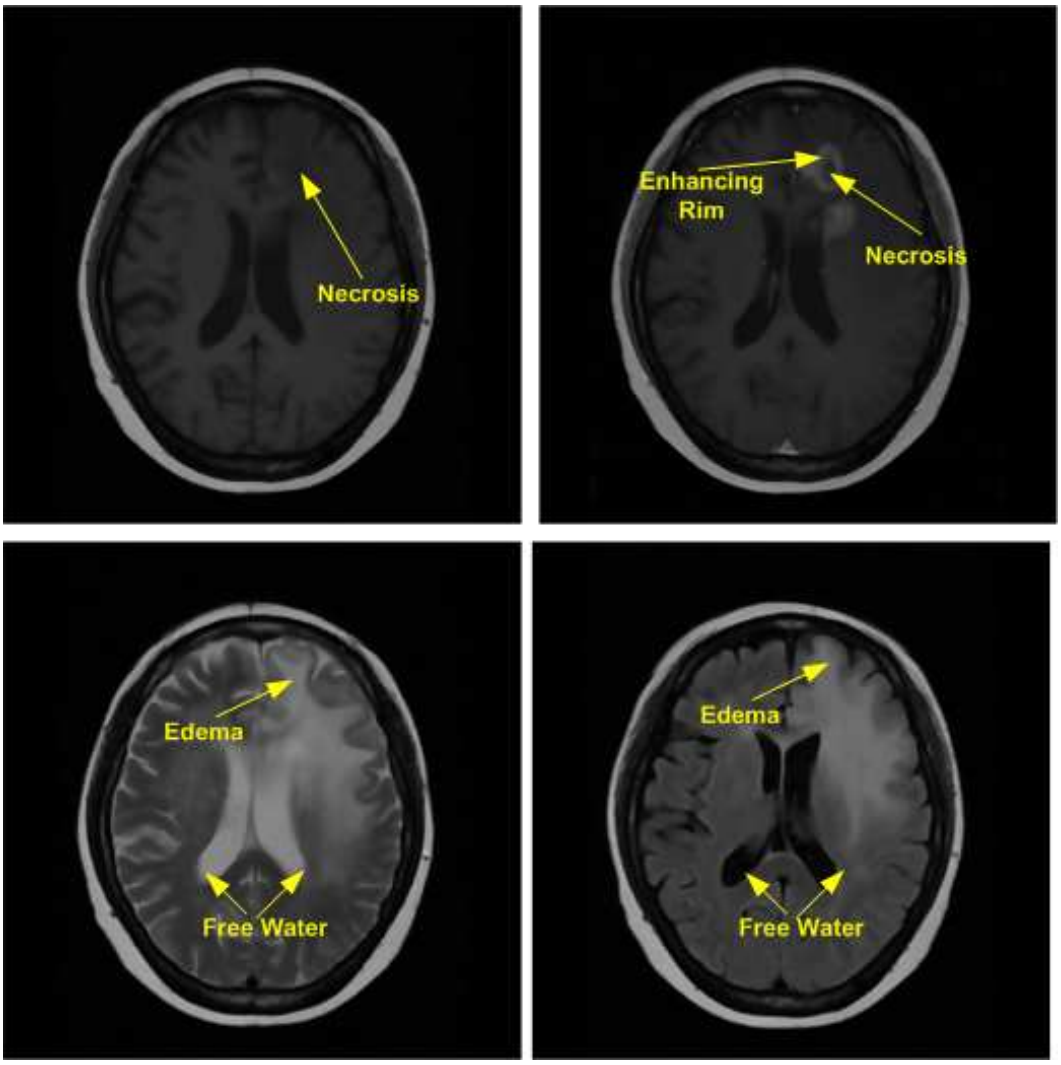

Figure 2.2: MRI scans of a glioblastoma tumor. (Top-Left) T1-weighted (Top-Right) T1-weighted after post gadolinium injection (Bottom-Left) T2-weighted (Bottom-Right) FLAIR image. Edema appears dark in T1 and T1-C (Contrast Enhanced) but bright in FLAIR and T2. Ventricles appear dark in T1, T1-weighted and FLAIR but bright in T2. Necrosis appears dark in T1 and T1-C, and brighter than edema in FLAIR and T2. The enhanced area is bright in T1-C.

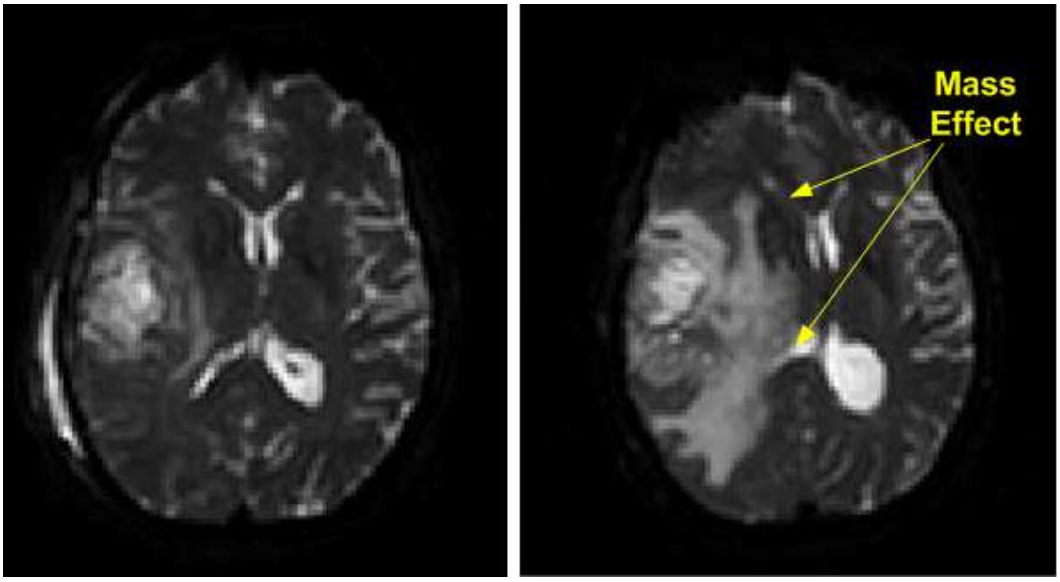

Figure 2.3: Tumor mass effect: An expanding tumor creates pressure that deforms parts of the brain around the tumor. This mechanical phenomenon is called the mass effect.

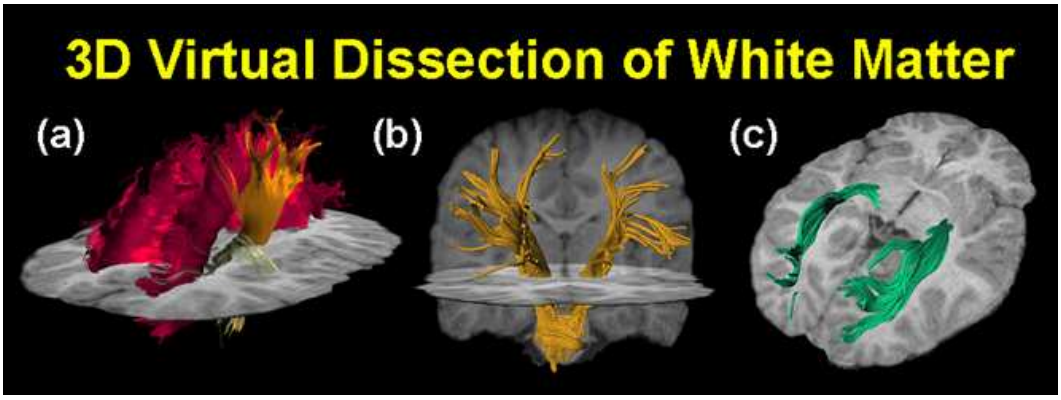

Figure 2.4: Tractography of white matter pathways. Diffusion tensor tractography identifies (a) the corpus callosum and internal capsule, (b) corticospinal tracts, and (c) optic radiations in a healthy control subject. (Image from Christian Beaulieu)

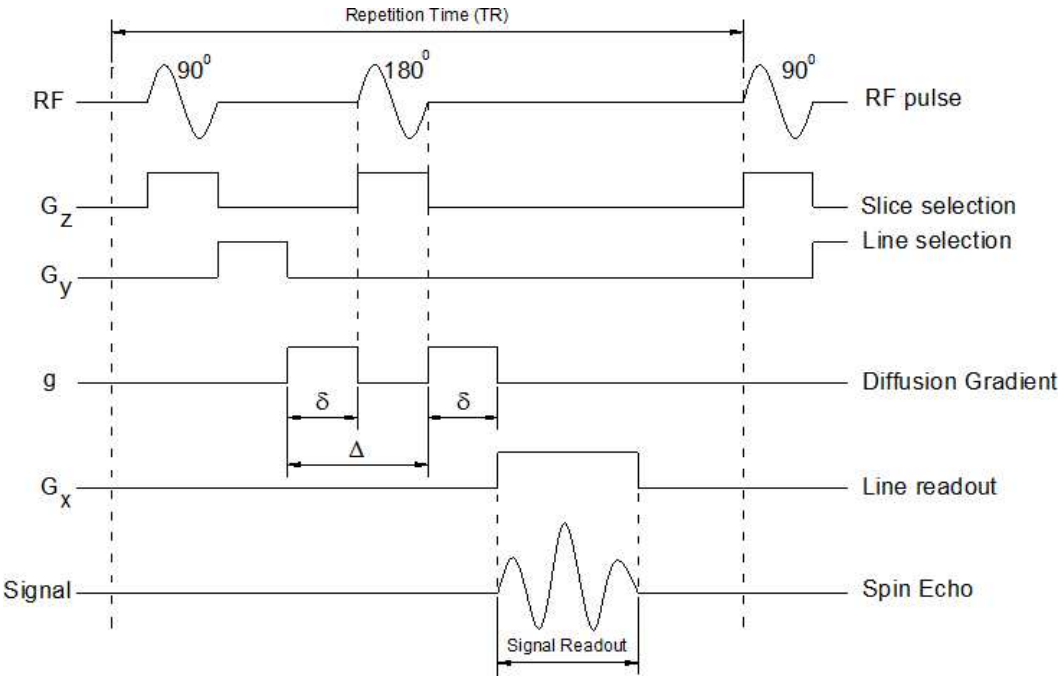

Figure 2.5: Stejskal-Tanner imaging sequence. (Image from [43])

this sequence, initially a 90 degrees RF signal is applied to flip the magnetization in the transverse plane. Then two rectangular gradient pulses $\mathbf{g}(t)$ are applied in the direction $\mathbf{g}$, of duration time δ, to control the diffusion weighting. They are placed before and after a 180 degrees negating pulse. The first gradient pulse causes a phase shift ϕ_1 of the spins whose position is now a function of time r(t):

$$\phi_1(t) = \gamma \int_0^{\delta} \mathbf{g}(t)^T \mathbf{r}(t) dt \tag{2.2}$$

Spin position is in fact assumed to stay constant during time. The negation effect of the 180 degrees pulse can be combined with the second gradient pulse to induce another phase shift of the form

$$\phi_2(t) = -\gamma \int_{\Delta}^{\delta+\Delta} \mathbf{g}(t)^T \mathbf{r}(t) dt \tag{2.3}$$

where Δ is the time between the two gradient pulses. This pulse cancels the phase shift ϕ_1 only for static spins. On the other hand, spins which move under Brownian motion during the time period Δ between the two pulses get different phase shifts by the two gradient pulses. This results in a $T2$ signal attenuation [11]. Figure 2.5 shows examples of diffusion weighted images acquired with two different directions $\mathbf{g}(t)$. By assuming the pulses to be infinitively narrow (see [69] for instance), the net phase shift from equations 2.2 and 2.3 is obtained as

$$\phi = \phi_1(t) + \phi_2(t) = \gamma\delta\mathbf{g}(t)^T(\mathbf{r}(0) - \mathbf{r}(\Delta)) = \gamma\delta\mathbf{g}(t)^T\mathbf{R} \tag{2.4}$$

where R denotes the spin displacement between the two pulses. To make the definitions simpler we introduce the displacement reciprocal vector $q = \gamma\delta\mathbf{g}$ [69]. The signal attenuation is modeled by

the following equation [28]

$$S(\mathrm{q}) = S_0(\exp(i\phi)) \tag{2.5}$$

where S_0 is the reference signal without diffusion gradient. S is the obtained MRI signal which corresponds to the net magnetization of all contributing spins. The MRI signal, which shows the diffusion displacement of spins in the direction g, is called the diffusion weighted signal. The image obtained from these signals is called diffusion weighted image, and Diffusion Weighted Imaging (DWI) is the technique of getting a set of diffusion weighted images from different directions.

2.4.2 Diffusion Tensor Imaging (DTI)

The Brownian motion of water molecules at a macroscopical scale yields a diffusion process. In an isotropic medium, the diffusion coefficient D was related is to the root mean square of the diffusion distance by Einstein [19]

$$D = \frac{1}{6\tau} \left\langle \mathbf{R}\mathbf{R}^T \right\rangle \tag{2.6}$$

where τ is the diffusion time and $\mathbf{R} = \mathbf{r} - \mathbf{r}_0$ is the net displacement vector, where $\mathbf{r}_0$ is the original position of a particle and $\mathbf{r}$, its position after the time τ and $\langle . \rangle$ denotes an ensemble average. The scalar constant D, known as the diffusion coefficient, measures the molecules mobility. In the isotropic case it only depends on the type of molecule and the properties of the surrounding medium but not on any particular direction.

However, this isotropic model cannot be applied to biological tissues where the medium is often anisotropic. For example in brain tissue, obstacles such as falx, tentorium, perpendicular nerve bundles etc., constrains water molecule motion in certain directions and some other forces facilitate motility of water molecules in certain directions (parallel nerve tracts). In this case, the scalar diffusion coefficient D must be replaced by a bilinear operator $\mathbf{D}$.

Equation 2.6 can by generalized be considering the covariance matrix of the net displacement vector $\mathbf{R}$:

$$\mathbf{D} = \begin{pmatrix} \mathbf{D}_{xx} & \mathbf{D}_{xy} & \mathbf{D}_{xz} \\ \mathbf{D}_{yx} & \mathbf{D}_{yy} & \mathbf{D}_{yz} \\ \mathbf{D}_{zx} & \mathbf{D}_{zy} & \mathbf{D}_{zz} \end{pmatrix} \tag{2.7}$$

This is a second order symmetric and positive-definite tensor. The probability density of water molecules free diffusion can be modeled by a Gaussian function.

$$p(\mathbf{r}|\mathbf{r}_0, \tau) = \frac{1}{\sqrt{(4\pi\tau)^3|\mathbf{D}|}} \exp\left(-\frac{(\mathbf{r}-\mathbf{r}_0)^T\mathbf{D}(\mathbf{r}-\mathbf{r}_0)}{4\tau}\right) \tag{2.8}$$

where p is the probability to find a molecule, initially at position $\mathbf{r}_0$, at $\mathbf{r}$ after a delay τ.

In diffusion tensor imaging (DTI), we are interested in calculating the diffusion tensors $\mathbf{D}$ for each voxle. Each tensor $\mathbf{D}$ consists of six separate unknown parameters. Diffusion weighted imaging (DWI) can be applied to find the unknown parameters of $\mathbf{D}$. For this mean, we can rewrite the obtained diffusion signal S from equation 2.5 considering the diffusion probability density function p:

$$S(\mathbf{q},\tau) = S_0 \int_{\mathbf{R}^3} p(\mathbf{r}|\mathbf{r}_0,\tau)\exp(i\mathbf{q}^T\mathbf{R})dr \tag{2.9}$$

Using Gaussian probability density of the form of equation 2.8 yields a simple expression for the signal $S(\mathbf{q},\ \tau)$ [63]:

$$S(\mathbf{q}_i,\tau) = S_0 \exp(-b\mathbf{g}_i^T\mathbf{D}\mathbf{g}_i) \tag{2.10}$$

where $S(\mathbf{q}_i,\tau)$ is the signal in the direction $\mathbf{g}_i$ and b is the diffusion weighting factor depending on scanner parameters (proposed by Le Bihan et al. [7]) as:

$$b = \gamma^2\delta^2|\mathbf{g}|^2\left(\Delta - \frac{\delta}{3}\right) \tag{2.11}$$

We recall that $|\mathbf{g}|$ is the magnitude of the diffusion gradient pulse, δ its duration and Δ the time separating two pulses (see figure 2.5). A typical value of b is $1000s.mm^{-2}$. The diffusion tensor **D** can then be estimated at each voxel using the $S(\mathbf{q}_i,\tau)$ and S_0. We need at least six independent measurements in gradient directions g_i and one reference image S_0. But more images can be taken to increase the accuracy and also images can be collected with one or more b factor(s). The classical method to derive the tensors uses a least squares technique, but various alternative methods have been proposed. We have finally obtained a diffusion tensor image, i.e. a 3D image with 6 parameters describing the local tensor **D** at each voxel.

Diffusion-tensor MRI is the most popular technique for diffusion MRI reconstruction. It is simple and provides diffusion anisotropy statistics that can be used to construct fibre tracts. However, a major drawback of DT-MRI is that the Gaussian model is a poor fit to the data and DT-MRI can only estimate one fiber orientation in each voxel. Therefore, when fibre crossing happens within a voxel, the model cannot estimate both fibre orientations and the single fibre orientation estimate lies consistently between the two true fibre directions [2]. Despite this shortcoming of DT-MRI, it has not still been replaced by any other method that is as simple and fast in implementation. Modern scanners come with a built-in acquisition sequence for DT-MRI and manysoftwares are available for the necessary post processing. For these reasons, we also use DT-MRI for diffusion MRI reconstruction in this project.

2.4.3 Diffusion Tensor Properties and Indices

A diffusion tensor **D** can be decomposed to its eigenvalues (λ_1, λ_2, λ_3) and eigenvectors ($\mathbf{e}_1$, $\mathbf{e}_2$, $\mathbf{e}_3$), where eigenvectors show diffusion directions and eigenvalues show the amount of diffusion in each direction. One can form an ellipsoid from the diffusion tensor, which corresponds to an iso-surface of the probability density function. Figure 2.6 shows a DTI image along with the tensors. Additionally a sample ellipsoid with its eigenvalues and eigenvectors is visualized. Different scalar indices have been proposed to characterize diffusion anisotropy. Initially, indices were simply calculated from diffusion-weighted images [5]. These indices were not really quantitative since they did not correspond to a single meaningful physical parameter and were dependent on the choice of

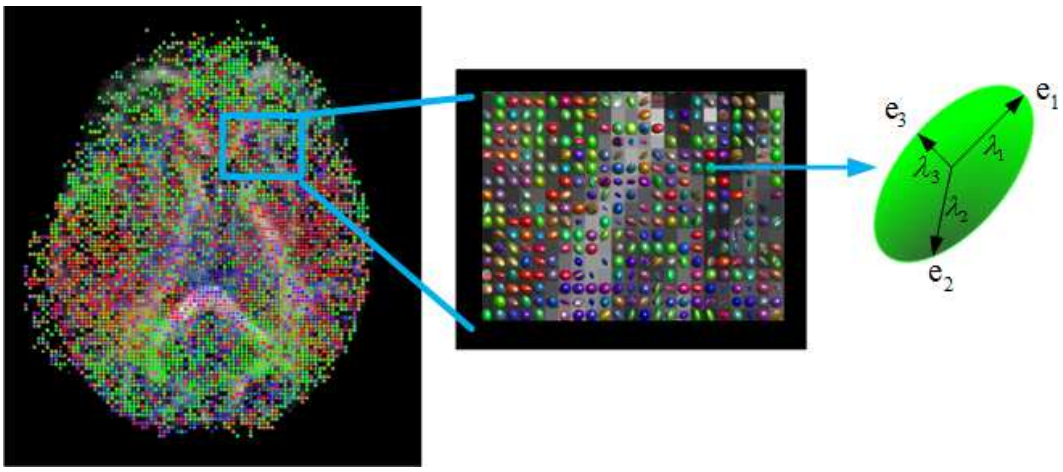

Figure 2.6: Diffusion tensors: An example of a DTI image, where tensors are represented by ellipsoids. Each ellipsoid is characterized by the 3 eigenvectors that characterize diffusion along $\mathbf{e}_1$ and across ($\mathbf{e}_2$,$\mathbf{e}_3$). The eigenvalues λ_1, λ_2, λ_3 are the diffusion rates in the corresponding directions.

directions made for the measurements [22]. Hence, invariant indices were introduced to avoid such dependence and provide an intrinsic structural information [5]. Two standard invariant indices derived from DTI are the average apparent diffusion coefficient, known as the mean diffusivity (MD) and the fractional anisotropy (FA) [4]. MD is a rotationally-invariant average measure of the diffusion rate that is fairly homogeneous throughout the brain, with the exception of neonates, when diffusion-weighted images are acquired at lower diffusion sensitivity factors (with b-values up to about 1000 s/mm2).

$$MD = \frac{\lambda_1 + \lambda_2 + \lambda_3}{3} \tag{2.12}$$

Fractional Anisotropy (FA) is a measure of the directionality of the diffusion. FA value varies between 0 (corresponding isotropic diffusion) to 1 (highly anisotropic diffusion).

$$FA = \sqrt{\frac{3}{2}} \frac{\sqrt{(\lambda_1 - \lambda)^2 + (\lambda_2 - \lambda)^2 + (\lambda_3 - \lambda)^2}}{\sqrt{\lambda_1^2 + \lambda_2^2 + \lambda_3^2}} \tag{2.13}$$

MD shows the average of eigenvalues while FA measures their covariance. FA has far greater variability in the brain than MD and in particular highlights the white matter tracts (figure2.7,b). The directionality of the white matter tracts is usually presented on color-coded FA maps, where red indicates left/right tracts, blue indicates superior/inferior tracts, and green indicates anterior/posterior tracts (figure2.7,c). High FA values could correspond to areas of high fibre bundle density and/or increased myelination. Low FA values could imply axonal degradation or demyelination as well as tumor cell infiltration or edema.

2.5 Conclusion

In this chapter, we first studied different classes of brain tumors. This classification shows that Glioblastoma is the most malignant primary tumor. Since this tumor rarely metastasizes, it is possi-

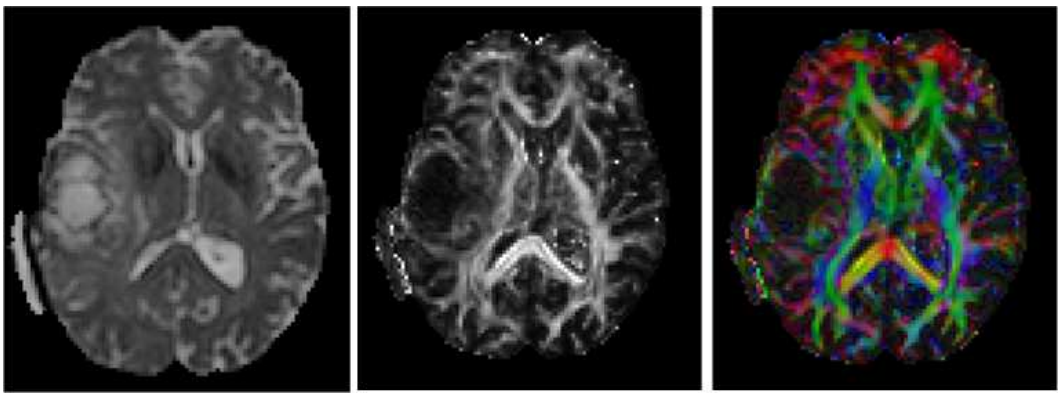

Figure 2.7: Left: Mean Diffusivity (MA), average measure of the diffusion rate; Middle: Fractional Anisotropy (FA), A quantitative measure of the micro-structural integrity and coherence of white matter tracts. Fractional anisotropy ranges from 0 (black, isotropic, direction-independent diffusion) to 1 (white, anisotropic, direction-dependent diffusion). Right: The direction of diffusion color coded on FA map, each color shows a direction; Red: left-right, Green: Anterior-Posterior, Blue: Superior-inferior

ble that improvement in local control of this tumor can directly result in the quality of its treatment. To control this tumor, we need to enhance radiography treatment, which in turn requires a more precise definition of the planning target volume (PTV). Diffusive behaviour of tumor cells in the direction of water molecules plus advanced imaging technologies that can detect the diffusion of water molecules (DWI) can provide us necessary tool to define PTV volume more correctly. In this chapter, we also explained DWI and DTI imaging techniques and the properties of extracted tensors.

Chapter 3

Review of Mathematical Modeling of Brain Tumors

3.1 Introduction

Cancer research has been a fertile field of study during the past several years. Various approaches have been applied to mathematically model different aspects of cancer dynamics. As we mentioned in Chapter 2, the main aim of this project is to define a more realistic radiotherapy margin adapted to the brain tumor invasion. Only few projects in the literature have directly addressed the task of finding the tumor invasion margin, while an extensive portion of existing research belongs to generative mathematical modeling of tumor growth. However, we need to consider that modeling the tumor growth and finding its invasion margin are interrelated tasks since the occult cells are the reason for the tumor growth and recurrence over time. Therefore, we can use the same mathematical modeling for both concepts. In this chapter, we present a literature review for the general problem of tumor growth mathematical models. This helps to situate the methods presented in this work better among other works.

The vast number of papers published in mathematical modeling of cancer growth in the past twenty years has motivated researchers to survey and classify these studies. We refer the reader for some good reviews on this topic to [29], [20], [3] and [61]. Here we discuss some main research orientations and classifications.

The main goal of tumor growth modeling and simulation is to develop a mathematical abstraction that can explain dynamics of tumour formation and behaviour of tumor cells in time. Such an abstraction can be in the format of differential equations, stochastic models or individual-based simulations. Forming such a mathematical model can have several benefits depending on the purpose of the research. First, it helps to unify outcomes of different experimental researches in a single mathematical model. A virtual simulation of this mathematical model allows researchers to understand the underlying mechanism of tumor growth. This in turn provides the opportunity to interpret real experimental results and also to observe effects of different treatments on cancerous cells. So

it can ultimately improve the overall clinical outcome by predicting the results of specific forms of treatment applied in different times and also predicting the probability of recurrence of the tumor in the future. Another important usage of mathematical modeling is in therapy planning where it helps radiologists to define the PTV corresponding to tumor invasion margin. It also helps to predict the future shape and invasion of an existing tumor and the oncologist can decide the best time of surgery and treatment. Some of the existing models are patient specific which means that they describe the growth based on the observations obtained from the patient. These models can help the oncologist to pick the type of drugs that would best suit the patient.

Certain biological aspects are considered when modeling the tumor growth. These aspects include internal dynamics of cancerous cells with each other and with healthy surrounding tissue, nutrition and oxygen transport from the extracellular matrix and from the vascular network, chemicals produced by tumor cells, and finally the type of the underlying tissue. Based on these fundamental aspects, scientist have conducted their research on different stages of tumor growth including initial genetic alterations and their effects, early avascular tumor growth, proliferation, invasion, angiogenesis, vascular growth and metastasis. Hatzikirou et al. [29] introduced a new classification for tumor growth models based on these stages in growth process, which we will explain in more detail in Section 3.2.

As we mentioned, the main purpose of mathematical modeling is to introduce a mathematical abstract that can best explain the clinical and experimental observations. These observations come from different sources, including *in-vitro* experiments done in lab, *in-vivo* experiments tested on animal subjects, autopsy result, medical images of patients such as Computer Tomography (CT), Magnetic Resonance Imaging (MRI) and finally the new imaging technique, Diffusion Weighted MRI (DWI). These observations can be classified based on their scale into two groups, microscopic and macroscopic. Observations on cellular activities such as those coming from *in-vivo* and *in-vitro* experiments belong to microscopic scale while those coming from different imaging sources are placed in the macroscopic class. Another popular classification of growth models is based on these scales of observations [20].

In the rest of this chapter, we will discuss about different classifications for tumor growth models and explain the most important works of each class in more details.

3.2 Classification of Mathematical Growth Models

During the last twenty years, theoreticians have developed a great variety of mathematical models covering various morphological and functional aspects of tumour growth. These models can be classified in different ways. The first model of classification we explain here was introduced by Hatzikirou et al, [29]. They defined a new classification for researches on Glioblastoma multiforme (GBM) modelling, in a way that was useful for both theoreticians and practitioners. Their categorization takes into account the main medical and biological focus of each study, rather than

the mathematical approach chosen. There are four different classes in their model: *Early tumour growth, Tumour invasion, Genetic mutations and their macroscopic effects* and *Therapy.*

3.2.1 Hatzikirou Classification

Mathematical modelling allows answering diverse biological questions concerning the analysis of early GBM growth, therapy effectiveness or even simulations in realistic brain structure and geometry. Here we classify the models considering biological aspects of GBM growth.

Early tumour growth

This class contains those studies that model the early growth of gliomas. These methods mostly capture the glioma growth evolution from the very beginning (first cell or a small set of cells) of the disease. This kind of cell-based modelling helps to identify the self-organizational behaviour of the tumor system motivated by micro-dynamics (cellular or even molecular interactions). Although these models usually deliver convincing qualitative simulations, they are still far from achieving exact quantitative results (e.g. Kansal et al.[38]).

Invasion

This class includes research that addresses the invasive behaviour of tumor growth as the dominant aspect of the growth. A theoretical framework of invasion was introduced first by Tracqui et al. [17], [68], [73], [9]. These early GBM models deal with invasion as a homogeneous isotropic process while Swanson et al. [64] and Wurzel et al. [74] added the inhomogeneity of the brain topology to the model. The brain topology accelerates the invasion in white matter fiber tracts. These approaches provide an appropriate understanding for better therapy designs.

Tumor Modelling of Genetic Alterations and their Macroscopic Effects

An important theoretical and clinical challenge is the development of models that predict which microscopic (genetic) modifications are required for a given macroscopic behaviour. One interesting approach is to use an event-guided evolution due to alterations of the genetic profile of the cells where the term “event” refers to a sequence of cell mutations. These models are complicated multiscale models reflecting microscopic changes with macroscopic consequences. There is almost no successful research in this category. Painter et al. [37] has introduced the only known method in this category. He has developed a macroscopic model that describes several tumor-relevant quantities: malignant cell densities (of all grades), vascular density, necrotic tissue and chemical (nutrient and toxic) concentrations. The goal is to analyse the effect of genetic mutation in time at the macroscopic level (in terms of tumor cell concentration).

Therapy

This last class belongs to the mathematical modelling of glioma therapy instead of glioma growth. So far, numerous methods have been introduced to model glioma chemotherapy, tumor resection and glioma radiotherapy. In early modelling the effects of chemotherapy, glioma growth and invasion was considered a homogeneous process while Swanson et al [66] applied the assumption of a diffusive tumor in an inhomogeneous brain structure to make the therapy more effective. This was an important contribution which opened a new direction for the tumor growth modeling research.

3.2.2 Scale Based Classification

Although the classification introduced by Hatzikirou [29] is suitable from medical and biological point of view, another more organized classification is based on scale. In this new classification, each method is simply categorized under *Microscopic* or *Macroscopic* groups. The main difference of these two models is the scale of observations they explain and formulate ([20], [59]).

Micorscopic models describe the growth process in cellular level, concentrating on activities that happen inside the tumor cell. They concentrate on observations coming from *in-vitro* and *in-vivo* experiments and describe the interactions between tumor cells and their surrounding tissue, the complicated chemical networks inside tumour cells and nutrition and oxygen availability. Macroscopic methods, on the other hand, formulate tumor growth in a clinically observable scale, as is seen in medical images. These approaches focus on tissue level processes considering large scale quantities such as tumor volume and flow. Microscopic models are roughly classified based on the three phases of the growth including avascular, angiogenesis and vascular growth. In the next section we will briefly explain these three subclasses but as our project is defined at the macroscopic level, we will skip details.

Macroscopic tumor growth models are based on large scale observations such as medical images which are at millimetre resolution. Macroscopic models are classified based on the effect of the tumor growth on the brain [20]. The two main subclasses are *mechanical* models which concentrate on the mass-effect of the tumor and *diffusive* models which concentrate on the infiltration of the brain tissue. This general classification is suggested by Konukoglu [20]. Here, we add the sub-classification of the *diffusive* class in order of complexity:(i) isotropic diffusion models (Murray [1989]), (ii) non-isotropic diffusion models (Swanson et al. [64]), and (iii) direction dependent diffusion models (Clatz et al. [13], Jbabdi et al. [36], Konukoglu et al. [40]). We extend this with: (iv) DTI-based geometric models (Cobzas [14]).

In the rest of this chapter, we will go through some of the most important models in each category and also clarify our own classification.

3.3 Microscopic Models

Models under this class describe the tumor growth process in a sub-cellular level using *in-vivo* and *in-vitro* experiments. They capture the interactions of tumor cells with each other and with the surrounding tissue. Mechanical phenomenon like cohesion forces, adhesion forces and pressure are also included to explain the physical behaviour. Various mathematical methods have been applied to model all these phenomena including Partial Differential Equations (PDE), stochastic models and cellular automata. We sub-classify these models based on the stage of the tumor growth: the **avascular** growth, the **angiongenesis** and the **vascular** growth. Here we briefly explain each of these stages and the corresponding researches on them.

3.3.1 Avascular Growth/ Solid Tumor

The avascular growth corresponds to the stage of proliferation of tumor cells. It was originally thought that the tumor is a solid mass that only grows by means of mitosis. Mayneord in 1932 [48] published one of the first papers based on this hypothesis. The models using this idea apply only population growth dynamics such as exponential, Gompertz or logistic proliferation models. Although not completely known, it is assumed that there is no invasion to the healthy tissue in the avascular stage and the interactions between tumor cells and the healthy tissue is also limited [3]. Although a simple proliferative behaviour means that the tumor should grow indefinitely, it does not happen in reality due to a simple reason. As the tumor grows, less nutrition and oxygen will be available for cells in the center of the mass. Tumor cells that are not getting enough nutrition die and the necrosis is formed. Only those cells on the periphery remain the viable ones that will continue to proliferate [10]. McElwain [49] added another cells loss mechanism called apoptosis in formation of the necrosis. He showed that tumor cells may die even if they receive enough nutrition and oxygen. When the necrosis and proliferation balance each other, the avascular tumor reaches a limiting size which is assumed to be 1-3 mm in diameter [56]. In addition to these deterministic models, there have been some stochastic ones emphasizing the probabilistic nature of the growth. We refer the reader for more information about these models to [20].

3.3.2 Tumor-Induced Angiogenesis

Angiogenesis (vascularisation) is the stage where tumor cells in the avascular mass change the existing vascular network to make new vessels to feed them. In this stage, due to the availability of nutrition sources, the tumor can overcome its limit size, speed up the growth and invade to the surrounding tissue. Tumor-induced angiogenesis is a complicated process including different chemical, physical and mechanical phenomena. The whole process is still not totally understood. But due to its crucial role the tumor growth, its underlying biological mechanism have been studied and analyzed in many papers. Mantzaris et al. [47] review some of the known biological processes happening in angiogenesis. Also, different mathematical formulations are used to model this complex phenomena

phase by phase [56], [23], [12]. As the main focus of this project is on macroscopic models, we omit details about this phase.

3.3.3 Vascular Growth/ Invasive Tumor

The third stage of the tumor growth is the vascular growth. In this stage several processes happen simultaneously that make the growth process more complicated. The main difference of avascular and vascular growth is in the existence of blood vessels. The blood vessels provide almost unlimited source of nutrition compared to avascular stage where nutrition was only available through diffusion from perimeter. Consequently vascular tumors are not compact masses of tumor cells and they can start to grow indefinitely. Moreover, in addition to cellular and chemical interactions going on in the first two stages, tumor cells start invading the surrounding tissue. While the difference between cancerous and healthy regions is clear in the avascular stage, this difference vanishes in the vascular stage since tumor cells diffuse towards healthy tissue. Most of recent works on microscopic growth either model the vascular process or combine all the three phases of growth.

3.4 Macroscopic Models

Macroscopic tumor growth models are based on large scale observations such as medical images. The images currently used in mathematical modeling include Computed Tomography scans (CT), MRI and diffusion tensor MRI. Currently used information of large scale observations is very limited, only including tumor delineation area and brain deformation. Limited observations reduce the number of factors included in the modeling, which results in a simpler formulation compared to the microscopic case. Moreover, in contrast to microscopic models that focus on theoretical aspects, macroscopic modeling research is driven by real clinical data, e.g. real boundaries of the brain, tumor region resection and brain tissue characteristics. Hence, evaluation of these models can be done using real patient data. For example a sequence of MRI images of the brain can be used to evaluate the growth model in time. The macroscopic models are classified based on the targeted effect of the tumor. The models that formulate the invasion of the tumor in the surrounding tissue form the diffusion class while the ones that concentrate on tumor mass-effect make the mechanical class. The models in the diffusion class can be sub-classified based on their degree of complexity. Also, the methods under this category are different in a way that most of them aim to find the tumor growth in time while few of them try to find the tumor invasion margin in the initial scan time. In the rest of this section, we review the methods under these two categories.

3.4.1 Diffusive Models

Almost all macroscopic models formulate the growth process based on two fundamental characteristic of tumor: diffusion and proliferation, which are formulated together as a general equation called diffusion-reaction formalism introduced by Murray [54] in 1989. This equation simply states that

the rate of changes in tumor cell density depends on infiltration of tumor cells in to surrounding tissue in addition to their reproduction. The diffusion-reaction equation is a partial differential equation (PDE) with formatted boundary conditions (real boundaries defined in brain), which is then solved using numerical techniques. The physical base and mathematical formulation of this equation is explained in detail in Chapter 4. Numerically solving this equation also requires information about physical boundaries inside the brain, as these barriers inhibit cell diffusion. Known barriers include the skull, the tentorium cerebelli and the falx cerebri. We introduce a new classification of macroscopic models based on the diffusive part of the diffusion-reaction equation. The key parameter in the diffusive part is the diffusion tensor **D** that defines the direction of motility of tumor cells. The degree of difficulty depends on the type of diffusion tensor used. By progress of imaging techniques, diffusion tensors gradually contained more information about the real diffusive behaviour of tumor cells. This fact is reflected in our classification.

(i)+(ii) Isotropic and non-isotropic diffusion models

The diffusion part of reaction-diffusion equilibrium defines the invasion of the tumour cells by means of a Brownian motion characterized by an isotropic (spherical) or anisotropic (elliptical) tensor. In the case of isotropic diffusion, cells will spread equally in all directions, while with anisotropic diffusion, cells will spread faster in the direction of the largest axis of the tensor (ellipsoid) and slower in the direction of the smallest axis. In early researches, a mathematical model of glioma growth and diffusion was developed based on the analysis of serial CT scans of a patient with recurrent anaplastic astrocytoma. They used an isotropic diffusion model that allowed tumor cells to diffuse equally in all directions with the same speed for all tissues [17], [68], [73]. The experimental results of Giese et al. [1] established that tumor cells move faster in white matter than in gray matter. Swanson et al. [64], [65] incorporated this experimental fact to the growth model by multiplying the tensors in white matter with a scaling factor. This isotropic model, which always results in spherical cell invasion, only simulates high-grade gliomas. Low-grade gliomas, which exhibit complex finger-like shapes, are not well described by an isotropic model.

(iii) DTI-based diffusion models

Extending Swanson's work, Clatz et al. [13], Jbabdi et al. [36] and recently Konukoglu et al. [40] included anisotropy to the invasion mechanism of tumor cells. By adding anisotropy to the numerical simulation of the tumor diffusion process, the"cloudy like" tumor shapes observed in MRI scans is better formed. These models assume that tumor cells move faster in white matter compared to gray matter and also follow the white matter fiber tracts in the brain. The tumor diffusion tensor (TDT) is constructed from the DTI water diffusion tensor data in different ways. The idea of all these construction methods is to assign an isotropic diffusion to the gray matter and an anisotropic diffusion to the white matter, with the greatest diffusion along the direction of fibres. The so far proposed transformation of water tensors in DTI data into TDT is rather heuristic and our observations show that more elaborate models need to be developed. All the mentioned diffusive models simulate

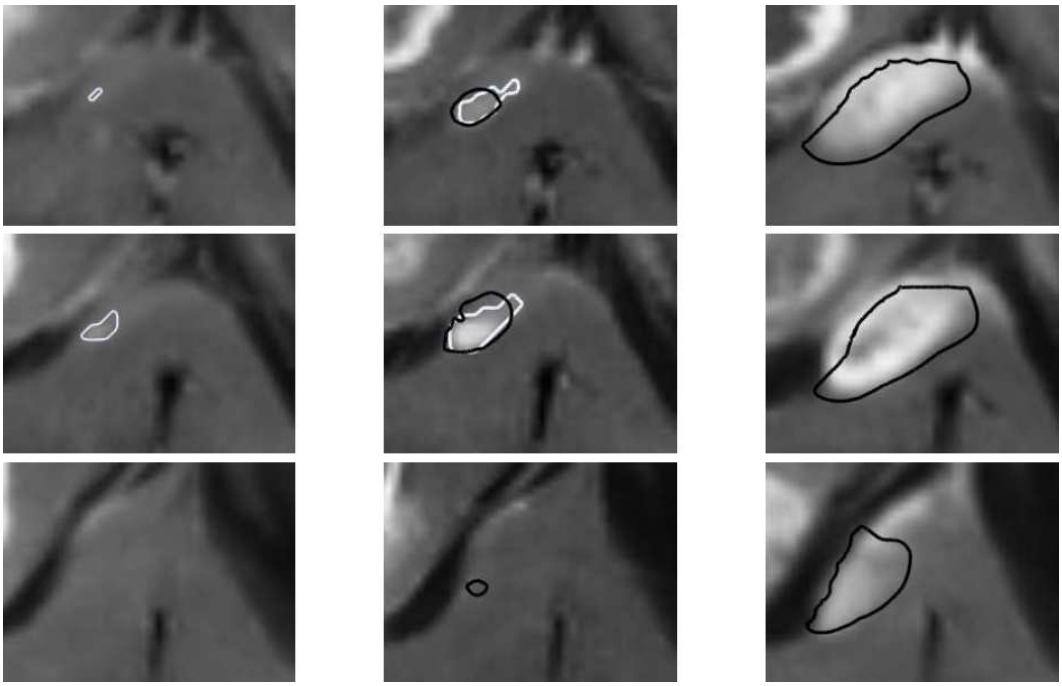

Figure 3.1: A diffusive model (by Konukoglu [40] with anisotropic diffusion and patient specific parameter estimation) is applied to the images of a real patient suffering from high grade glioma. Images in left column show different slices of the T1-post gadolinium images of the initial time with manual delineation of the tumor (in white) . The middle column belongs to slices of 21 days later with manual segmentation (white) and simulation result (black). Right column shows the final state of the tumor with the results. (Image from [40])

the tumor growth in time, not directly the tumor invasion margin. Konukoglu et al. [39] suggested capturing the tumor invasion margin by extrapolating the low tumor densities in MRI images. For extrapolation, they considered the travelling solution of the reaction-diffusion equation in an infinite cylinder. However, no proper validation is available in their paper.

A main limitation of published DTI-based models is the lack of validation with real patient DTI data. Some of the above-mentioned models use non-patient DTI data, either on atlas tensors registered with the patient (Clatz et al. model [13]) or tensors from a single healthy subject that are unregistered with the patient (Jbabdi [36]). Authors in [39] validate their model by simulating a synthetic tumor on a healthy brain and comparing the simulation result with the simulation result of another method. Validation method in other papers is more plausible, comparing the visible tumor growth in MR images with the one simulated by the model [40]. However, none of the models are validated on more than two cases. In this project, thanks to the availability of several DTI data of patients, the proposed methods are validated on real data.

iv) DTI-based geometric models (geodesic model)

In this thesis, we add a new class to the family of *macroscopic* growth models by introducing the idea of using geodesic distance on a Riemannian (curved) manifold of brain fibres to define the tumor invasion margin. This idea is basically one of the main contributions of this thesis, which has

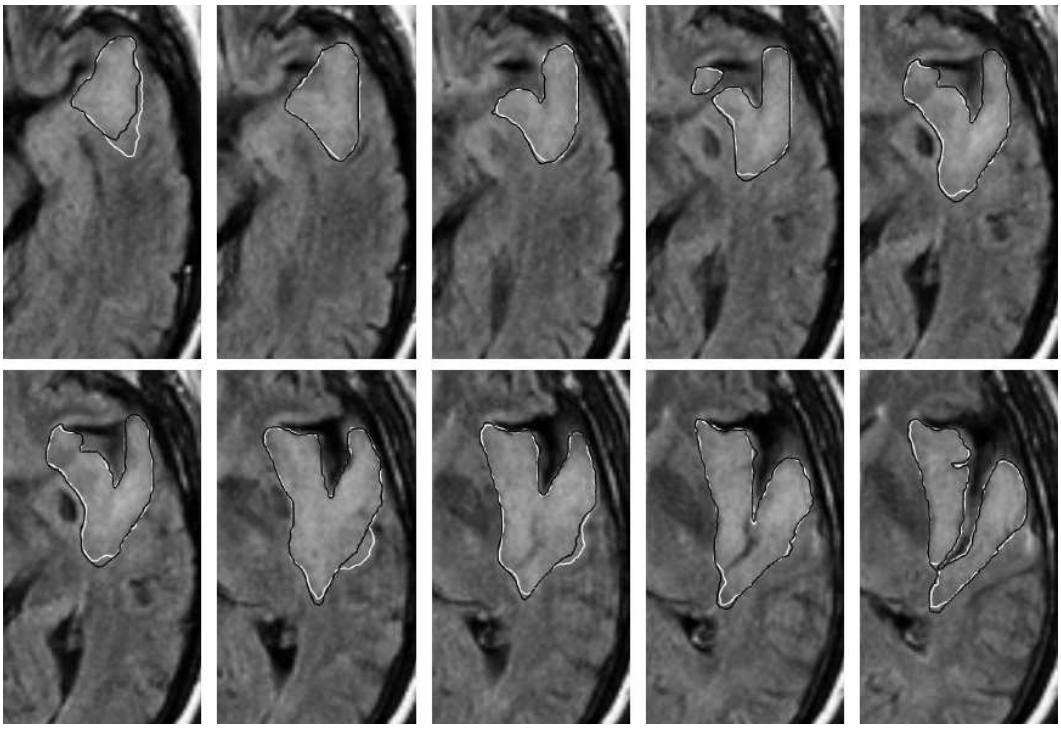

Figure 3.2: Konukoglu model [40] applied to a low grade tumor. Each column show several slices of T2 flair images corresponding to one time step of the growth with manual delineations (in white) and simulation result (in black). Note that the model works much better for low grade tumors where the rate of growth is low and parameters can be estimated more accurately. (Image from [40])

also been published in MICCAI 2009 [14]. As mentioned, the current radiation therapy practice is to use the MRI segmented tumor and measure a 2cm straight-line Euclidean distance outward from the contour. By using the DTI data, we can introduce of a new metric, the geodesic distance, onto the brain images. The formulation of white matter as a Riemannian manifold was first introduced by O Donnell et al. [55] and later formalized by Lenglet et al. [45]. They used this model for white matter connectivity mapping (tractography).

The geodesic distance can be directly integrated into planning of radiation targets and doses by predicting the distance occult cells have reached beyond the visible tumour margin. As we will explain in Chapter 5, this formulation is numerically more stable since it results in a first-order PDE as opposed to the second-order anisotropic diffusion PDE used in other work. In addition, the distance formulation is easily transferable into radiation treatment planning as it defines a consistent map of the brain, where every location is marked with the time it would take glioma growth to reach that point.

The closest model to ours is the recent model by Konukoglu et al. [40] on image guided personalization of reaction-diffusion equation, in a way that the tumor delineation area is captured on MRI images instead of the tumor cells density. To capture the tumor delineation area, the reaction-diffusion equation is approximated with an Eikonal equation where the travelling time moving frame solution of the equation is the tumor delineation in time. Such approximation is based on the asymptotic properties of the reaction-diffusion equation under certain conditions. But, we do not need to make any approximation for modelling the distance on a Riemannian manifold. Moreover [40] estimates the patient specific parameters of the model using images of the patient taken at successive time instances. Although the patient specific parameter estimation has several clinical benefits, it is not helpful for our problem of defining the tumor invasion margin. Since to define the invasion margin at the time of radiation treatment, we only have one time instant image of the patient at hand, not a time sequence of images. In figures 3.1 and 3.2, the result of applying Konukoglu et al. method [40] to one low-grade tumor and one high-grade one is shown. As visible in the figures, the model works much better on low grade glioma where the rate of the growth is much lower and several time point scans with little difference are available. This way, parameters for further scans can be more accurately estimated.

3.4.2 Mechanical Models

Mechanical models mainly focus on modeling the effect of tumor growth on deformation of the surrounding tissue known as mass effect. These models couple two distinct formulations, one for growth and one for the mechanical deformation of brain tissue. The combination can describe the mechanical interactions of the tumor and the brain tissue. To make a mechanical model, first the mechanical properties of brain tissue need to be characterized. Brain tissue is a deformable material but not elastic. Since characterization of brain tissue properties is very complicated, almost all mod-

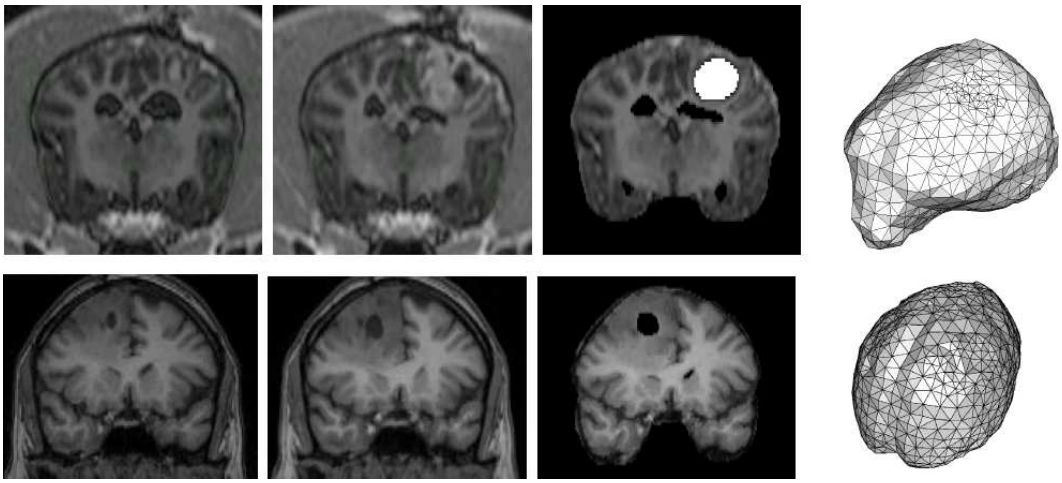

(a) (b) (c) (d)

Figure 3.3: A mechanical model to model the mass effect by Mohamed et al. [51]. The tumor growth is modeled as a solid proliferation process. Example cross sectional images from the starting (a) and target (b) 3D images for two different models (upper and lower row) compared to the deformed images obtained via the mechanical model (c). Tumors in simulated images are assigned similar intensities to the real images; (d) shows the outer surface of the FE meshes used. (Image from [51])

els make some assumptions to simplify the definition [71].

One the first mechanical models was proposed by Wasserman et al. [71]. He simply assumed that the brain tissue is a linear elastic material for which strain-stress relations by generalized Hook's law are applicable. The strain caused by the tumor under certain stress was proportional to the density of brain tissue. For the growth part he used a simple linear proliferation model. He modeled growth of tumor in CT images using this model. Kyriacou et al. [42] extended this model by characterizing brain tissue as a nonlinear incompressible elastic material instead of a simple linear one. They could capture large deformations by introducing the nonlinear elasticity to the model. Tumor growth was still modeled as a single proliferative process. They used their method to register 2D CT or MRI images of patients having tumors with brain atlases.

Mohamed et al. [51] modeled the tissue as an isotropic and homogenous hyperelastic material. So they could relax the incompressibility assumption made in [42] and still generate the large deformations (see figure 3.3). In their model, the mass effect was generated by the expansion of both the tumor and its surrounding edema. Again in this model, tumor growth only consisted of proliferation with constant mitosis rate. Hogea et al. [32] reformulated the same model in a general Eulerian framework with a level-set based approach for the evolving tumor. The new formulation had the advantage of using regular grid and was more efficient. They modeled the brain tissue as a linear inhomogeneous elastic material that can have different material properties in the white matter, gray matter and CSF. The non-linearity was handled in the same framework, via a series of linearized problems.

In all these methods, the tumor growth model was kept very simple as a linear proliferative process.

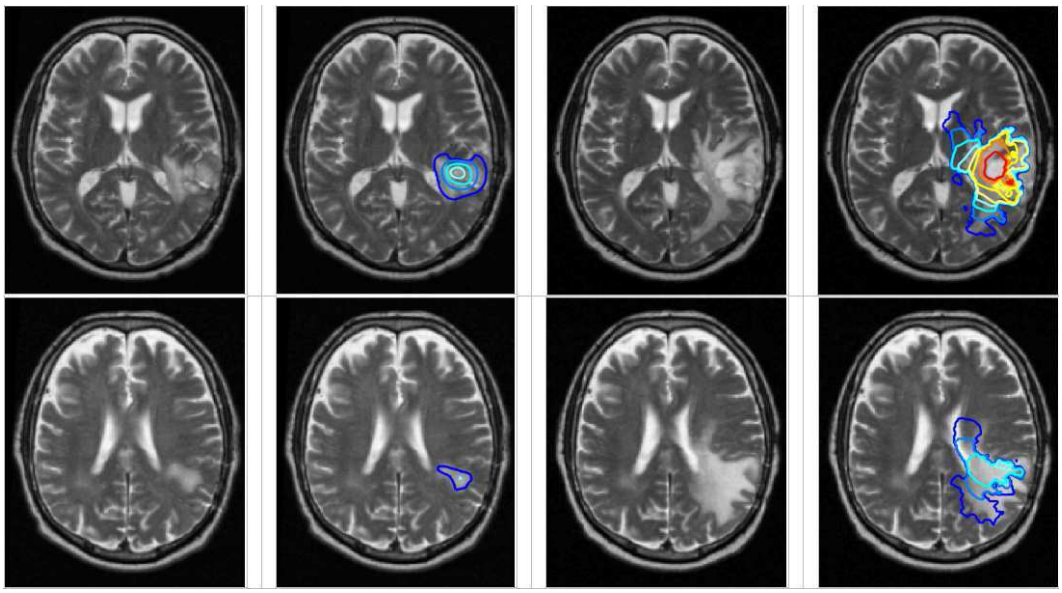

Figure 3.4: The first mechanical model that uses a complete reaction-diffusion equation with anisotropic diffusion to formulate the growth. The cloud-like tumor shape is captured due to the anisotropic diffusion. Brain tissue deformation is obtained by modeling the mass effect. First two columns show the initial image and the initial state of the model respectively, while the third column shows the tumor after 6 month and the colored contours in the fourth column show the growth result in time using the model given by Clatz et al. [13]. The rows correspond to two different slices of a 3D image. (Image from [13])

Clatz et al. [13], for the first time, considered a complete reaction-diffusion equation for the growth part of a mechanical model. So they combined the proliferation, anisotropic diffusion and mass effect together. They considered the brain tissue as a visco-elastic material that can be modeled using a static equilibrium equation. Two different mass effects were established in their model, one for tumor and the other for edema. The bulk tumor mass effect was considered as a homogenous pressure caused by mass increase. The mass effect of tumor-infiltrated-edema included the effect of invasion through a stress term. They evaluated their model on one real MRI data showing the growth in time (figure 3.4). Hogea et al. [32] also extended their mechanical formulation based on Eulerian framework using a complete reaction-diffusion growth term [33]. They later used this general framework for patient specific parameter estimation [35] and also for image registration [34]

3.5 Conclusion

In this chapter, we reviewed some works on mathematical modeling of the brain tumor growth process. This area of research is vast with numerous projects. In this review, our goal was to highlight those approaches that are most relevant to our project. We classified the literature in two general classes, microscopic and microscopic, depending on the scale of observation. Each class is, in turn,

subdivided into subclasses.

Tumor growth is a complex phenomenon and despite all the efforts and progress in mathematical modeling of tumor growth, there are still several problems in evaluating these models and introducing more accurate ones. The first problem is the lack of knowledge on real behaviour of tumor cells in brain. *In-vivo* and *in-vitro* experiments can only give a rough insight of what is happening in reality. A more important problem is the lack of opportunity to test the developed treatment models on patients. For example, a certain drug or therapy planning can only be evaluated reliably if it is tested on patients. But this might put the patient's health in danger and it is not always possible. Another shortcoming is due to limitations in imaging techniques. Each imaging technique has a threshold of detection. Above this threshold the tumour is observable, while below the threshold it is not. Currently CT images can only detect those parts where the number of tumor cells in each voxel is above a certain level (1-40$\%$ of the maximum number of tumor cells that brain parenchyma can hold [67]). No research has been done to define the detection threshold in MRI images, but the visible extent of the tumor is very close to what is observed in CT images. If imaging techniques were capable of detecting all invaded cells, the enhanced margin could be directly used in radiation planning and there would be no need to define a mathematical model to compute the tumor invasion margin. Progress of imaging techniques, linking microscopic and macroscopic scale observations and introducing a standard validation methodology can enhance the results of tumor growth models.

Chapter 4

Theory

4.1 Introduction

In this chapter, we will introduce two mathematical tumor growth models using diffusion tensor imaging data. These models formulate the physical behaviour of tumor growth into a mathematical format. We start by transferring the biological and physical facts of tumor growth into a general equation and then solve this equation in different ways. Two main proposed models are anisotropic diffusion growth (Section 4.2.4) and geodesic distance models (Section 4.4). The formulation and proposed solution of these two models are explained in detail. We also introduce different functions for transforming water diffusion tensor data to tumor diffusion tensor data.

4.2 Tumor Growth Formulation

Macroscopic tumor growth models use the information obtained from imaging techniques to mathematically formulate the growth. Most macroscopic models focus on two different characteristics of biological behaviour of tumor growth: infiltration and proliferation. So we can formulate the tumor growth in time in the format of a simple equation:
Rate of change of tumor cell density = Diffusion (motility) of tumor cells + Growth of tumor cells.
This simple equation was turned to a mathematical formulation by Murray [54] in 1989. The first term of the equation illustrates the diffusive nature of the tumor reflecting the fact that tumor cells infiltrate into the surrounding brain tissue. The second term is a function representing a reactive behaviour that primarily accounts for tumor cell proliferation and death. This combination results in a partial differential equation (PDE), called reaction-diffusion equation that is solved on the geometry of the brain. In the following sections, we discuss each of these components and the overall equation in detail.

4.2.1 Tumor Diffusion

Tumor cells move gradually to the surrounding tissue. There is a hypothesis that tumor cells move similarly to water molecules [41]. Hence, to define the motion direction of tumor cells, one needs

to define the motion direction of water molecules. The motion of water molecules can be represented by Brownian motion X_t . Brownian motion in Euclidean space is the simplest Markov process whose stochastic behaviour is defined by its initial distribution μ and its transition mechanism. Transition mechanisms are determined by a probability density function p or an infinitesimal generator $\mathcal{L}$. The infinitesimal generator characterizes the Brownian motion as a molecular diffusion process. Here we first explain the diffusion processes and then define the relation between Brownian motion and the diffusion process for water molecules.

Physical background of diffusion processes

Intuitively, diffusion is a physical process that equilibrates concentration differences without creating or destroying mass. This physical observation can be easily shown in a mathematical formulation. The equilibration property is expressed by Ficks law:

$$\mathbf{j} = -\mathbf{D}\nabla u \tag{4.1}$$

This equation states that a concentration gradient ∇u causes a flux **j** that aims to compensate for this gradient. The relation between ∇u and **j** is described by the diffusion tensor **D**, a positive definite symmetric matrix. The case where **j** and ∇u are parallel is called isotropic. Then we may replace the diffusion tensor by a positive scalar value. In the general anisotropic case, **j** and ∇u are not parallel. The observation that diffusion only transports mass without destroying it or creating new mass is expressed by the continuity equation.

$$\frac{\partial u}{\partial t} = -\mathrm{div}\mathbf{j} \tag{4.2}$$

where t denotes the time. If we plug in Ficks law into the continuity equation we end up with the diffusion equation

$$\frac{\partial u}{\partial t} = \mathrm{div}(\mathbf{D}\nabla u) \tag{4.3}$$

This equation appears in many physical transport processes. Two major examples are heat transfer in fluid mechanics and diffusive filters in image processing. In the concept of diffusion MRI, diffusion of water molecules in biological tissues is an anisotropic process. Its anisotropic behaviour shows the complex microstructure of brain and the neural tracts. The general diffusion equation can be thought of as a Brownian process, written as:

$$\frac{\partial u}{\partial t} = \mathrm{div}(\mathbf{D}\nabla u) = \mathcal{L}u \tag{4.4}$$

where u corresponds to the concentration of water molecules in each voxel volume and $\mathcal{L}$ is the infinitesimal operator of the Brownian motion process.

4.2.2 Tumor Proliferation

The penetration of tumor cells to the surrounding tissue is not the only cause of the tumor growth. Tumor cells divide and make new cells while moving to other tissues. Tumor growth due to this net

cell division is represented by a differential equation in time.

$$\frac{\partial u}{\partial t} = f(u) \tag{4.5}$$

where f is a function representing the temporal evolution pattern of the growth and u is the (normalized) tumor cell density. Different functions have been suggested to model tumor proliferation [36], including:

$$\begin{aligned} f(u) &= \rho u && \text{(Exponential Proliferation)} \\ f(u) &= \rho u \tfrac{u_m - u}{u_m} && \text{(Verhulst or logistic law)} \\ f(u) &= \rho u \ln\left(\tfrac{u_m}{u}\right) && \text{(Gompertz law)} \end{aligned} \tag{4.6}$$

where u_m is the maximum value of tumor cell density and ρ corresponds to the proliferation rate of tumor cells. For the exponential model, ρ is the relative increase of cell concentration per time unit (usually day). In most approaches, an exponential model in the simple format of ρu or $\rho u(1-u)$ is used [39], [40], [36], [13]. This is due to fact that none of the functions introduced in 4.6 are proved to model the proliferation behaviour correctly. Hence, the simplest model is preferred to be used in most of the approaches. In this work, we also choose the simple exponential (linear) proliferation function.

4.2.3 General Tumor Formulation

The general partial differential equation (PDE) of tumor growth model is written as the combination of proliferation (time component) with diffusion (space component) of tumor cells. Another term is added representing the effect of the tumor treatment. This equation is called reaction-diffusion equation in literature.

$$\begin{cases} \frac{\partial u}{\partial t} = \underbrace{\operatorname{div}(\mathbf{D}\nabla u)}_{\text{DiffusionTerm}} + \underbrace{f(u)}_{\text{ProliferationTerm}} - \underbrace{T(u)}_{\text{Treatmentlaw}} \\ \\ \mathbf{D}\nabla u.\vec{n}_{\partial\Omega} = 0 \end{cases} \tag{4.7}$$

where the second row defines the Neumann boundary conditions; Ω shows the domain (image) and $\partial\Omega$ is its boundary. Some approaches ([51], [35] and [13]) also add the effect of tumor growth on the deformation of surrounding tissue to the formulation. This tissue deformation is known as mass effect.

4.2.4 Tumor Invasion Margin as the Isocontours of Tumor Cell Concentration

Most approaches in macroscopic modeling of tumor growth solve the general reaction-diffusion PDE (equation 4.7). The result will show the increase of tumor cell concentration for different tissues in time (usually defined in *days* format). The difference of these approaches is based on the type of diffusion tensor they use (this part is described in detail in Section 4.3), the proliferation

function and whether or not they include any mass effect or treatment plan. Another difference of various growth models is the choice of the numerical method of implementation. Some approaches use finite element method to include the mechanical changes such as mass effect into the modeling, while other methods solve the equation using finite differences.

Our Approach

The first method we introduce to find the tumor invasion margin is based on the general equation 4.7. For the diffusion tensor **D**, we use a function of water diffusion tensors obtained from DTI data (described in detail Section 4.3). In addition, we use the exponential proliferation model and we do not consider the treatment planning. The whole equation is simplified as:

$$\begin{cases} \frac{\partial u}{\partial t} = \operatorname{div}(\mathbf{D}.\nabla u) + \rho u \\ \\ \mathbf{D}\nabla u.\vec{n}_{\partial\Omega} = 0 \end{cases} \tag{4.8}$$

In this equation, we consider u as the normalized tumor cell density ($u \in [0, 1]$). To keep u below 1 in existence of proliferation, we consider a free boundary problem. The areas inside the visible part of the tumor in reference time get the initial value 1 and the other voxels get the value 0. The voxels inside the initial tumor area are also regarded as boundary voxels, so they keep their value $u = 1$ during all iterations.

A fundamental difference of our approach with others is that we do not intend to define the tumor growth in time. Instead, we would like to find the tumor invasion margin. But how can we define the tumor invasion margin?

The part of the tumor that is observed in the MRI images is called the tumor delineation area. Based on [39], the detection limit in T2 weighted CT images is defined as 5% of the maximum number of cells that tumor parenchyma can hold. The detection limit of MRI images in not known yet but since CT and MRI images enhance the same area, we can consider the same limit for MRI images. So the tumor invasion margin corresponds approximately to the remaining 5% of the tumor that is not visible in the MRI image; we plan to detect this area. By solving (4.8), we define the tumor cell concentration for all voxels in time. The voxels containing similar tumor cell densities form an isocontour around the initial tumor delineation area. It is not yet medically clear what value of tumor cell density defines the tumor invasion margin. Also it is unknown to what extend we should grow the tumor to find the invasion margin, e.g. one can grow the tumor to the volume size defined by the 2cm Euclidean distance model and then stop the growth and consider the delineated area as the tumor invasion margin. Finally, we need to solve equation 4.8 with a stable numerical method to define tumor cell density and invasion margin. Details on the numerical solution are given in Chapter 5.

4.3 Brain Tumor Diffusion Tensor Model

In Section 4.2.4, we stated that one of the key differences of tumor growth approaches is based on the type of diffusion tensor they pick. In early attempts to formulate glioma growth with reaction-diffusion equation, the tensors were considered equally isotropic all over the brain [16]. This kind of tensors would allow tumor cells to diffuse equally in all directions. This diffusion tensor model in the brain can be written as:

$$DT_1(x) = \begin{cases} d, & x \in \text{gray matter} \\ d, & x \in \text{white matter} \end{cases} \tag{4.9}$$

where d is a constant value and x represents the voxel location in brain.

A significant change in growth models occurred when Swanson et al. [64] [65] introduced different motilities of tumor cells in gray and white matters. Their model was based on the hypothesis that tumor cells move faster in white matter compared to gray matter. This diffusion tensor model can be written as:

$$DT_2(x) = \begin{cases} d_g, & x \in \text{gray matter} \\ d_w = \alpha d_g, & x \in \text{white matter} \end{cases} \tag{4.10}$$

where α is a value between 0 and 100. This model is numerically simple to solve since it is still isotropic. Hence, it is used even in fairly recent approaches [33], [39], [35]. The next stage of progress in growth models happened when anisotropy was included in the mechanism of tumor cell infiltration (Clatz et al. [13], Jbabdi et al. [36] and recently Konukoglu et al. [40]). By including the anisotropy into the tumor diffusion formulation, these models were able to better capture the "spiky" tumor shapes usually observed in MRI scans. They assume that tumor cells not only move faster on myelin compared to gray matter, but also they follow the white matter tracts of the brain. Based on the hypothesis that tumor cells diffuse in the direction of diffusion of water molecules [41], D can be replaced with a function the water diffusion tensor obtained from diffusion tensor imaging (DTI).

$$DT_3(x) = D_w, \quad x \in \text{gray or white matter} \tag{4.11}$$

However, the tumor diffusion tensor (TDT) is not exactly the same as the water diffusion tensor but can be expressed as a function of water diffusion tensor $DT_4(x) = f(D_w)$. The main idea in constructing the TDT is to assign isotropic diffusion in gray matter and anisotropic diffusion in white matter. While this should be directly reflected by the diffusion tensors (D_w) magnitude, due to noise and discretization problems it is not. Also different motilities of tumor cells in gray and white matter is not reflected by water diffusion. The proposed transformation of water tensors from DTI data into TDT is rather heuristic. Clatz et al. [13] and Konukoglu et al. [40] used isotropic tensors in gray matter and water tensors in white matter scaling their value with constraint $d_w > d_g$:

$$DT_5(x) = \begin{cases} d_g I, & x \in \text{gray matter} \\ d_w D_{water}, & x \in \text{white matter} \end{cases} \tag{4.12}$$

where I is the identity matrix. Jbabdi et al. [36] suggested the following model to increase the tensor anisotropy without changing its orientation and also favouring the appropriate orientations

when fiber crossing occurs.

$$DT = a_1\lambda_1\mathbf{e}_1\mathbf{e}_1^T + a_2\lambda_2\mathbf{e}_2\mathbf{e}_2^T + a_3\lambda_3\mathbf{e}_3\mathbf{e}_3^T \tag{4.13}$$

where λ_1 to λ_3 and $\mathbf{e}_1$ to $\mathbf{e}_3$ are respectively eigenvalues and eigenvectors in the decreasing order and a_is are defined as:

$$\begin{pmatrix} a_1 \\ a_2 \\ a_3 \end{pmatrix} = \begin{pmatrix} r & r & 1 \\ 1 & r & 1 \\ 1 & 1 & 1 \end{pmatrix} \begin{pmatrix} c_l \\ c_p \\ c_s \end{pmatrix} \tag{4.14}$$

The anisotropy change is controlled by the factor r. c_l, c_p and c_s are respectively, the linear, planar and spherical indices for the tensor; defined as

$$c_l = \frac{\lambda_1-\lambda_2}{\lambda_1+\lambda_2+\lambda_3}, \quad c_p = \frac{2(\lambda_2-\lambda_3)}{\lambda_1+\lambda_2+\lambda_3}, \quad c_s = \frac{3\lambda_3}{\lambda_1+\lambda_2+\lambda_3}$$

We tried to find the best mapping function from the real data that we had. Clatz's model (4.12) is not so practical since it needs a "Patient to Atlas" registration to differentiate between gray and white matter regions. Jbabdi's model (4.13) is better in a sense that it is directly applied to the extracted tensors and it does not need any additional registration. However, our experimental results on real patient DTI data shows that a linear function FA values can produce better results. FA represents the normalized fractional anisotropy computed from tensor data.

$$D(x) = \alpha\ f(FA)\ D_w, \quad x \in \text{gray/white matter} \tag{4.15}$$

where $f(FA)$ is a linear function of FA values.

Our proposed model is also heuristic. For future work, we propose a more principled way of modeling the TDT in the form of a function learned from tumor growth observations for various patients from several MRI scans.

4.4 Tumor Invasion Using Geodesic Distance on Brain Fiber Manifold

So far, we have shown the growth formulation that gives the concentration of tumor cells in each image voxel in time. As mentioned, in this project we are interested in finding the tumor invasion margin. The current radiation therapy practice is to use the MRI segmented tumor area and measure a 2cm straight-line Euclidean distance outward from the segmented contour as the invasion margin. In this section, we introduce a new method that directly calculates the cell infiltration isocontours as a format of a distance function from the original tumor location. These isocontours define a map of the brain where every location is marked with the 'time' it would take glioma cells to reach there from the current tumor location. This way the calculated distance can be directly replaced with the Euclidean distance in the radiation treatment planning software.

The proposed method calculates geodesic distance on the Riemannian manifold of brain fibers to

model the anisotropic tumor growth. O'Donnell et al. [55] and Lenglet et al. [45] introduced the formulation of the white matter as a Riemannian manifold characterized by the infinitesimal anisotropic diffusion operator. They made the link between the diffusion tensor data D and the white matter manifold geometry and showed that the diffusion operator can be associated with a metric $G = D^{-1}$. This metric allows computation of geodesic path and distances between points on the brain that was used in [45] for fiber connectivity.

To explain this geometric idea, we employ an analogy with city traffic. Using the Euclidean distance for tumor margin corresponds to the assumption that it takes the same time to drive to any point on a city map at a particular radius from home. However, transport time to a certain point in a city depends to a large extent on the road net geometry and traffic flow. The same is true for glioma spread, which depends on the brain structures in its vicinity. The DTI technique gives us the key to design a road-map of the brain. We make maps that consistently mark every 3D voxel (space unit) in the brain with the time it would take glioma cells to reach there from the current tumor. The mathematically correct way to do this is to compute a geodesic distance on a Riemannian (curved) manifold of brain fibers.

A remarkable advantage of this new formulation is that it is numerically more stable, as it results in a first order PDE as opposed to the second order anisotropic diffusion PDE. The numerical stability issues are explained in detail in Section 5.

4.4.1 Geometry of Manifold from Diffusion Processes

To define the manifold geometry from the water diffusion process, we briefly repeat some notions from the beginning of this chapter. As we mentioned, we represent the motion of water molecules by Brownian motion X_t. Transition mechanisms are determined by a probability density function p or an infinitesimal generator $\mathcal{L}$. The infinitesimal generator characterizes the Brownian motion as a molecular diffusion process (equation 4.4).

$$\frac{\partial u}{\partial t} = \mathrm{div}(\mathbf{D}\nabla u) = \mathcal{L}u$$

Lenglet et al. [45] show that under some technical hypothesis on $\mathcal{L}$ (with its domain of definition $D(\mathcal{L})$) and on the Brownian motion X_t, it is possible to define an $\mathcal{L}$-diffusion process on a Riemannian Manifold *M* from the d-dimensional stochastic process X_t. Here we follow their theory on building the connection between $\mathcal{L}$-diffusion process and the Riemannian Manifold. The main focus is on the case of diffusion processes with time-independent infinitesimal operator $\mathcal{L}$ that is assumed to be smooth and non-degenerate elliptic. We define the Laplace-Beltrami differential operator for a function f on a Riemannian manifold *M*

$$\Delta_M f = \mathrm{div}(\mathrm{grad} f) \tag{4.16}$$

In local coordinates, the Riemannian metric is written as

$$ds^2 = g_{ij} dx_i dx_j \tag{4.17}$$

and the Laplace-Beltrami operator becomes

$$\Delta_M f = \frac{1}{\sqrt{G}} \frac{\partial}{\partial x_j} \left(\sqrt{G} g^{ij} \frac{\partial f}{\partial x_i} \right) = g^{ij} \frac{\partial^2 f}{\partial x_i \partial x_j} + b^i \frac{\partial f}{\partial x_i} \tag{4.18}$$

where G is the determinant of the matrix $\{g_{ij}\}$ and $\{g^{ij}\}$ its inverse. Moreover,

$$b^i = \frac{1}{\sqrt{G}} \frac{\partial(\sqrt{G} g^{ij})}{\partial x_i} \tag{4.19}$$

We can omit the second term of 4.18, since Δ_M is second order, strictly elliptical.

Definition: The operator $\mathcal{L}$ is said to be an intrinsic Laplacian generating a Brownian motion on M if

$$\mathcal{L} = \frac{1}{2} \Delta_M$$

For a smooth and non-degenerate elliptic differential operator on M, $\mathcal{L}$ is written as

$$\mathcal{L} = \frac{1}{2} d_{ij} \frac{\partial^2}{\partial x_i \partial x_j} \tag{4.20}$$

which concludes in the following lemma:

Lemma: If $\left\{d^{ij}\right\}_{i,j=1\ldots d}$ denotes the inverse matrix of $\mathbf{D} = \{d_{ij}\}_{i,j=1\ldots d}$ then $g = d^{ij} dx_i dx_j$ defines a Riemannian metric g on M.

Conclusion: This ends up in a very important concept in diffusion tensor imaging, that the diffusion tensor **D** estimated at each voxel point, after inversion, defines the metric of the manifold. In this way, the link between the diffusion tensor data and the manifold geometry of brain fibers is made.

$$\mathbf{G} = \mathbf{D}^{-1} \tag{4.21}$$

Now that we have the metric of the manifold, we are able to define the tumor invasion margin as the distance from the initial tumor location on the Riemannian Manifold *M*. The idea is that water molecules starting from a given point x_0 on M can reach to any point x on *M* through a geodesic under Brownian motion. Here, the geodesic distance between the two points shows the pathway of molecular Brownian motion (fibers in the brain).

We can compute these geodesics using the metric g of the manifold. Let us define Riemannian distance from a fixed starting point $x_0 \in M$ to another point x on the manifold as $r(x) = \phi(x_0, x)$ where $r : M \to \Re_+$. Based on [45], under the assumption that *M* is geodesically complete, there is a unique distance minimizing the geodesic between each two point on the manifold. The distance function is Lipschitz on all *M*, smooth on M/Cut_{x0} where Cut_{x0} is the location of all the points where the geodesic starting orthonormally from x_0 stops being optimal for the distance. The distance function on M/Cut_{x0} has the property $|\mathrm{grad}\phi(x)| = 1$ where $\mathrm{grad}\phi(x)$ denotes the gradient of the distance function on the tangent plane of the manifold. This results in the general definition of the distance function.

Theorem

The distance function ϕ from a non-empty closed subset K is the unique viscosity solution of the Hamilton-Jacobi equation [45]

$$\begin{cases} |\text{grad}\phi| = 1 & \text{in} \quad M \backslash K \\ \phi(x) = \phi_0(x) & \text{for} \quad x \in K \end{cases} \tag{4.22}$$

where $\phi_0(x) = 0 \; \forall x \in K$ in the class of bounded uniformly continuous functions. This is a well-known eikonal equation on the Riemannian Manifold (*M,g*).

The general format of this Hamilton-Jacobi equation with Dirichlet boundary condition is written as

$$\begin{cases} H(x, D\phi(x)) = 0 & \text{in} \quad M \backslash K \\ \phi(x) = \phi_0(x) & \text{for} \quad x \in K \end{cases} \tag{4.23}$$

where the Hamiltonian $H : M \times T^*M \rightarrow \Re$ is a continuous real function on the cotangent space of the manifold (T^*M) . Equation 4.22 is achieved by setting $H(x, D\phi(x)) = |grad(\phi(x))| - 1$ in 4.23. We denote by $|\nu|$ the magnitude of a vector ν of TM (tangent plane of M), defined as $\sqrt{g(\nu, \nu)}$. In matrix notation by forming $\mathbf{G} = \{g_{ij}\}$ the metric tensor, this writes as $\sqrt{\nu^T \mathbf{G} \nu}$.

4.4.2 A Levelset Formulation for Distance Function

The viscosity solution ϕ at $x \in M$ of equation 4.22 is not a smooth solution. But it has the property that it is the minimum time $t \geq 0$ for any curve γ to reach a point $\gamma(t) \in K$ starting at x with the condition $\gamma(0) = 0$ and $\left|\frac{\partial \gamma}{\partial t}\right| \leq 1$. Based on this fact, equation 4.22 can be solved as a dynamic problem and we can apply a level set methods for its numerical solution [45].

The level set formulation introduces the use of an implicit function of one higher dimension to solve the dynamic equation. In this way, the problems of instabilities, deformation of surface elements and topological changes are avoided. In the level set formulation, the distance function ϕ is the zero level of an implicit smooth function $\psi(x, t)$ at time t. $\psi(x, t)$ is a compact surface of higher dimension, which divides M into $\Gamma \in M$ and its complement $\Gamma^c \in M$. We call Γ the interior part (which means points of the manifold that have already been visited) and Γ^c the exterior (the points not visited). So $\psi(x, t)$ has the following property at $t = 0$

$$\begin{cases} \psi(x, 0) = 0 & \Leftrightarrow x \in \phi_0 \\ \psi(x, 0) > 0 & \forall x \in \Gamma \\ \psi(x, 0) < 0 & \forall x \in \Gamma^c \end{cases} \tag{4.24}$$

$\psi(x, 0)$ is a uniformly continuous and monotonic strictly decreasing function of distance near ϕ_0. We can initialize ψ with a Euclidean signed distance function. We require ϕ_t to evolve so that:

$$\psi(x, t) = 0 \Leftrightarrow t = \phi(x) \tag{4.25}$$

The levelset generated by 4.25 is the viscosity solution of 4.22 if ψ is the viscosity solution of [45]

$$\begin{cases} \psi_t + F(t, x, D\psi(t, x)) = 0 \quad \forall t > 0 \\ \psi(x, 0) = \psi_0(x) \end{cases} \tag{4.26}$$

$F > 0$ does not change sign and it is defined as

$$F(t, x, D\psi) = H(t, x, D\psi) + 1$$

So equation 4.26 becomes

$$\begin{cases} \frac{\partial \psi}{\partial t} + |\mathrm{grad}\psi| = 0 \quad \forall t > 0 \\ \psi(x, 0) = \psi_0(x) \end{cases} \tag{4.27}$$

where ψ_0 is the signed distance function of ϕ_0. The viscosity solution of this PDE gives us the distance function as the zero level of ψ in time.

4.4.3 Geodesic Distance Calculation

To numerically solve hyperbolic Hamilton-Jacobi Equation 4.27, we first clarify the term $|\mathrm{grad}\psi|$. In particular the gradient operator on the tangent plane of a manifold is defined as

$$\mathrm{grad} f = \mathbf{G}^{-1} df$$

Section 4.4.1 defines the magnitude of a vector on the tangent space of a Riemannian manifold. Based on this notion we have:

$$\begin{aligned} |\mathrm{grad}\psi|^2 &= (\mathrm{grad}\psi)^T \mathbf{G}\, \mathrm{grad}\psi \\ &= (\mathbf{G}^{-1} D\psi)^T \mathbf{G} (\mathbf{G}^{-1} D\psi) \\ &= D\psi^T \mathbf{G}^{-1} D\psi \end{aligned} \tag{4.28}$$

where $D\psi$ is the first order differential of ψ, which can be extended in

$$|\mathrm{grad}\psi|^2 = \sum_{k=1}^{3} \sum_{l=1}^{3} \frac{\partial \psi}{\partial x_l} \frac{\partial \psi}{\partial x_k} g^{kl} \tag{4.29}$$

where $g^{lk} = g_{kl}^{-1}$.

We need a consistent and stable numerical method to discretize equation 4.27. The stability and consistency of the numerical scheme is explained in detail in Chapter 5. Here we just mention that approximating the continuous flux $|\mathrm{grad}\psi|^2$ with following upwind method provides a consistent numerical solution.

$$\begin{aligned} |\mathrm{grad}\psi|^2 = \; & \sum_{i=1}^{3} g^{ii} \left(\max(D_{x_i}^{-}\psi, 0)^2 + \min(D_{x_i}^{+}\psi, 0)^2 \right) + \\ & \sum_{i \neq j, i, j=1}^{3} g^{ij} \mathrm{minmod}(D_{x_i}^{+}\psi, D_{x_i}^{-}\psi) \mathrm{minmod}(D_{x_j}^{+}\psi, D_{x_j}^{-}\psi) \end{aligned} \tag{4.30}$$

where $\left(g^{ij}\right)_{i,j=1\ldots3}$ are components of the inverse matrix $\mathbf{G}^{-1}$ and $D_{x_i}^{\pm}\Psi$ are forward/backward approximation of the gradient of Ψ in x_i and $\mathrm{minmod}(a, b) = \min(a, 0) + \max(b, 0)$.

When using the geodesic distance in the context of growth prediction, the subset K from where we initiate the growth, represents the visible tumor margin. In addition, as the brain contains several obvious natural barriers to glioma growth such as the skull, ventricular system, the tentorium cerebelli and the falx cerebri, M is defined as the brain volume that does not contain those barriers. Starting

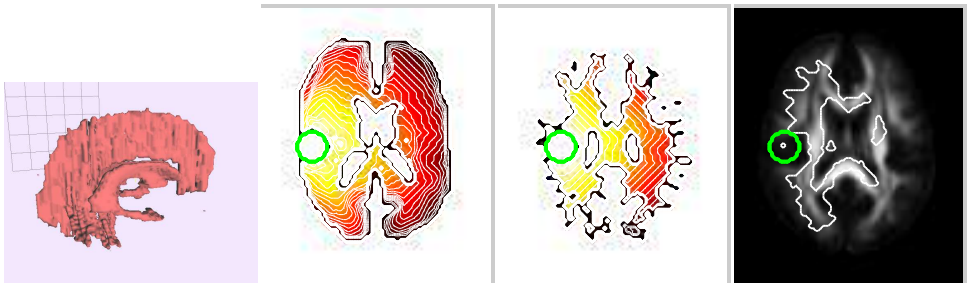

(a) Barriers (b) Geod esicdist. (c) Geodesic dist. on white matter (d) Geodesic dist. isocontour on FA

Figure 4.1: The result of applying the geodesic distance model to a DTI atlas. Colors show the geodesic distance from the initial position.

the growth from K, in each iteration the zero levelset of ψ defines the distance corresponding to $t = i$ (i is the iteration number), we can stop the growth whenever we have reached the desired margin. Fig. 4.1(a) shows an example of segmented barriers (ventricles, falx, tentorium). Fig. 4.1(b-d) shows examples of geodesic distance computed on the ICBM DTI-81 atlas [46]: (b) shows the geodesic distance computed with linear tensor weighting that originates from a sphere (green circle in the figure) until reaches the skull boundary. (c) shows the geodesic distance computed only in the white matter tensors instead of the whole brain tensors; (d) shows an isocontour of the geodesic distance aligned with FA values. Notice how the distance follows the fiber directions.

4.5 Conclusion

In this chapter, we discussed the theory and mathematical formulation of two different tumor growth models for defining the tumor invasion margin. The first model is based on solving the general reaction-diffusion equation with a stable numerical method. The resulting tumor cell density map is used to define the isocontours of same concentration around the tumor. These isocontours correspond to the later time tumor delineation area observed in MRI images. The other method we introduced, links the tumor diffusion to a Riemannian manifold on brain fibers and defines the isocontours of tumor growth as geodesic distances on the manifold. We also surveyed different functions used in literature to map water diffusion tensors to tumor diffusion tensors and introduced our new approach.

Chapter 5

Stability Study for the Numerical Implementation

5.1 Introduction

Numerical methods used for solving differential equations should be chosen with great care. Not considering numerical aspects such as stability, consistency and wellposed-ness could result in erroneous solutions. One of the most important aspects that should be considered is the *stability* of the numerical method. According to standard textbook definition (e.g. [30]), in studying differential equations, a numerical method is said to be *stable* if small perturbations in the input data or the ones that occur during computation do not cause the resulting numerical solution to diverge away without bound. In other words, a numerical method is *stable* if the numerical solution at any arbitrary but fixed time t remains bounded [30].

The divergence of the numerical solution could be either caused by instability of the solution of the differential equation or by the numerical method itself even when the solution to the differential equation is stable. In this chapter, we discuss stability issues of different numerical methods that can be applied to solve differential equations we obtained in Chapter 4 to model the tumor growth.

5.2 Numerical Aspects for Solving Diffusion Equation

As we discussed in Chapter 4, the most accepted hypothesis regarding tumor growth is to model the growth as a diffusion-proliferation process. The mathematical modeling of this process results in a second order parabolic partial differential equation. To simulate the tumor growth in time, we need to solve this PDE using a numerical method. Different numerical methods can be used for this purpose. The most well-known ones are finite difference and finite element methods.

Most implementations of nonlinear diffusion processes used in image processing are based on finite differences. An example is nonlinear diffusion filtering. The main reason is that a finite difference scheme is easy to implement. Also, the pixel structure of digital images provides a natural regular grid. On the other hand, this method can easily get unstable especially for diffusion processes that

are anisotropic and nonlinear. Hence, the finite difference method should be used carefully.
In this chapter, we try to carefully assess the stability of different finite difference methods used to discretize and solve diffusion equation. We first start from a simple linear diffusion model and gradually extend the stability concept to the isotropic and anisotropic nonlinear diffusion cases. We will first make all the definitions for the 2D case following Weickert [72] and then present our extension to the 3D case.

5.2.1 Linear Diffusion Process, Numerical Aspects

The diffusion equation that we explained in Chapter 4

$$\frac{\partial u}{\partial t} = \mathrm{div}(D\nabla u)$$

is called homogenous or linear, if the diffusion tensor D is constant over the whole spatial domain. In other words, in the linear diffusion, the diffusion tensor is an identity matrix and the diffusion equation can be written as

$$\frac{\partial u}{\partial t} = \mathrm{div}(\alpha I \nabla u) = \alpha \Delta u \tag{5.1}$$

without loss of generality α can be dropped and the equation is written as

$$\partial_t u = \partial_{xx} u + \partial_{yy} u \tag{5.2}$$

in the 2D case. To discretize this equation using finite difference approximations, the first and second order derivatives in (x_i, y_j, t_k) are replaced with

$$\begin{aligned} \partial_t u &= \frac{u_{i,j}^{k+1} - u_{i,j}^k}{\tau} + O(\tau) \\ \partial_{xx} u &= \frac{u_{i+1,j}^k - 2u_{i,j}^k + u_{i-1,j}^k}{h_1^2} + O(h_1^2) \end{aligned} \tag{5.3}$$

where τ and h_1 are time and space discretization steps respectively. Replacing them in equation 5.2 results in

$$\frac{u_{i,j}^{k+1} - u_{i,j}^k}{\tau} = \frac{u_{i+1,j}^k - 2u_{i,j}^k + u_{i-1,j}^k}{h_1^2} + \frac{u_{i,j+1}^k - 2u_{i,j}^k + u_{i,j-1}^k}{h_2^2} \tag{5.4}$$

The unknown $u_{i,j}^{k+1}$ at time $k+1$ can be computed explicitly (i.e., without solving a system of equations) from five known values at level k:

$$u_{i,j}^{k+1} = (1 - 2\frac{\tau}{h_1^2} - 2\frac{\tau}{h_2^2})u_{i,j}^k + \frac{\tau}{h_1^2}u_{i+1,j}^k + \frac{\tau}{h_1^2}u_{i-1,j}^k + \frac{\tau}{h_2^2}u_{i,j+1}^k + \frac{\tau}{h_2^2}u_{i,j-1}^k \tag{5.5}$$

where h_1 and h_2 are grid sizes in x and y direction. This method is therefore called explicit finite difference scheme where solution at time step $k+1$ depends only on the values of the solution at time k. The spatial weights can be written in the following 3×3 stencil format

0	$\frac{\tau}{h_2^2}$	0
$\frac{\tau}{h_1^2}$	$1 - \frac{\tau}{h_1^2} - 2\frac{\tau}{h_1^2}$	$\frac{\tau}{h_2^2}$
0	$\frac{\tau}{h_2^2}$	0

Now we should assess the stability of this method. Based on the definition of stability, the numerical solution at any arbitrary but fixed time t should remain bounded. A restricted requirement is to satisfy the Maximum-Minimum principle:

$$\min_{n,m} f_{n,m} \;\leq\; u_{n,m}^{k+1} \;\leq\; \max_{n,m} f_{n,m} \quad \forall\, k \geq 0,\;\; \forall\, i,j \tag{5.6}$$

where f is the initial value: $f_{n,m} = u_{n,m}^{0}$. To check the maximum-minimum principle we first observe that stencil weights sum up to one. So if all the weights are nonnegative, we will obtain a stable convex combination satisfying the maximum-minimum principle. We observe that all non-central weights are non-negative. A non-negative central weight means that $1 - 2\frac{\tau}{h_1^2} - 2\frac{\tau}{h_2^2} \geq 0$ which leads to a stability condition on the time step size τ

$$\tau \leq \frac{1}{\frac{2}{h_1^2} + \frac{2}{h_2^2}} \tag{5.7}$$

So the finite difference model is stable for the linear diffusion equation if the time stability is satisfied.

5.2.2 Nonlinear Diffusion Processes, Numerical Aspects

In the nonlinear diffusion process, the diffusion tensor is a variable of the spatial domain. We emphasize that our definition of nonlinearity here, does not necessarily mean that D is a nonlinear function of u but rather that D is a spatially varying function. If D is an isotropic tensor ($D = \alpha I$ where α is a spatially varying parameter), the process is called a non-linear isotropic diffusion process. When D is a full tensor and spatially varying, the process is called a nonlinear anisotropic diffusion process. To study the stability of this model, let us first define the differential problem in detail.

Basic Diffusion Process Structure

Let us consider a rectangular image domain $\Omega := (0, a_1) \times (0, a_2)$ with boundary $\Gamma := \partial\Omega$ and let the tumor cell density in the image be represented by a mapping $f \in L^{\infty}(\Omega)$. The class of anisotropic diffusion processes we are concerned about, is represented by the initial boundary value problem

$$\left.\begin{array}{lll} \partial_t u = \mathrm{div}(D.\nabla u) & on & \Omega \times (0,\infty), \\ u(x,0) = f(x) & on & \Omega, \\ \langle D\nabla u, \vec{n}\rangle = 0 & on & \Gamma \times (0,\infty). \end{array}\right\} P_c \tag{5.8}$$

Here, $\vec{n}$ denotes the outward pointing normal and $\langle ., . \rangle$ the Euclidean scalar product on $\Re^2$. The diffusion tensor $D \in \Re^{2\times 2}$ is obtained from DTI data and satisfies the following properties:

(C1) Smoothness:

$$D \in C^{\infty}(\Re^{2,2} \times \Re^{2,2})$$

(C2) Symmetry

(C3) Positive Definiteness

Under these assumptions, the wellposed-ness of the diffusion equation in the continuous sense can be proved [72].

Theorem1 (Well-poseness, regularity, extremum principle, continuous problem)

The problem (P_c) has a unique solution $u(x,t)$ in the distributed sense, which depends continuously on f and it fulfills the extremum principle

$$a \leq u(x,t) \leq b \quad on \quad \Omega \times (0,T]. \tag{5.9}$$

where

$$\begin{aligned} a &:= \inf_{\Omega} f, \\ b &:= \sup_{\Omega} f \end{aligned} \tag{5.10}$$

5.2.3 Semi-Discrete Diffusion Process

To assess the well-posedness of the semidiscrete problem, let us first define the semidiscrete class of diffusion problems (P_s) in the following way:

$$\left.\begin{array}{l} \text{Let } f \in \Re^N. \text{ Find a function } u \in C^1([0,\infty), \Re^N) \text{ that satisfies an initial value problem of type} \\ \qquad \begin{aligned} \tfrac{\partial u}{\partial t} &= A(u)u, \\ u(0) &= f, \end{aligned} \\ \text{where } A = (a_{ij}) \text{ has the following properties:} \\ \text{(S1)} \quad \text{Lipschitz-continuity of } A \in C(\Re^N, \Re^{N\times N}) \text{ for every bounded subset of } \Re^N \\ \text{(S2)} \quad \text{symmetry:} \qquad a_{ij}(u) = a_{ji}(u) \quad \forall i,j \in J, \quad \forall u \in \Re^N, \\ \text{(S3)} \quad \text{vanishing row sums:} \qquad \textstyle\sum_{j\in J} a_{ij}(u) = 0 \quad \forall i \in J, \quad \forall u \in \Re^N, \\ \text{(S4)} \quad \text{nonnegative off-diagonals:} \qquad a_{ij}(u) \geq 0 \quad \forall i \neq j, \quad \forall u \in \Re^N \end{array}\right\} (P_s)$$

Theorem2 (Well-posedness, extremum principle, semidiscrete problem)

For every $T > 0$ the problem (P_s) has a unique solution $u(t) \in C^1([0,T], \Re^N)$. The solution depends continuously on the initial value and the right-hand side of the ODE system, and it satisfies the extremum principle

$$a \leq u_i(t) \leq b \quad \forall i \in J, \quad \forall t \in [0,T], \tag{5.11}$$

where

$$\begin{aligned} a &:= \min_{j\in J} f_j, \\ b &:= \max_{j\in J} f_j \end{aligned} \tag{5.12}$$

This theorem is proved in [72].

Now we should investigate whether it is possible to use spatial discretization of the continuous filter

$\frac{-b_{i-1,j}-b_{i,j+1}}{4h_1h_2}$	$\frac{c_{i,j+1}+c_{i,j}}{2h_2^2}$	$\frac{b_{i+1,j}+b_{i,j+1}}{4h_1h_2}$
$\frac{a_{i-1,j}+a_{i,j}}{2h_1^2}$	$-\frac{a_{i-1,j}+2a_{i,j}+a_{i+1,j}}{2h_1^2}$ $-\frac{c_{i,j-1}+2c_{i,j}+c_{i,j+1}}{2h_2^2}$	$\frac{a_{i+1,j}+a_{i,j}}{2h_1^2}$
$\frac{b_{i-1,j}+b_{i,j-1}}{4h_1h_2}$	$\frac{c_{i,j-1}+c_{i,j}}{2h_2^2}$	$\frac{-b_{i+1,j}+b_{i,j-1}}{4h_1h_2}$

Table 5.1: Standard 2D stencil; Discretization with this stencil is not guaranteed to be stable since the diagonal boundary stencil elements can become negative

class P_c in order to construct semidiscrete diffusion model of P_s satisfying (S1)-(S4). First we shall indicate that this is easily done for the isotropic case (We refer the reader to [72] for the proof). In the anisotropic case, (S1) to (S3) are satisfied in the same way as isotropic case. However, it is difficult to ensure the nonnegativity (S4) due to the mixed term derivatives. Let us clarify the problem.
The right-hand side of the anisotropic diffusion equation in 2D is written as:

$$\begin{aligned} \operatorname{div}(D\nabla U) &= \operatorname{div}\left(\begin{bmatrix} a & b \\ b & c \end{bmatrix}\begin{bmatrix} \frac{\partial u}{\partial x} \\ \frac{\partial u}{\partial y} \end{bmatrix}\right) \\ &= \frac{\partial(a\frac{\partial u}{\partial x})}{\partial x} + \frac{\partial(b\frac{\partial u}{\partial y})}{\partial x} + \frac{\partial(b\frac{\partial u}{\partial x})}{\partial y} + \frac{\partial(c\frac{\partial u}{\partial y})}{\partial y} \end{aligned} \tag{5.13}$$

The standard discretization using forward-backward differences is obtained by

$$\frac{\partial(a\frac{\partial u}{\partial x})}{\partial x} = \frac{1}{h_1}\left(\frac{a_{i+1,j}+a_{i,j}}{2}\frac{u_{i+1,j}-u_{i,j}}{h_1} - \frac{a_{i,j}+a_{i-1,j}}{2}\frac{u_{i,j}-u_{i-1,j}}{h_1}\right) \tag{5.14}$$

For the mixed term, the standard approximation by central differences results in:

$$\frac{\partial(b\frac{\partial u}{\partial y})}{\partial x} = \frac{1}{2h_1}\left(b_{i+1,j}\frac{u_{i+1,j+1}-u_{i+1,j-1}}{2h_2} - b_{i-1,j,k}\frac{u_{i-1,j+1}-u_{i-1,j-1}}{2h_2}\right) \tag{5.15}$$

This standard discretization results in a stencil of the format of Table 5.1. Is this discretization nonnegative?
If $\begin{pmatrix} a & b \\ b & c \end{pmatrix}$ is positive semi definite, then $a \geq 0$ and $c \geq 0$. However, b may have arbitrary sign. So the sign pattern of the stencil will be

?	+	?
+	−	+
?	+	?

Negative $\boxed{?}$ destroy the nonnegativity condition (S4) for the off-diagonal elements of $A(u)$. So if we apply the standard discretization to the mixed-term derivatives, we will obtain an unstable finite difference method. But the following theorem shows that for a sufficiently large stencil it is always possible to find a nonnegative discretization.

$\frac{\lvert b_{i-1,j+1}\rvert - b_{i-1,j+1}}{4h_1h_2}$ $+\frac{\lvert b_{i,j}\rvert - b_{i,j}}{4h_1h_2}$	$\frac{c_{i,j+1}+c_{i,j}}{2h_2^2} - \frac{\lvert b_{i,j+1}\rvert + \lvert b_{i,j}\rvert}{2h_1h_2}$	$\frac{\lvert b_{i+1,j+1}\rvert + b_{i+1,j+1}}{4h_1h_2}$ $+\frac{\lvert b_{i,j}\rvert + b_{i,j}}{4h_1h_2}$
$\frac{a_{i-1,j}+a_{i,j}}{2h_1^2}$ $-\frac{\lvert b_{i-1,j}\rvert + \lvert b_{i,j}\rvert}{2h_1h_2}$	$-\frac{a_{i-1,j}+2a_{i,j}+a_{i+1,j}}{2h_1^2}$ $-\frac{c_{i,j-1}+2c_{i,j}+c_{i,j+1}}{2h_2^2}$ $-\frac{\lvert b_{i-1,j+1}\rvert - b_{i-1,j+1} + \lvert b_{i+1,j+1}\rvert + b_{i+1,j+1}}{4h_1h_2}$ $-\frac{\lvert b_{i-1,j-1}\rvert + b_{i-1,j-1} + \lvert b_{i+1,j-1}\rvert - b_{i+1,j-1}}{4h_1h_2}$ $+\frac{\lvert b_{i-1,j}\rvert + \lvert b_{i+1,j}\rvert + \lvert b_{i,j-1}\rvert + \lvert b_{i,j+1}\rvert + 2\lvert bi,j\rvert}{2h_1h_2}$	$\frac{a_{i+1,j}+a_{i,j}}{2h_1^2}$ $-\frac{\lvert b_{i+1,j}\rvert + \lvert b_{i,j}\rvert}{2h_1h_2}$
$\frac{\lvert b_{i-1,j-1}\rvert + b_{i-1,j-1}}{4h_1h_2}$ $+\frac{\lvert b_{i,j}\rvert + b_{i,j}}{4h_1h_2}$	$\frac{c_{i,j-1}+c_{i,j}}{2h_2^2} - \frac{\lvert b_{i,j-1}\rvert + \lvert b_{i,j}\rvert}{2h_1h_2}$	$\frac{\lvert b_{i+1,j-1}\rvert - b_{i+1,j-1}}{4h_1h_2}$ $\frac{\lvert b_{i,j}\rvert - b_{i,j}}{4h_1h_2}$

Table 5.2: Non-negative 2D stencil; Discretization with this stencil is guaranteed to be stable as long as the condition numbers of all diffusion tensors are less than or equal to 5.8

Theorem 3 (Existence of a Nonnegative Discretization)

Let $D \in \Re^{2\times 2}$ be symmetric positive definite with a spectral condition number k. Then there exists some $m(k) \in N$ such that $\mathrm{div}(D\nabla u)$ reveals a second-order nonnegative FD discretization on a $(2m+1)\times(2m+1)$ stencil. We refer the reader for the proof of this theorem to [72].

Weickert also defined the conditions for having a nonnegative semidiscretization on a (3×3)-stencil in the format of Table 5.2. He showed that for equal grid size in x and y directions we can achieve a nonnegative stencil of the following format if the spectral (2-norm) condition number satisfies:

$$\mathrm{cond}(D) \leq 3 + 2\sqrt{2} \cong 5.8284$$

5.2.4 Discrete Diffusion Process

So far, we have studied the semi-discrete diffusion processes which are discrete in space and continuous in time. Now, let us consider a fully discrete process (P_d) of the following format that is discrete both in space and time:

Let $f \in \Re^{\mathrm{N}}$ Calculate a sequence $(u^{(k)})_{k\in \mathrm{N}_0}$ of processed version of f by means of

$$\left.\begin{array}{rll} & u^{k+1} = Q(u^k)u^k, \quad \forall k \in N_0, & \\ & u^0 = f & \\ \text{where } Q \text{ has the following properties:} & & \\ \text{(D1) Continuity in its arguments:} & Q \in C(\Re^N, \Re^{N\times N}), & \\ \text{(D2) symmetry:} & q_{ij}(\nu) = q_{ji}(\nu) \quad \forall i,j \in J, \quad \forall \nu \in \Re^N, & \\ \text{(D3) unit row sum:} & \sum_{j\in J} q_{ij}(\nu) = 1 \quad \forall i \in J, \quad \forall \nu \in \Re^N, & \\ \text{(D4) nonnegativity:} & q_{ij}(\nu) \geq 0 \quad \forall i,j \in J \quad \forall \nu \in \Re^N, & \\ \text{(D5) positive diagonals:} & q_{ii}(\nu) > 0 \quad \forall i \in J, \quad \forall \nu \in \Re^N & \end{array}\right\} (P_d)$$

To define the relation between semi-discrete and discrete diffusion problems regarding wellposedness, we define u^k as an approximation of the solution u of (P_s) at time $t = k\tau$, where τ denotes the time step size. The following theorem shows the condition under which the discrete problem is well-posed and stable assuming its semi-discrete alternate is well-posed and stable.

Theorem 4 Let $\alpha \in [0,1]\,, \tau > 0$ and let $A = (a_{ij}) : \Re^N \to \Re^{(N\times N)}$ satisfy the requirements (S1)-(S5) of Section 5.2.3. Then the α-semi-implicit scheme

$$\frac{u^{k+1} - u^k}{\tau} = A(u^k)(\alpha u^{k+1} + (1-\alpha)u^k) \tag{5.16}$$

fulfils the prerequisites (D1)-(D6) for discrete diffusion models provided that $\alpha \in (0,1)$ and

$$\tau \leq \frac{1}{(1-\alpha)\max\limits_{i\in J} |a_{ii}(u^k)|} \tag{5.17}$$

If $\alpha = 0$ (explicit model), the properties (D1)-(D6) hold for

$$\tau < \frac{1}{\max\limits_{i\in J} |a_{ii}(u^k)|} \tag{5.18}$$

and the semi-implicit case $(\alpha = 1)$ satisfies (D1)-(D6) unconditionally. We refer the reader for proof to [72]. From this theorem, we conclude that in transition from semi-discrete to discrete case, the only additional condition which should be satisfied is equation 5.18 in the explicit case. No condition needs to be checked for the semi-implicit case.

5.3 Numerical Aspects of the Diffusion Model in 3D

So far, we have discussed the numerical aspects of 2D diffusion equations. However, we need to model the tumor growth in 3D and we need to extend the appropriate numerical method to 3D. The

discretization method introduced by Jbabdi [36] uses the chain rule to discretize the non-isotropic linear diffusion equation. However this method of discretization results in an unstable solution. We instead use the discretization method introduced by Weickert [72] and extend it to 3D. This method discretizes the mixed term derivatives a robust and stable way. We evaluate the stability issues of these models on synthetic and real data in Section 6.2.

5.3.1 Chain Rule Discretization

The first method we used for differentiation of the tumor growth diffusion equation was introduced by Jbabdi in [36]. This model seems plausible in the first glance as it uses the chain rule to discretize the anisotropic nonlinear diffusion equation. But experiments with an implementation of this model show that it easily gets unstable when the gradient of tensor parameters is nonzero. This model violates the nonnegativity of the discretization and hence it violates maximum-minimum principle and therefore easily gets unstable. Here, we show for the 2D case how it violates the nonnegativity. Consider the right hand side of the diffusion equation:

$$\operatorname{div}(D\nabla U) = \operatorname{div}\left(\begin{bmatrix} a & b \\ b & c \end{bmatrix}\begin{bmatrix} \frac{\partial u}{\partial x} \\ \frac{\partial u}{\partial y} \end{bmatrix}\right) \tag{5.19}$$

In order to discretize 5.19, if we apply the chain rule to calculate the derivitives

$$\partial\left(a\frac{\partial u}{\partial x}\right) = \frac{\partial a}{\partial x}\frac{\partial u}{\partial x} + a\frac{\partial^2 u}{\partial x^2}$$

and use the following discrete schemes to discretize the derivatives:

$$\begin{array}{l} \frac{\partial u}{\partial x} = \frac{u_{i+1,j} - ui,j}{2h_1} \\ \frac{\partial^2 u}{\partial x^2} = \frac{u_{i+1,j} - 2ui,j + u_{i,j+1}}{h_1^2} \end{array} \tag{5.20}$$

We will end up in a stencil with the format of Table 5.3. As we see in Table 5.3, this stencil can violate the nonnegativity for all its elements, even the ones containing only a and c coefficients. The same problem exists for the 3D case as well. Therefore, we cannot use this model for a stable discretization.

5.3.2 Extending Weickert Standard Model to 3D

The diffusion equation in 3D has the following format

$$\begin{array}{l} \operatorname{div}(D\nabla U) = \operatorname{div}\left(\begin{bmatrix} a & b & c \\ b & d & e \\ c & e & f \end{bmatrix}\begin{bmatrix} \frac{\partial u}{\partial x} \\ \frac{\partial u}{\partial y} \\ \frac{\partial u}{\partial z} \end{bmatrix}\right) = \\ \frac{\partial(a\frac{\partial u}{\partial x})}{\partial x} + \frac{\partial(b\frac{\partial u}{\partial y})}{\partial x} + \frac{\partial(c\frac{\partial u}{\partial z})}{\partial x} \\ + \frac{\partial(b\frac{\partial u}{\partial x})}{\partial y} + \frac{\partial(d\frac{\partial u}{\partial y})}{\partial y} + \frac{\partial(e\frac{\partial u}{\partial z})}{\partial y} \\ + \frac{\partial(c\frac{\partial u}{\partial x})}{\partial z} + \frac{\partial(e\frac{\partial u}{\partial y})}{\partial z} + \frac{\partial(f\frac{\partial u}{\partial z})}{\partial z} \end{array} \tag{5.21}$$

To solve this equation, we first implemented the finite difference method introduced in [36] but as we discussed before, it easily becomes unstable. Then we extended Wickert's standard model to 3D.

$\frac{-b_{i,j}}{2h_1h_2}$	$\frac{b_{i+1,j}-b_{i-1,j}}{4h_1h_2}$ $+\frac{c_{i,j+1}-c_{i,j-1}}{4h_2^2}+\frac{c_{i,j}}{h_2^2}$	$\frac{b_{i,j}}{2h_1h_2}$
$\frac{a_{i,j}}{h_1^2}-\frac{a_{i+1,j}-a_{i-1,j}}{4h_1^2}$ $-\frac{b_{i,j+1}-b_{i,j-1}}{4h_1h_2}$	$-\frac{2a_{i,j}}{h_1^2}-\frac{2c_{i,j}}{h_2^2}$	$\frac{a_{i,j}}{h_1^2}+\frac{a_{i+1,j}-a_{i-1,j}}{4h_1^2}$ $+\frac{b_{i,j+1}-b_{i,j-1}}{4h_1h_2}$
$\frac{b_{i,j}}{2h_1h_2}$	$-\frac{b_{i+1,j}-b_{i-1,j}}{4h_1h_2}$ $-\frac{c_{i,j+1}-c_{i,j-1}}{4h_2^2}+\frac{c_{i,j}}{h_2^2}$	$\frac{-b_{i,j}}{2h_1h_2}$

Table 5.3: Chain-Rule 2D stencil; This stencil is obtained with applying Chain-Rule discretization method introduced by Jbabdi [36]. Discretization with this stencil is not guaranteed to be stable since all stencil elements can get negative

The sample discretization for mixed and non-mixed terms is obtained by:

$$\begin{aligned}\frac{\partial(a\frac{\partial u}{\partial x})}{\partial x} &= \frac{1}{h_1}\left(\frac{a_{i+1,j,k}+a_{i,j,k}}{2}\frac{u_{i+1,j,k}-u_{i,j,k}}{h_1}-\frac{a_{i,j,k}+a_{i-1,j,k}}{2}\frac{u_{i,j,k}-u_{i-1,j,k}}{h_1}\right)\\ \frac{\partial(b\frac{\partial u}{\partial y})}{\partial x} &= \frac{1}{2h_1}\left(b_{i+1,j,k}\frac{u_{i+1,j+1,k}-u_{i+1,j-1,k}}{2h_2}-b_{i-1,j,k}\frac{u_{i-1,j+1,k}-u_{i-1,j-1,k}}{2h_2}\right)\end{aligned} \tag{5.22}$$

Replacing the discretization in the differential equation Figure 5.21 will result in the $3\times3\times3$ stencil of Table 5.4 . Although this model is simple and easy to implement, it is not always stable. Positive semi-definiteness of the tensor D guarantees that diagonal elements of the tensor (a, d and f) are nonnegative. However, we do not know the sign of off-diagonal elements of D, which in turn can make the diagonal elements of the stencil in figure 5.4 negative. Hence, we extended Weickert's nonnegative model to 3D.

5.3.3 Extending Weickert Nonnegative Model to 3D

In this section, we extend Weickert's theorem 5.2.3 on existence of a nonnegative discretization method for anisotropic diffusion equations to 3D. However, Weickert's theorem is proved for the general $(2m+1)\times(2m+1)$-stencil size. Extending the same theorem in the general format is not straight forward (if at all possible) and it is not our major concern in this thesis. What we intend to do in this thesis is finding a simple stable finite difference method to solve the diffusion equation. Therefore, we will focus on finding the weights of a $3\times3\times3$-stencil which can give us a nonnegative discretization and also the assigned conditionings which are explained in the following section.

k-1

j+1		$\frac{-e_{i,j,k-1}-e_{i,j+1,k}}{4h_2h_3}$	
j	$\frac{c_{i-1,j,k}+c_{i,j,k-1}}{4h_1h_3}$	$\frac{f_{i,j,k}+f_{i,j,k-1}}{2h_3^2}$	$\frac{-c_{i+1,j,k}-c_{i,j,k-1}}{4h_1h_3}$
j-1		$\frac{e_{i,j-1,k}+e_{i,j,k-1}}{4h_2h_3}$	
	i-1	i	i+1

k

j+1	$\frac{-b_{i,j+1,k}-b_{i-1,j,k}}{4h_1h_2}$	$\frac{d_{i,j+1,k}+d_{i,j,k}}{2h_2^2}$	$\frac{b_{i+1,j,k}+b_{i,j+1,k}}{4h_1h_2}$
j	$\frac{a_{i-1,j,k}+a_{i,j,k}}{2h_1^2}$	$-\frac{a_{i-1,j,k}+2a_{i,j,k}+a_{i+1,j,k}}{2h_1^2}$ $-\frac{d_{i,j-1,k}+2d_{i,j,k}+d_{i,j+1,k}}{2h_2^2}$ $-\frac{f_{i,j,k-1}+2f_{i,j,k}+f_{i,j,k+1}}{2h_3^2}$	$\frac{a_{i+1,j,k}+a_{i,j,k}}{2h_1^2}$
j-1	$\frac{b_{i-1,j,k}+b_{i,j-1,k}}{4h_1h_2}$	$\frac{d_{i,j-1,k}+d_{i,j,k}}{2h_2^2}$	$\frac{-b_{i+1,j,k}-b_{i,j-1,k}}{4h_1h_2}$
	i-1	i	i+1

k+1

j+1		$\frac{e_{i,j+1,k}+e_{i,j,k+1}}{4h_2h_3}$	
j	$\frac{-c_{i,j,k+1}-c_{i-1,j,k}}{4h_1h_3}$	$\frac{f_{i,j,k}+f_{i,j,k+1}}{2h_3^2}$	$\frac{c_{i+1,j,k}+c_{i,j,k+1}}{4h_1h_3}$
j-1		$\frac{-e_{i,j,k+1}-e_{i,j-1,k}}{4h_2h_3}$	
	i-1	i	i+1

Table 5.4: 3D Standard Stencil; This stencil is obtained by extending Weickert's 2D standard stencil to 3D. The boundary diagonal elements of the stencil can become negative which will result in an unstable discretization.

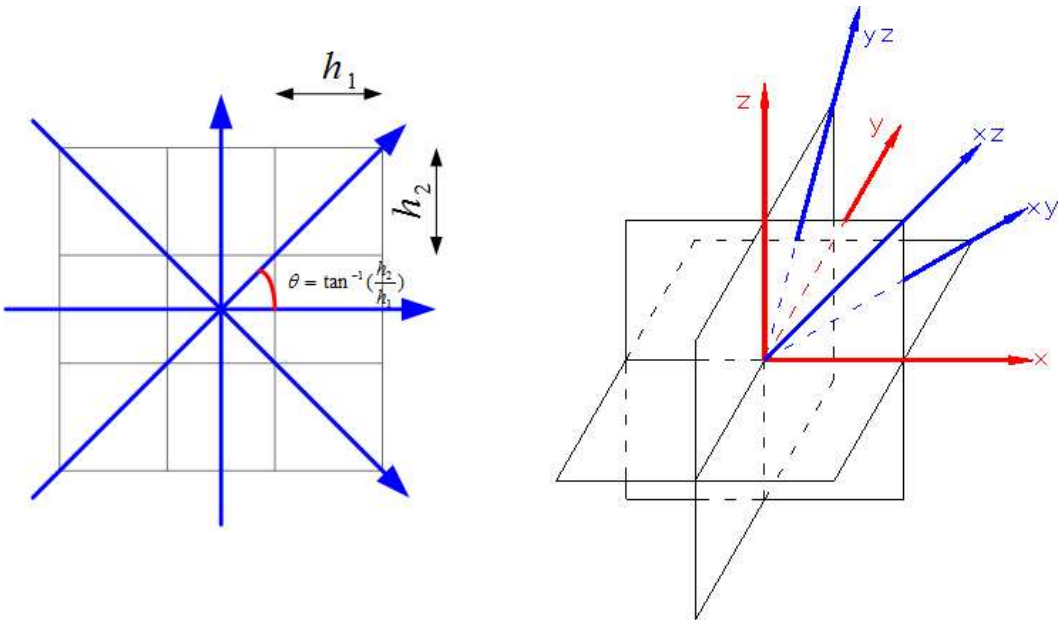

Figure 5.1: 2D and 3D Stencil. Left: 2D stencil with the four principal directions. Right: Three main planes of the 3D stencil with the six principal orientations

3D Nonnegative Discretization

In Weickert's standard method, the discretization of the mixed term derivatives as defined in equation 5.15 produces negatives terms in the stencil. This problem was described in details in Section 5.2.3. To solve this problem, Weickert suggested calculating the derivatives in some newly defined directions in addition to the three original directions (x,y,z). In 2D, the new directions are the diagonal directions of the 3×3-stencil. The mixed term derivatives in equation 5.13 are therefore replaced by directional derivatives and it is enough to find nonnegative weights for the new directions.

For 3D extension, we consider the 3D stencil as a combination of three 2D stencils in xy, yz and xz planes. In each plane, we have a 3×3 stencil. The "boundary pixels" of this stencil define four principal orientations $\beta_i \in (-\frac{\pi}{2}, \frac{\pi}{2}]$ corresponding to angles $\left(-\arctan\left(\frac{h_2}{h_1}\right),\ 0,\ \arctan\left(\frac{h_2}{h_1}\right),\ \frac{\pi}{2}\right)$. Figure 5.1-left shows a 3×3-stencil with the principal directions. We can define a partion of $(-\frac{\pi}{2}, \frac{\pi}{2}]$ into two subintervals:

$$(-\frac{\pi}{2}, \frac{\pi}{2}] = (-\frac{\pi}{2}, 0] \cup (0, \frac{\pi}{2}] = I_1 \cup I_{-1}$$

In the 3D coordinate system, each orientation is shown with three angles θ_x, θ_y and θ_z which define the angles to the three coordinate axes x, y and z. The directional splitting of the diffusion equation in 3D results in:

$$\begin{aligned}
&\mathrm{div}(D\nabla u) = \\
&\partial e_{\beta_x}(\alpha_x e_{\beta_x} u) + \partial e_{\beta_y}(\alpha_y e_{\beta_y} u) + \partial e_{\beta_z}(\alpha_z e_{\beta_z} u) + \\
&\partial e_{\beta_{xy}}(\alpha_{xy} e_{\beta_{xy}} u) + \partial e_{\beta_{-xy}}(\alpha_{-xy} e_{\beta_{-xy}} u) + \\
&\partial e_{\beta_{xz}}(\alpha_{xz} e_{\beta_{xz}} u) + \partial e_{\beta_{-xz}}(\alpha_{-xz} e_{\beta_{-xz}} u) + \\
&\partial e_{\beta_{yz}}(\alpha_{yz} e_{\beta_{yz}} u) + \partial e_{\beta_{-yz}}(\alpha_{-yz} e_{\beta_{-yz}} u) +
\end{aligned} \tag{5.23}$$

In equation 5.23, e_{β_i} denotes the stencil direction and α_i shows the coefficient along the corresponding direction. A nonnegative discrete method is obtained if α_i coefficients are nonnegative. In the rest of this section, we will find conditions under which directional coefficients remain nonnegative. First, for simplicity and also in order to use subsequent indices, let us define

$$\begin{array}{l}\phi_0 := \beta_x, \phi_1 := \beta_y, \phi_2 := \beta_z, \phi_3 := \beta_{xy}, \phi_4 := \beta_{xz}, \phi_5 := \beta_{yz}. \\ \gamma_0 := \alpha_x, \gamma_1 := \alpha_y, \gamma_2 := \alpha_z, \gamma_3 := \alpha_{xy}, \gamma_4 := \alpha_{xz}, \gamma_5 := \alpha_{yz}\end{array} \tag{5.24}$$

In each plane, there is only one diagonal direction that has a positive coefficient and the other diagonal direction has a zero coefficient. For example, in xy plane, if α_{xy} is positive then α_{-xy} is zero and vise a versa. Hence, for simplicity, we can keep only one diagonal direction in each plane and we will keep the one in I_1 partition (between $(0, \frac{\pi}{2}]$). When the coefficient for one diagonal direction is defined, it will be easy to find the other one from it. Figure 5.1-right shows the three planes of a $3 \times 3 \times 3$-stencil with the defined six principal directions.

By substituting new coefficients of equation 5.24 in equation 5.23, we will have

$$\begin{array}{l} div(D\nabla U) = div\left(\left(\begin{array}{ccc} a & b & c \\ b & d & e \\ c & e & f \end{array}\right)\nabla u\right) = \sum_{i=0}^{5} \frac{\partial}{\partial e_{\phi_i}}(\gamma_i \frac{\partial}{\partial e_{\phi_i}}) = \\ \frac{\partial}{\partial x}\sum_{i=0}^{5} \cos\phi_{ix}(\gamma_i(u_x\cos\phi_{ix} + u_y\cos\phi_{iy} + u_z\cos\phi_{iz})) \\ + \frac{\partial}{\partial y}\sum_{i=0}^{5} \cos\phi_{iy}(\gamma_i(u_x\cos\phi_{ix} + u_y\cos\phi_{iy} + u_z\cos\phi_{iz})) \\ + \frac{\partial}{\partial z}\sum_{i=0}^{5} \cos\phi_{iz}(\gamma_i(u_x\cos\phi_{ix} + u_y\cos\phi_{iy} + u_z\cos\phi_{iz})) \\ = div\left(\left(\begin{array}{ccc} \sum_{i=0}^{5}\gamma_i\cos^2\phi_{ix} & \sum_{i=0}^{5}\gamma_i\cos\phi_{ix}\cos\phi_{iy} & \sum_{i=0}^{5}\gamma_i\cos\phi_{ix}\cos\phi_{iz} \\ \sum_{i=0}^{5}\gamma_i\cos\phi_{iy}\cos\phi_{ix} & \sum_{i=0}^{5}\gamma_i\cos^2\phi_{iy} & \sum_{i=0}^{5}\gamma_i\cos\phi_{iy}\cos\phi_{iz} \\ \sum_{i=0}^{5}\gamma_i\cos\phi_{ix}\cos\phi_{iz} & \sum_{i=0}^{5}\gamma_i\cos\phi_{iy}\cos\phi_{iz} & \sum_{i=0}^{5}\gamma_i\cos^2\phi_{iz} \end{array}\right)\nabla u\right) \end{array} \tag{5.25}$$

By comparing the coefficients and using the definition of γ_i we obtain the linear system:

$$\left(\begin{array}{cccccc} 1 & 0 & 0 & \cos^2\phi_{3x} & \cos^2\phi_{3y} & 0 \\ 0 & 0 & 0 & \cos\phi_{3x}\cos\phi_{3y} & 0 & 0 \\ 0 & 0 & 0 & 0 & \cos\phi_{4x}\cos\phi_{4z} & 0 \\ 0 & 1 & 0 & \cos^2\phi_{3y} & 0 & \cos^2\phi_{5y} \\ 0 & 0 & 0 & 0 & 0 & \cos\phi_{5y}\cos\phi_{5z} \\ 0 & 0 & 1 & 0 & \cos^2\phi_{4z} & \cos^2\phi_{5z} \end{array}\right)\left(\begin{array}{c}\gamma_0\\ \gamma_1\\ \gamma_2\\ \gamma_3\\ \gamma_4\\ \gamma_5\end{array}\right) = \left(\begin{array}{c} a\\ b\\ c\\ d\\ e\\ f\end{array}\right) \tag{5.26}$$

that has the unique solution

$$\begin{array}{l} \gamma_0 = a - c\frac{\cos\phi_{4x}}{\cos\phi_{4z}} - b\frac{\cos\phi_{3x}}{\cos\phi_{3y}} \\ \gamma_1 = d - e\frac{\cos\phi_{5y}}{\cos\phi_{5z}} - b\frac{\cos\phi_{3y}}{\cos\phi_{3x}} \\ \gamma_2 = f - e\frac{\cos\phi_{5z}}{\cos\phi_{5y}} - c\frac{\cos\phi_{4z}}{\cos\phi_{4x}} \\ \gamma_3 = \frac{b}{\cos\phi_{3x}\cos\phi_{3y}} \\ \gamma_4 = \frac{c}{\cos\phi_{4x}\cos\phi_{4z}} \\ \gamma_5 = \frac{e}{\cos\phi_{5y}\cos\phi_{5z}} \end{array} \tag{5.27}$$

To have a nonnegative discretization, the coefficients γ_0 to γ_5 must be nonnegative. If the grid sizes are h_1, h_2 and h_3, the coefficients for all the nine directions are defined as:

$$\begin{aligned}
\gamma_x &= a - |c|\tfrac{h_1}{h_3} - |b|\tfrac{h_1}{h_2} \geq 0 \\
\gamma_y &= d - |e|\tfrac{h_2}{h_3} - |b|\tfrac{h_2}{h_1} \geq 0 \\
\gamma_z &= f - |e|\tfrac{h_3}{h_2} - |c|\tfrac{h_3}{h_1} \geq 0 \\
\gamma_{xy} &= (|b| + b).\tfrac{h_1^2+h_2^2}{h_1 h_2} \geq 0 \\
\gamma_{-xy} &= (|b| - b).\tfrac{h_1^2+h_2^2}{h_1 h_2} \geq 0 \\
\gamma_{xz} &= (|c| + c).\tfrac{h_1^2+h_3^2}{h_1 h_3} \geq 0 \\
\gamma_{-xz} &= (|c| - c).\tfrac{h_1^2+h_3^2}{h_1 h_3} \geq 0 \\
\gamma_{yz} &= (|e| + e).\tfrac{h_2^2+h_3^2}{h_2 h_3} \geq 0 \\
\gamma_{-yz} &= (|e| - e).\tfrac{h_2^2+h_3^2}{h_3 h_3} \geq 0
\end{aligned} \tag{5.28}$$

From equation 5.28 we can define the condition of the tensor for a nonnegative discretization:

$$\begin{aligned}
a &\geq |c|\tfrac{h_1}{h_3} + |b|\tfrac{h_1}{h_2} \\
d &\geq |e|\tfrac{h_2}{h_3} + |b|\tfrac{h_2}{h_1} \\
f &\geq |e|\tfrac{h_3}{h_2} + |c|\tfrac{h_3}{h_1}
\end{aligned} \tag{5.29}$$

Finally, we can find the nonnegative weights of the stencil by replacing the coefficients of equation 5.28 in equation 5.23 and by considering the directional step sizes (e.g. $\sqrt{h_1^2 + h_2^2}$ for the xy direction). The final stencil is given in Table 5.5. Using this stencil guarantees a stable spatial discretization assuming equation 5.29 is satisfied. The only other issue that we need to consider is the time stability which is dealt in the same way as the 2D case (equation 5.18).

5.4 Numerical Aspects of the Geodesic Model

In Chapter 4 we described the geodesic model to find distance function in time. The mathematical formulation ended in a Hamilton-Jacobi equation 4.27 of the form:

$$\phi_t + |\mathrm{grad}\phi| = 0 \tag{5.30}$$

We here explain the numerical aspects of solving this equation. Hamilton-Jacobi equations are first order hyperbolic (wave like) PDE of the form $\phi_t + H(\phi_x) = 0$. They are very similar to classical hyperbolic conservative laws [57]. The numerical aspects of first order hyperbolic equations are totally different from the second order parabolic equations that we studied in the previous section. There are two main issues about the first-order hyperbolic equations: 1. consistency and 2. Stability.

5.4.1 Consistency

Consistency is achieved by applying the discretization in the direction of the wave motion (it depends on the sign of velocity). Generally upwind methods approximate derivatives by biasing the finite difference stencil in the direction where the characteristic information is coming. Upwind method guarantees a consistent finite difference scheme. Here, we briefly explain the upwind method for a

k-1

j+1		$\frac{\lvert e_{i,j+1,k-1}\rvert - e_{i,j+1,k-1}}{4h_2h_3}$ $+\frac{\lvert e_{i,j,k}\rvert - e_{i,j,k}}{4h_2h_3}$	
j	$\frac{\lvert c_{i-1,j,k-1}\rvert + c_{i-1,j,k-1}}{4h_1h_3}$ $+\frac{\lvert c_{i,j,k}\rvert + c_{i,j,k}}{4h_1h_3}$	$\frac{f_{i,j,k-1}+f_{i,j,k}}{2h_3^2} - \frac{\lvert c_{i,j,k-1}\rvert + \lvert c_{i,j,k}\rvert}{2h_1h_3} - \frac{\lvert e_{i,j,k-1}\rvert + \lvert e_{i,j,k}\rvert}{2h_2h_3}$	$\frac{\lvert c_{i+1,j,k-1}\rvert - c_{i+1,j,k-1}}{4h_1h_3}$ $+\frac{\lvert c_{i,j,k}\rvert - c_{i,j,k}}{4h_1h_3}$
j-1		$\frac{\lvert e_{i,j-1,k-1}\rvert + e_{i,j-1,k-1}}{4h_2h_3}$ $+\frac{\lvert e_{i,j,k}\rvert + e_{i,j,k}}{4h_2h_3}$	
	i-1	i	i+1

k

j+1	$\frac{\lvert b_{i-1,j+1,k}\rvert - b_{i-1,j+1,k}}{4h_1h_2}$ $+\frac{\lvert b_{i,j,k}\rvert - b_{i,j,k}}{4h_1h_2}$	$\frac{d_{i,j+1,k}+d_{i,j,k}}{2h_2^2} - \frac{\lvert b_{i,j+1,k}\rvert + \lvert b_{i,j,k}\rvert}{2h_1h_2} - \frac{\lvert e_{i,j+1,k}\rvert + \lvert e_{i,j,k}\rvert}{2h_1h_3}$	$\frac{\lvert b_{i+1,j+1,k}\rvert + b_{i+1,j+1,k}}{4h_1h_2}$ $+\frac{\lvert b_{i,j,k}\rvert + b_{i,j,k}}{4h_1h_2}$
j	$\frac{a_{i-1,j,k}+a_{i,j,k}}{2h_1^2}$ $-\frac{\lvert b_{i-1,j,k}\rvert + \lvert b_{i,j,k}\rvert}{2h_1h_2}$ $-\frac{\lvert c_{i-1,j,k}\rvert + \lvert_{i,j,k}\rvert}{2h_1h_3}$	$-\frac{a_{i-1,j,k}+2a_{i,j,k}+a_{i+1,j,k}}{2h_1^2}$ $-\frac{d_{i,j-1,k}+2d_{i,j,k}+d_{i,j+1,k}}{2h_2^2}$ $-\frac{f_{i,j,k-1}+2f_{i,j,k}+f_{i,j,k+1}}{2h_3^2}$ $-\frac{\lvert b_{i-1,j+1,k}\rvert - b_{i-1,j+1,k} + \lvert b_{i+1,j+1,k}\rvert + b_{i+1,j+1,k}}{4h_1h_2}$ $-\frac{\lvert b_{i-1,j-1,k}\rvert + b_{i-1,j-1,k} + \lvert b_{i+1,j-1,k}\rvert - b_{i+1,j-1,k}}{4h_1h_2}$ $+\frac{\lvert b_{i-1,j,k}\rvert + \lvert b_{i+1,j,k}\rvert + \lvert b_{i,j-1,k}\rvert + \lvert b_{i,j+1,k}\rvert + 2\lvert b_{i,j,k}\rvert}{2h_1h_2}$ $-\frac{\lvert c_{i-1,j,k+1}\rvert - c_{i-1,j,k+1} + \lvert c_{i+1,j,k+1}\rvert + c_{i+1,j,k+1}}{4h_1h_3}$ $-\frac{\lvert c_{i-1,j,k-1}\rvert + c_{i-1,j,k-1} + \lvert c_{i+1,j,k-1}\rvert - c_{i+1,j,k-1}}{4h_1h_3}$ $+\frac{\lvert c_{i-1,j,k}\rvert + \lvert c_{i+1,j,k}\rvert + \lvert c_{i,j,k-1}\rvert + \lvert c_{i,j,k-1}\rvert + 2\lvert c_{i,j,k}\rvert}{2h_1h_3}$ $-\frac{\lvert e_{i,j-1,k+1}\rvert - e_{i,j-1,k+1} + \lvert e_{i,j+1,k+1}\rvert + e_{i,j+1,k+1}}{4h_2h_3}$ $-\frac{\lvert e_{i,j-1,k-1}\rvert + e_{i,j-1,k-1} + \lvert e_{i,j+1,k-1}\rvert - e_{i,j+1,k-1}}{4h_2h_3}$ $+\frac{\lvert e_{i,j-1,k}\rvert + \lvert e_{i,j+1,k}\rvert + \lvert e_{i,j,k-1}\rvert + \lvert e_{i,j,k+1}\rvert + 2\lvert e_{i,j,k}\rvert}{2h_2h_3}$	$\frac{a_{i+1,j,k}+a_{i,j,k}}{2h_1^2}$ $-\frac{\lvert b_{i+1,j,k}\rvert + \lvert b_{i,j,k}\rvert}{2h_1h_2}$ $-\frac{\lvert c_{i+1,j,k}\rvert + \lvert c_{i,j,k}\rvert}{2h_1h_3}$
j-1	$\frac{\lvert b_{i-1,j-1,k}\rvert + b_{i-1,j-1,k}}{4h_1h_2}$ $+\frac{\lvert b_{i,j,k}\rvert + b_{i,j,k}}{4h_1h_2}$	$\frac{d_{i,j-1,k}+d_{i,j,k}}{2h_2^2} - \frac{\lvert b_{i,j-1,k}\rvert + \lvert b_{i,j,k}\rvert}{2h_1h_2} - \frac{\lvert e_{i,j-1,k}\rvert + \lvert e_{i,j,k}\rvert}{2h_1h_3}$	$\frac{\lvert b_{i+1,j-1,k}\rvert - b_{i+1,j-1,k}}{4h_1h_2}$ $+\frac{\lvert b_{i,j,k}\rvert - b_{i,j,k}}{4h_1h_2}$
	i-1	i	i+1

k+1

j+1		$\frac{\lvert e_{i,j+1,k+1}\rvert + e_{i,j+1,k+1}}{4h_2h_3}$ $+\frac{\lvert e_{i,j,k}\rvert + e_{i,j,k}}{4h_2h_3}$	
j	$\frac{\lvert c_{i-1,j,k+1}\rvert - c_{i-1,j,k+1}}{4h_1h_3}$ $+\frac{\lvert c_{i,j,k}\rvert - c_{i,j,k}}{4h_1h_3}$	$\frac{f_{i,j,k+1}+f_{i,j,k}}{2h_3^2} - \frac{\lvert c_{i,j,k+1}\rvert + \lvert c_{i,j,k}\rvert}{2h_1h_3} - \frac{\lvert e_{i,j,k+1}\rvert + \lvert e_{i,j,k}\rvert}{2h_2h_3}$	$\frac{\lvert c_{i+1,j,k+1}\rvert + c_{i+1,j,k+1}}{4h_1h_3}$ $+\frac{\lvert c_{i,j,k}\rvert + c_{i,j,k}}{4h_1h_3}$
j-1		$\frac{\lvert e_{i,j-1,k+1}\rvert - e_{i,j-1,k+1}}{4h_2h_3}$ $+\frac{\lvert e_{i,j,k}\rvert - e_{i,j,k}}{4h_2h_3}$	
	i-1	i	i+1

Table 5.5: 3D Non-negative Stencil; This stencil is obtained by extending Weickert's 2D non-negative stencil to 3D. The stencil elements are non-negative as long as conditions of Equation 5.29 are satisfied, which results in a stable discretization.

basic linear hyperbolic equation

$$\phi_t + \vec{V}.\nabla\phi = 0 \tag{5.31}$$

where $\vec{V}.\nabla\phi = u\phi_x + v\phi_y + w\phi_z$. The time discretization using first order forward Euler gives:

$$\frac{\phi^{n+1} - \phi^n}{\Delta t} + u^n\phi_x + v^n\phi_y + w^n\phi_z = 0 \tag{5.32}$$

For simplicity, we consider the one-dimensional version of the equation

$$\frac{\phi^{n+1} - \phi^n}{\Delta t} + u^n\phi_x = 0 \tag{5.33}$$

where the sign of u^n indicates whether the values of ϕ are either moving to the right or to the left. Considering that u^n is spatially varying, we rewrite the equation 5.33 as

$$\frac{(\phi_x)_i^{n+1} - (\phi_x)_i^n}{\Delta t} + u_i^n(\phi_x)_i^n = 0 \tag{5.34}$$

where $(\phi_x)_i$ shows the derivative of ϕ at the grid point x_i. If $u_i > 0$ then the values of ϕ are moving from left to right and based on the *method of characteristics,* we should look at the left of x_i to find the value of $(\phi_x)_i$ at the end of time step. Similarly, we should search the right of x_i when $u_i < 0$. Clearly backward differences D_ϕ^- should be used to approximate ϕ_x when $u_i > 0$ and forward differences D_ϕ^+ for the case $u_i < 0$. Euler Forward and backward differences are calculated as

$$D_x^+\phi_x \approx \frac{\phi_{i+1} - \phi_i}{\Delta x},$$
$$D_x^-\phi_x \approx \frac{\phi_i - \phi_{i-1}}{\Delta x},$$

This idea of choosing the differencing method based on the sign of u is known as *upwind* differencing [57]. The combination of the Euler differencing method with the upwind difference scheme gives a *consistent* finite difference scheme to the differential equation 5.31.

So far, we explained the upwind method for a simple linear equation. However equation 5.30 is a non-linear equation of the general form $f(u) = u^2$. Engquist-Osher introduced the upwind method for nonlinear functions [21]. The numerical flux to the positive speed function f is defined as:

$$f(u) = \Big(\big(\max(D_x^-u, 0)\big)^2 + \big(\min(D_x^+u, 0)\big)^2\Big) \quad , u = \phi_x \tag{5.35}$$

Consistency of this discretization scheme is proved in [21]. This method is extended to the 3D in [44] for the quadratic Hamilton equation as defined in equation 4.30.

5.4.2 Stability

As we discussed in the beginning of this chapter, a numerical method is said to be stable if small perturbations do not cause the resulting numerical solution to diverge without bound [30]. According to [57], stability guaranties that small errors are not amplified in time. For a first order hyperbolic equation, stability is achieved by forcing Courant-Friedrichs-Lewy conditions (CLF condition), which states that numerical waves should propagate at least as fast as the physical wave. This

means that the speed of the numerical wave $\frac{\Delta x}{\Delta t}$ must be at least as large as the physical wave speed $|u|$. The CLF condition for 5.31 is given as [57]:

$$\Delta t \ \leq \ \frac{\delta x}{\max\{|u|\}} \tag{5.36}$$

where $\max\{|u|\}$ is the largest value of $|u|$ over the entire Cartesian grid. equation 5.36 is enforced by choosing a CLF number (α) with

$$\Delta t \left(\frac{\max\{|u|\}}{\Delta x} \right) = \alpha \tag{5.37}$$

where $0 \ \leq \alpha \leq \ 1$. According to [57] a common near-optimal choice is $\alpha = 0.9$ but a common conservative choice is $\alpha = 0.5$. The multidimensional CLF condition for equation 5.31 can be written as

$$\Delta t \left(\frac{\max\left\{|\vec{V}|\right\}}{\min \Delta x, \Delta y, \Delta z} \right) = \alpha \tag{5.38}$$

The CLF condition for the Hamilton-Jacobi equation $\phi_t + H(\phi_x) = 0$ is given in [57] as

$$\Delta t \left(\frac{|H_1|}{\Delta x} + \frac{|H_2|}{\Delta y} + \frac{|H_3|}{\Delta z} \right) < 1 \tag{5.39}$$

where H_1, H_2 and H_3 are the spatial derivatives of H with respect to ϕ_x, ϕ_y and ϕ_z, respectively. Using this scheme, it is easy to find the CLF condition for Geodesic distance Hamilton-Jacobi equation with nonlinear part

$$H(\phi) = |\mathrm{grad}\phi|^2 = \sum_{k=1}^{3} \sum_{l=1}^{3} \frac{\partial \phi}{\partial x_l} \frac{\partial \phi}{\partial x_k} g^{kl} \tag{5.40}$$

where g^{kl} are the elements of the diffusion tensor. It is easy to see that

$$H_1 = \frac{\partial \phi}{\partial x_1} g^{11} + \frac{\partial \phi}{\partial x_2} g^{12} + \frac{\partial \phi}{\partial x_3} g^{13}$$

H_2 and H_3 are computed in the same way. We conclude that in contrast to second order Parabolic equations, Hamilton-Jacobi equation is stable in space and its time stability is simply satisfied by choosing an appropriate time step.

5.5 Summary

In this chapter, we discussed the numerical aspects for solving differential equations of the two different tumor growth models we introduced in Chapter 4. One of the growth models is the Geodesic distance model that ends in a Hamilton-Jacobi differential equation. The Hamilton-Jacobi equation belongs to the family of first order hyperbolic equations, where numerical aspects, including stability and consistency have been well studied in the literature. Using a suitable upwind method and an appropriate time step guarantees the consistency and stability of this model.

On the other hand, diffusion equation belongs to the family of second order parabolic equations. Certain conditions should be satisfied to guarantee the spatial stability of these equations. These

conditions are defined for the 2D case in [72]. In this chapter, we extended Weickert's discretization model to 3D to solve this equation and defined the corresponding stability conditions. The conditions show that unless the tensors have particular properties, the model gets unstable. So in comparison, the Geodesic model can be applied for more cases and not just for tensors with particular shapes.

Chapter 6

Experiments

6.1 Introduction

In this chapter, we will evaluate the materials and methods discussed in Sections 4 and 5. First, we validate the stability of numerical methods given in Section 5 for solving the second-order parabolic partial differential equation that is the main equation of the anisotropic diffusive model. For this mean, we generate a variety of synthetic 2D and 3D test models. Some models become unstable even on simple models and some become unstable only in complicated cases. The examples are ordered from easy to difficult to test where each model gets unstable. These test cases plus the degree of stability of each proposed model are explained in detail in Section 6.2. The second part of the chapter describes a system for validating the geodesic and diffusive models given in Section 4 on real patient DTI data. The validation procedure includes some pre-processing steps such as segmentation, registration and tensor extraction followed by the main simulation process. The results of simulation are then compared visually and numerically with ground truth (patient data). We have explained each of these steps in details in this chapter.

6.2 Experiments on Stability

In this section, we evaluate the discretization methods introduced in Chapter 5 for solving the PDE equation of diffusive growth model. We first test the correctness of the introduced methods on synthetic test cases and then apply the models to the real DTI data of patients. Finally, we provide visual examples of both stable and unstable cases.

6.2.1 Test on Synthetic Data

In this section, we will compare the stability issues of three different discretization methods for solving the second order parabolic PDE of the anisotropic diffusive model. These models include Jbabdi's chain-rule discretization (Section 5.3.1) Weickert's standard model (Section 5.3.3) and Wickert's nonnegative model (Section 5.3.2). For simplicity, we name these models JB, WS and WN respectively. As we mentioned in Chapter 5, the only method that is stable is WN method.

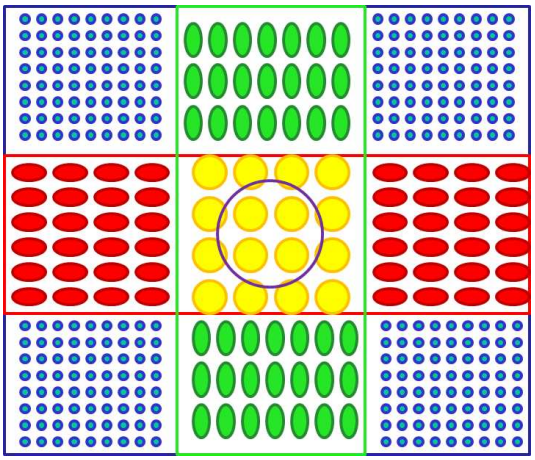

Figure 6.1: Tensor template for a 2D sample synthetic model. The simulation starts from the circle in the middle that is the symbol of tumor at initial time. Tensor shapes show the size and the degree of isotropy in different locations

Even this method is only stable when the condition number of all diffusion tensors is less than 5.8. To clarify the definition of instability, we notice that the measured value is the normalized tumor cell density that should always be between zero and one. The strict max-min stability condition states that the normalized tumor cell density should be between 0 and 1 in all iterations. A less strict stability condition is to check only the maximum stability.

To test the degree of stability of each method, we made several 2D examples with different degrees of complexity. The first example is a 64×64 image with a circle in the middle corresponding to tumor at initial time as shown in figure 6.1. The image value inside the circle is 1 (corresponding to normalized tumor cell density) and outside that is 0. The image values inside the circle remain 1 in all iterations representing the boundary condition. If the proliferation rate is more than zero, we consider a growing tumor boundary meaning that once the tumor cell density of a voxel reaches the value 1, the voxel will be added to the boundary in subsequent iterations. We also need to make a diffusion tensor image corresponding to this image. The size and shape of the tensors are symbolically shown in figure 6.1. Diffusion tensor image includes a ribbon of tensors with the anisotropy parallel to x direction and another ribbon of tensors in the y direction. The tensors in the middle are the summation of both ribbons and are isotropic. The rest of the image is covered with very small isotropic tensors. The 2D diffusion tensor has the format:

$$\mathrm{D} = \begin{pmatrix} a & b \\ b & c \end{pmatrix} \tag{6.1}$$

In choosing the values of the tensors we should always notice that tensors should be symmetric positive definite. The simplest case is where $b = 0$ for all tensors and the condition number of tensors are less than 5.8. Even for this simple model, the chain rule discretization model (JB model) always simply becomes unstable. This instability starts where the gradient of tensor elements becomes nonzero, e.g. on the edges of the two ribbons. The two other methods are stable in this example. WN

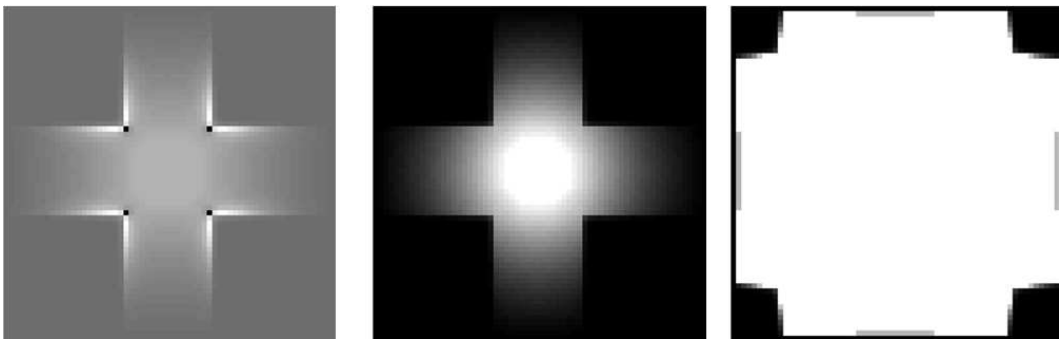

Figure 6.2: The result of applying numerical methods on the first test case. Left: Chain rule (Jbabdi) model, the white and black pixels on the edges of the ribbon correspond respectively to the pixels with very high and very low intensities that destroy the max-min stability. The initial tumor area region with intensity 1 (the circle in the middle) looks grey compared to edge pixels. Middle: Weickert's nonnegative method, this stable example nicely shows the diffusive nature of the growth. Right: Weickert model with nonzero proliferation rate. The proliferation helps the tumor cells to grow even in parts of the image with very small tensors.

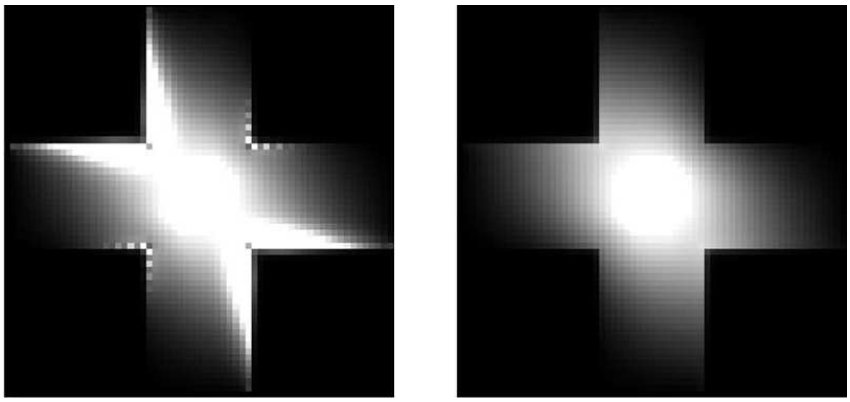

Figure 6.3: The result of applying numerical methods on the first test case but with non-zero b values. Left: Chain rule model that becomes unstable. Right: Weickert model that remains stable.

model is stable since condition numbers of all tensors are less than 5.8 and WS model is stable since the b values are zero and the stencils remain positive. Figure 6.2 illustrates the result of applying JB and WS models on this simple model. The left image shows the result of JB model. The white and black pixels on the edges of the ribbon correspond respectively to the pixels with very high and very low intensities so that the initial tumor circle area (with intensity 1) and the background pixels (with intensity 0) are shown grey with respect to them. This means that the edge pixel values are not in the 0-1 band and the stability is ruined. The middle image shows the result of applying WN method. The diffusive nature of the growth is clearly seen in this stable model. The right image shows the result of using Weickert's model on a diffusion equation with nonzero proliferation rate. As seen in the image, the proliferation helps the tumor cells to grow even in parts of the image with very small tensors shown in Figure 6.1.

We made this synthetic model a little more complicated by using non-zero b values. We tested two

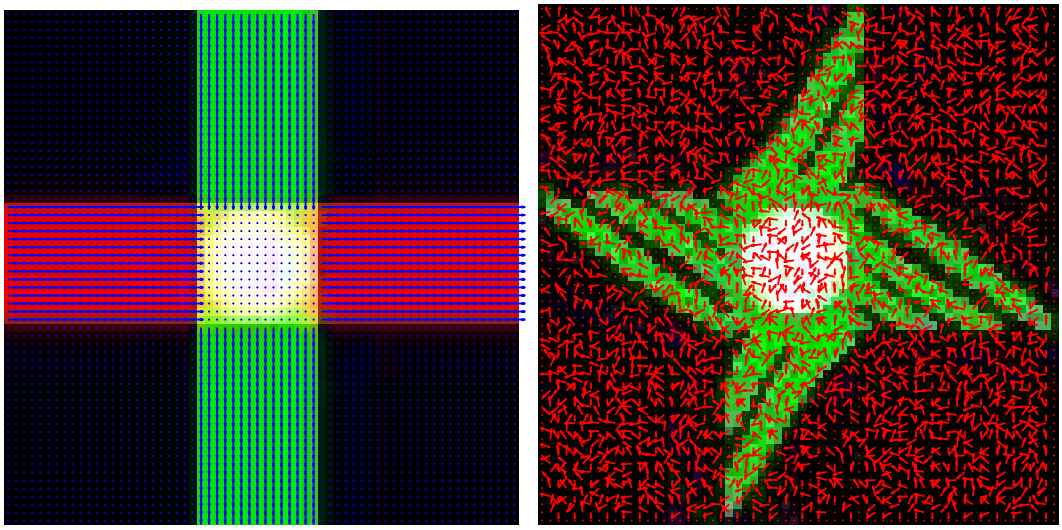

Figure 6.4: Synthetic test templates with first eigenvectors of corresponding diffusion tensors plotted on them; Left: a simple model with two ribbons of anisotropic tensors in x and y directions and small isotropic tensors in the rest of the image. This model can only make JB model unstable. Right: A complicated test model where tensors in the green area are larger than the rest of the image which produces a high gradient field in tensor values. Also directions of tensors are completely random as red arrows show. JB and both Weickert's models are even maximally unstable on this test model

different scenarios, once with $cond(D) \leq 5.8$ for all tensors and the other with some tensor values $cond(D) > 5.8$. We expected that in the first scenario, Weickert's non-negative model remains stable while Weickert's standard model becomes unstable and both models become unstable in the second case. In practice, this was true for the strict max-min stability condition. But we observed that the maximum stability condition was satisfied for all cases. The minimum values decreased a bit below zero, however their values were bounded. So, we could keep the maximum stability and a bounded minimum stability for these simple normal cases. Figure 6.3 shows an example of this case. The nonzero b values result in inclined tensors. Again the JB model becomess unstable and WN model remains stable (left and right images).

Then we tried to find an example where the maximum stability was also ruined with Weickert's models. It was not an easy task since Weickert's methods were maximally stable on all regular models. Finally, by using a complicated model with random tensor distribution on a high gradient irregular shape (instead of rectangular ribbons), we could achieve instability in Weickert's methods with $cond(D) > 5.8$. Figure 6.4 shows the two test models. The left image shows the previous test model with regular tensors in x and y directions. The first eigenvector of the tensors are plotted on the image. The right image shows the new case that is unstable with all of the three models. The directions of tensors are chosen randomly. Moreover, the size of tensors in the green area is much bigger than the rest of the image, which introduces an additional gradient in the tensor values.

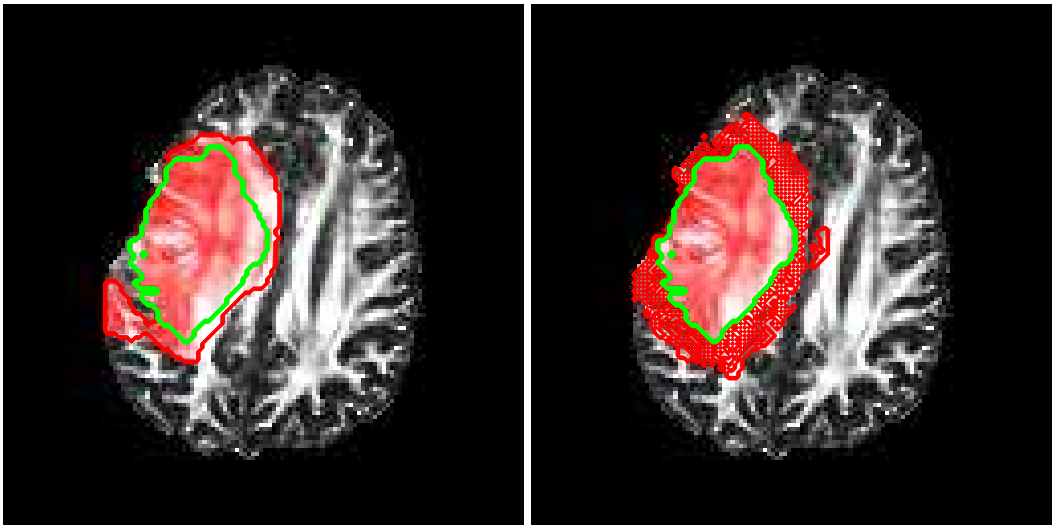

a b

Figure 6.5: Test of anisotropic diffusive model on real DTI data of patients with glioma. Left: Result of applying WN discretization method. The homogenous red area shows a stable growth model. Right: Result of applying JB model, dotted red areas show the inhomogeneous growth caused by an unstable model.

6.2.2 Test on Real Data

We extended all three mentioned discretization models to 3D to test them on real patient data. First, we used the original DTI data extracted with ExploreDTI software [25], from diffusion weighted images. The Chain-rule model becomes unstable very soon. WS and WN methods remain stable for our datasets if we just consider max stabilityk, not max-min stability. In the next step, we applied Jbabdi's post processing method on tensors, as explained in Section 4.3, to increase the degree of anisotropy of tensors. With a value of r equal to 10, meaning that the tensors get 10 times longer in the direction of first eigen-value, all methods become unstable. Figure 6.5-a shows a sample of WN method that remains stable through the simulation process. The tumor starts its growth from the green margin and keeps growing to a certain volume. The growth area remains homogenous. The right image shows the result of applying JB method to the same data. The instability results in a non-homogenous area that is seen as dotted red areas in the image. We conclude that, if we only take into account the max stability and not the max-min stability, Weickert's methods remain stable on real data without post processing. But a post processing that increases the degree of anisotropy will consequently increase the tensor condition number and destroy the stability. So WS model is stable for almost all regular models (even real patient DTI data), but the stability cannot be guaranteed and JB model is always unstable.

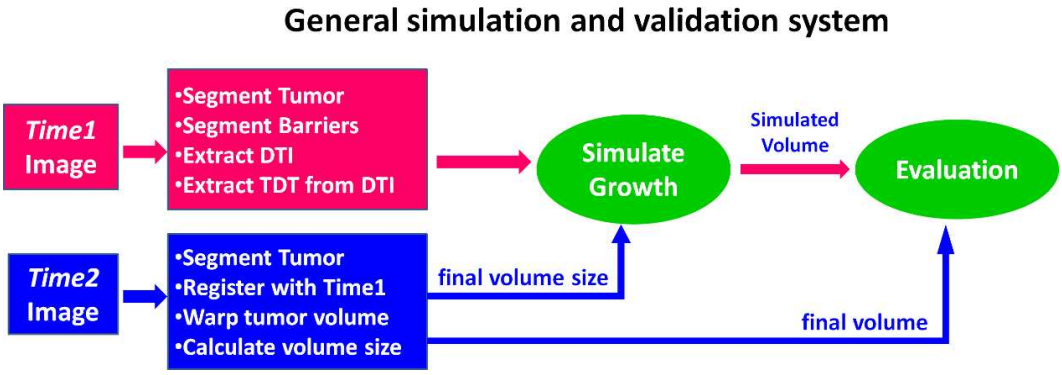

Figure 6.6: Overview of the tumor growth validation system

6.3 Experiments on Tumor Growth

In this section, we show the complete system of validation of growth models using real DTI data. First, we apply several steps of pre-processing to the raw DWI data to extract the necessary information for the simulation process. In the simulation process, the non-isotropic diffusion model and the geodesic distance model are separately tested on the data. To compare these models with the Euclidean distance model used in current therapy, the isotropic diffusion model is also tested on the data. The results are numerically and visually compared with the actual tumor growth at subsequent times.

6.3.1 Patients and Data

We used MRI and DTI data from clinical scans of patients with GBM.[1] The data acquisition process is done in cross cancer institute at the university of Alberta [15]. So far, data of 69 patients with different types of brain tumor have been collected, 56 having different types of high-grade tumours (27 cases of grade IV Glioblastoma multiforme; 18 cases of grade III-IV astrocytoma; 6 cases of grade III-IV oligodendroglioma; 5 cases of mixed high-grade glioma) and 13 having low-grade tumours (9 cases of grade II oligodendroglioma; 2 cases of grade II of oligodendroglioma, 2 cases of mixed low-grade glioma). All patients undergo routine clinical MRI scans at regular intervals of 3 months for high-grades glioma or 6 months for low-grades glioma. Patients are offered one pre-radiation treatment and 2 post-treatment DTI scans (at 1 and 7 months). To minimize the effects of radiation treatment not considered in our mathematical model, we only use data from the first available post-treatment DWI scan. Even though the average mortality is less than one year, with less than half of the patients yielding serial images, we have already acquired about 38 post-treatment DTI scans that can be used in combination with later regular MRI scans for validating the proposed mathematical tumour growth model.

[1] The data collection protocol was approved by REB and the patients have provided an informed consent.

MRI Acquisition

DWI images have been acquired on a research-dedicated 3T Philips Achieva located at the Cross Cancer Institute. The relevant DWI acquisition parameters for full brain coverage are: single-shot echo planar imaging with a SENSE factor of 2, 60 2.3 mm thick slices with no gap, field-of-view = $220 \times 220\ \mathrm{mm}^2$, 2.3 mm^3 isotropic resolution, echo time = 88 ms, repetition time = 8.8 s, 2 averages, acquisition time = 5 min, diffusion sensitivity $b = 1000 s/\mathrm{mm}^2$, and 15 diffusion-sensitizing gradient directions. In addition, a 3-dimensional isotropic T1-weighted image depicting the tumor is also acquired at 3T with $1 \times 1 \times 1\ \mathrm{mm}^3$ resolution in 5.5 min for anatomical comparison and co-registration with the 1.5T images. Routine MRI scans (T1 pre- and post-contrast, T2, FLAIR) are all acquired on the clinical 1.5T Philips scanner as part of the patient's standard follow-up. The resolution of DWI data is $128 \times 128 \times 60$ and the resolution of T2 data is $512 \times 512 \times 21$.

6.3.2 Data Pre-Processing and Validation Procedure

Any proposed model needs to be properly evaluated before being generally accepted. This fact is more important for the clinical case where we are dealing with patients' health. The main goal of our proposed models is to find the tumor invasion margin. We cannot use any direct method to evaluate our mathematical models since the invasion margin is not observable in any of the current imaging techniques. Instead, we have the sequence of MRI scans of patients. So to validate our models on patient data, we choose an initial time point in patient's image sequences and assume that the visible growth in the subsequent times occurs over the invisible but already-infiltrated regions at the initial time.

Fig. 6.6 shows an overview of the growth *validation* system. We simulate a growing tumor from the initial time, *time1*, to approximately its size at a reference subsequent scan, named *time2*, and then compare the result of our model with the actual growth. One should notice that this scheme is different from an actual growth model in a way that the real growth *time* is not important here and the only important factor is the size of the tumor.

We use the first or second DTI scans after treatment as *time1* image to minimize the effect of radiation treatment on the result. The starting growth volume is the manually segmented visible high signal on FLAIR, T2, or DWI-b0, which is the non weighted scan of DWI images that has the same properties as a regular T2 image. This region contains tumor and associated edema. The tumor and edema of *time2* data should also be segmented. To compare the simulation result with the actual result, we need to register the time point scans into the same coordinate system. A proper registration process is difficult due to the mass effect that usually happens between the two scans. In Section 6.3.2, we explain different registration systems we used to minimize this problem. Another pre-processing step is tensor extraction and transformation. To implement any diffusion based growth model, we need to compute water diffusion tensors (DTI) from DWI data and then transform DTI to tumor diffusion tensors (TDT). After the pre-processing steps are properly done, we can then run

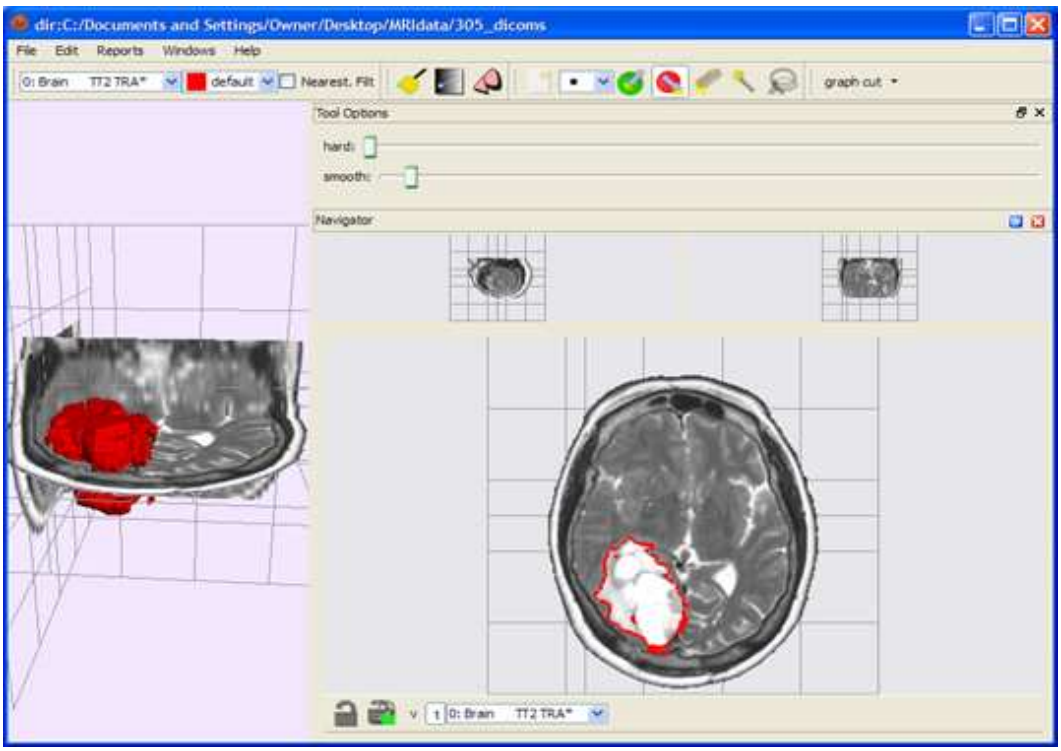

Figure 6.7: A segmented tumor and the segmentation tool

the simulation on the data. We run three different simulations on each patient data; the non-isotropic diffusion model, the geodesic distance model and the isotropic diffusion model, which corresponds to the usual 2cm uniform Euclidean growth model. Finally, we compare the actual growth with the simulation results of each model to see how well they fit. The comparison is done in two different ways: visual comparison, which shows how reasonable the result looks, and numerical comparison, which provides statistical measures. The next three sections will give more details about the pre-processing steps: segmentation, registration and tensor extraction.

Segmentation

For the validation procedure and for initializing the growth simulation, the area of tumor cells visible in the MRI data has to be segmented. The region containing the tumor and its associated edema is the high signal area visible in FLAIR, T2, or DWI-b0 data. We did all segmentations with a semi-automatic tool developed in our lab by Birkbeck et al. [8]. In addition to the tumour region, growth barriers (ventricular system, falx cerebri and tentorium cerebelli), which are also required by the growth prediction model, are manually delineated using the same software. An expert radiation oncologist validated all segmentations. Figure 6.7 shows one sample of a segmented tumor.

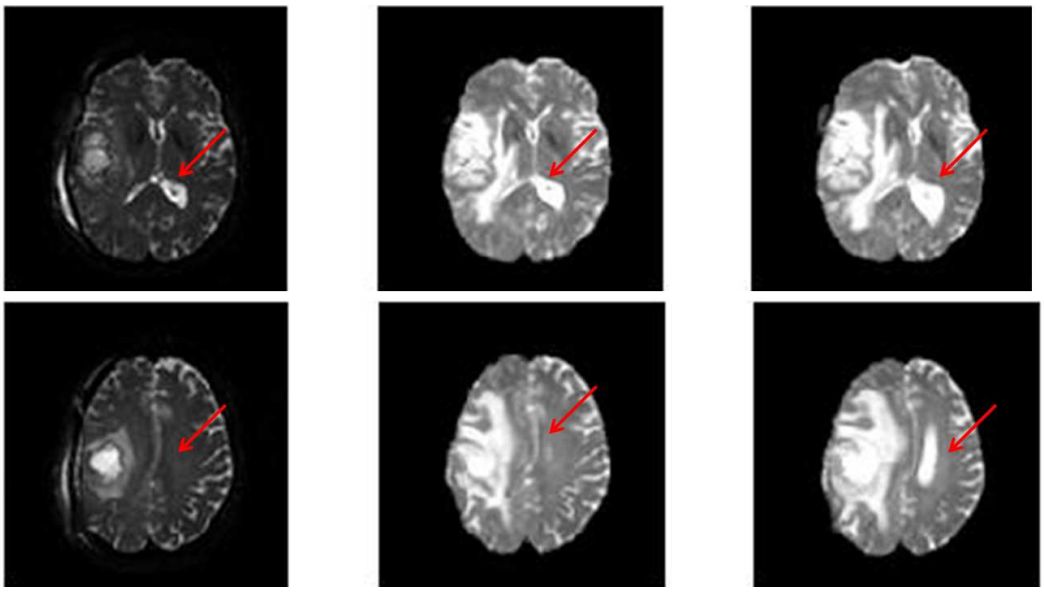

Figure 6.8: Result of applying affine and nonlinear registration between two time scans of the same patient. Each row shows a different slice of the 3D brain volume. Left column: *time 1* scan of the patient, Middle column: *time 2* scan after both affine and nonlinear registration, Right column: *time 2* scan after only affine registration. Notice how results improve if both methods of registration are applied.

Registration

Image registration refers to automatic methods that align two or more images using a warp function. This warp defines how pixels/voxels from one image map into the space of the other image such that they become as similar as possible. Warps can be either global, which define the same transformation (e.g. rotation, translation, affine) for all image pixels or local, in which pixels can move independently. Global warps are used when data from the same patient is needed to be registered. Local warps capture inter-subject variation and are used when data from different patients is registered or when patient data is registered with an atlas.

Our particular registration problem requires that several later MRI scans would be aligned with the initial DTI scan used for growth prediction. While this involves data from only a single patient and normally a global transformation would be enough to align the data, a local non-rigid registration is needed due to the mass effect that deforms parts of the brain around the tumor. This registration is particularly difficult, due to the progression of the tumor that normally grows from one scan to the other. As a result of this growth and its corresponding mass effect, the parts of the image exhibiting incremental growth will no longer match the reference image. Therefore, traditional registration methods cannot be applied directly. Figure 6.8 shows the result of registering two time points once with affine registration and once with both affine and nonlinear registration. The visualized images are 2D slices of a 3D image. The images show that combining the two steps enhances the result (especially in the ventrice area). However, as figure 6.9 shows, if we simulate the growth from *time 1* to

its *time 2* correspondence, we still have the mass effect problem in the ventricle area. For affine and nonlinear registrations, we used FSL tools [26] developed at Oxford (FLIRT for linear and FNIRT for non-linear registration). In this project, we used three different models to combine traditional

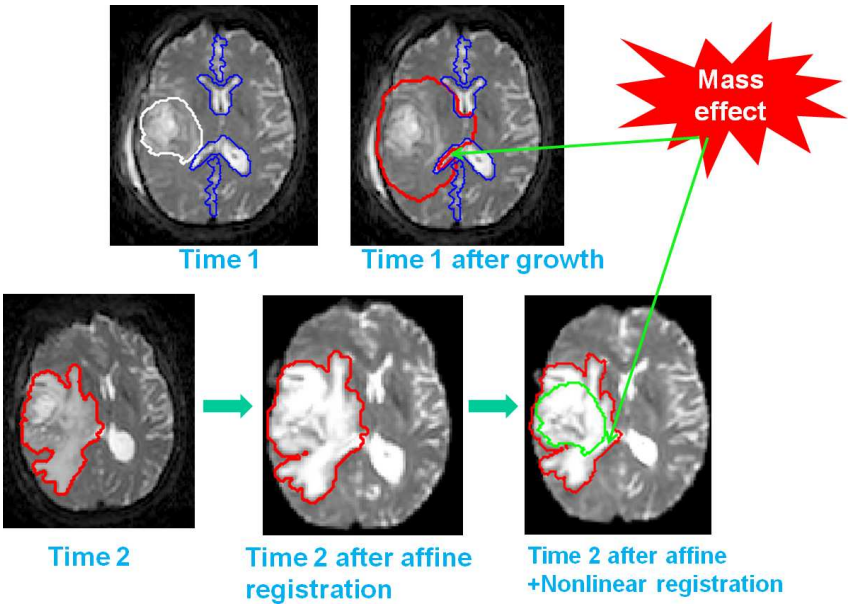

Figure 6.9: Main registration process: The tumor is grown from the *time 1* scan to the size of its volume in *time 2* scan. The *time 2* scan is registered to *time 1* for comparison. Notice that even after both affine and nonlinear registrations, we have the mass effect problem due to the movement in the ventricle regions.

affine and nonlinear registration methods to tackle the mass effect problem.

The first method we used was the simplest one. First, we segmented the tumor at *time 2* and then registered *time 2* with *time 1* with a simple global affine registration. We then applied the same warping function to the segmented area. This warped segmentation corresponded to the edema volume at *time 2* which was used as the reference final volume to be compared with the growth simulation result (see figure 6.10).

In the second method, first we segmented the tumor at *time 2* and then registered *time 2* with *time 1* through a nonlinear registration. Then we segmented the warped image to extract the reference edema volume of *time 2*. This method has two advantages: first the nonlinear registration is used instead of a simple affine one, which tackles the deformations much better. Second, the final volume is segmented after registration, therefore it is more homogenous. The problem with this model is the necessity of two segmentations of the *time 2* data, which is not practical. The first segmentation is needed for correct nonlinear registration and the second one is needed to extract the edema volume. For correct non-linear registration we masked edema label (*time2*) and the generated growth label (*time1*) because those regions contain abnormalities which cannot be incorporated in the registration score. Figure 6.11 shows the comparison between this method and the first method. The two rows show different slices of the same brain volume. In the first column, we see the *time 1* scan of the

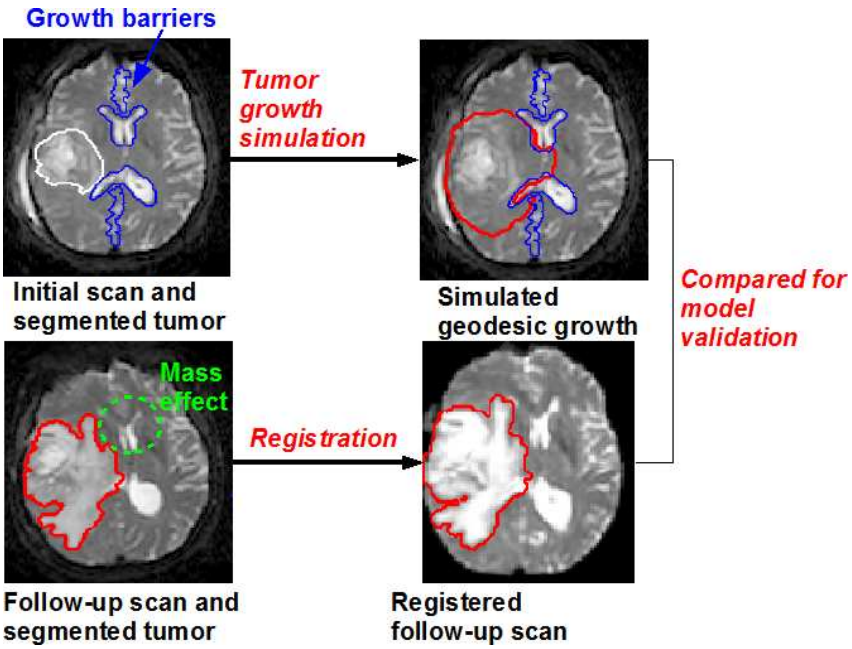

Figure 6.10: Simple growth system using only affine registration. The tumor is grown from the *time 1* scan to the size of its volume in *time 2* scan. The *time 2* scan is registered to *time 1* for comparison. Notice how the affine registration fails in solving the mass effect problem.

image. There is no tumor in the visualized slices at *time 1*. The second column shows the *time 2* scans after applying both affine and nonlinear registration. As we see, aside from the tumor area the rest of the images match. The blue line is the result of applying the second method of segmentation-registration with two steps of segmentation. Notice how well it fits the tumor boundaries. Red line shows the result of the first method of registration, which is far from the registered boundaries.

In the last model, which is the most complicated one, we did the registration in the opposite direction (*time 1* with *time 2*). In this sequence, we first segmented the edema at *time 2* and then registered image of *time 2* with *time 1* through an affine registration. We then applied the same warping function to the segmented area to find the size of the final edema volume. Then we simulated the growth from *time 1* to the defined size and masked it on *time 1* image. Finally, we registered the masked *time 1* image to the original *time 2* and compared the result. Although in the beginning we thought that this model would result better, it was not better in practice. In figure 6.12, we demonstrate this registration and validation system.

A reliable method of registration can greatly improve the validation result. With a problematic registration, we cannot verify what portion of the dissimilarity of the final simulation result is due to the registration and what portion is because of the growth model itself. Although our proposed methods can reduce the registration problem, they were suboptimal. The problem is due to the nonlinear registration. The global registration can easily be decoupled from the nonlinear registration and estimated separately. Nonlinear registration is still an open problem in literature. We recommend the

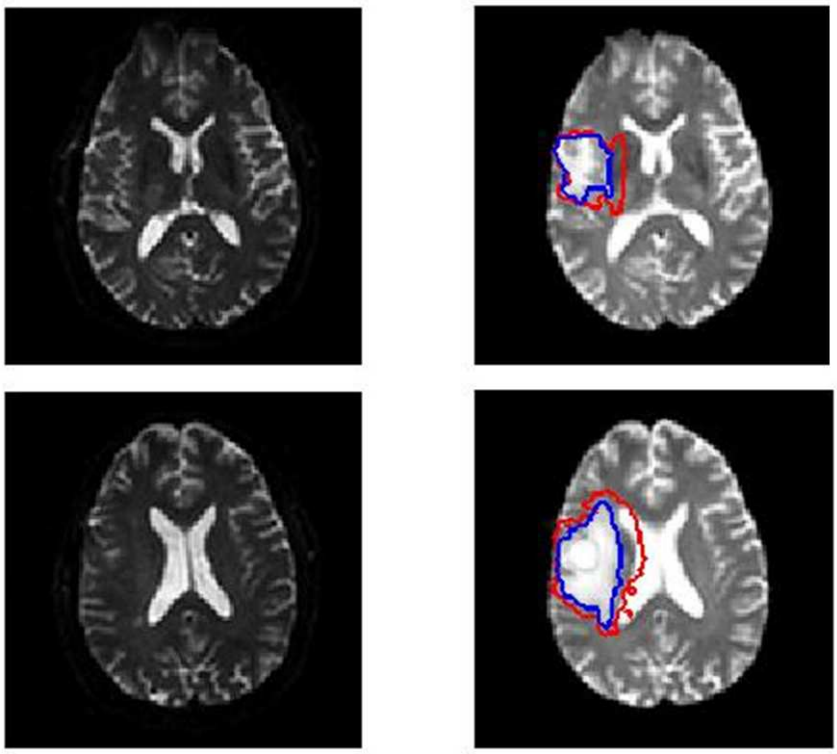

Figure 6.11: The comparison between first and second combination methods of registration. The two rows show different slices of the same brain volume. First column: *time 1* scan of the image. There is no tumor in these visualized slices of *time 1*. Second column: shows the *time 2* scans after applying both affine and nonlinear registration. Aside from the tumor area, the rest of the two images match together. The blue line is the result of applying the second method of segmentation-registration with two steps of segmentation. Notice how well it fits the tumor boundaries. Red line shows the result of the first method of registration and it is far from the registered boundaries.

development of a more reliable nonlinear registration method to enhance the validation procedure as a future work. We therefore propose to incorporate the non-linear mass effect into a global affine registration algorithm that correctly aligns patient time scans.

Tensor Extraction

We tested different tensor processing tools to extract the tensor data from 15 diffusion-weighted images on a voxel-by-voxel basis. The three tools we tested were ExploreDTI [25], MedInria [50] and FSL [26]. The extracted data at each voxel include three eigenvalues that measure diffusion rates along ($\lambda 1$) and across ($\lambda 2$, $\lambda 3$) the fiber length and three eigenvectors reflecting the primary directions of the diffusion ellipsoid. The eigenvalues are then used to calculate the average apparent diffusion coefficient, known as the mean diffusivity (MD), and the fractional anisotropy (FA). Figure 6.13 shows an example of MD and FA map in the left and middle columns respectively. Figure 6.13-right shows the corresponding color-coded map representing the white matter tract directionality, where red identifies left/right tracts, blue identifies superior/inferior tracts, and green identifies

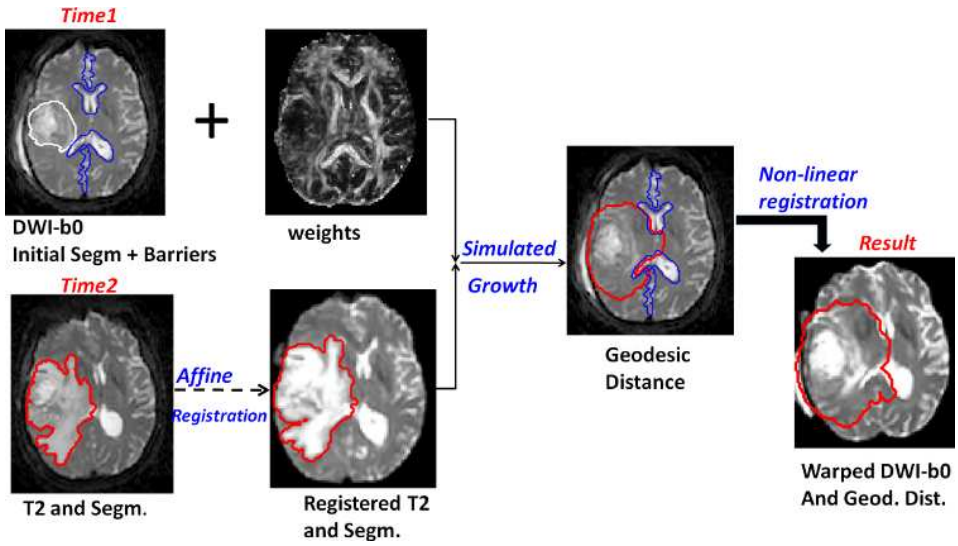

Figure 6.12: The third method of registration + validation system: In this method, the simulated growth result at *time 1* is nonlinearly registered with *time 2*. The key point is that masking the tumor needed for registration is done after the growth.

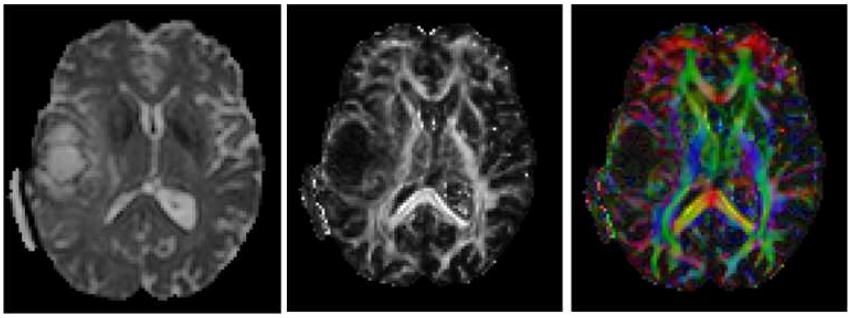

Figure 6.13: An example of DTI statistical data. Left: Mean Diffusivity (MD), Middle: FA map, Right: color-coded map representing the white matter tract directionality, where red identifies left/right tracts, blue identifies superior/inferior tracts, and green identifies anterior/posterior tracts

anterior/posterior tracts.

Our final choice was ExploreDTI with post processing for correcting eddy current distortions that are unique for each diffusion-encoding direction and also for correcting the motion distortion. MedInria gave incorrect results on real data; the tensors were not extracted for the whole image creating holes in some part of the image. FSL tool extracted the tensors completely and the eddy current distortion correction was embedded in the tool. However the visual comparison of FA maps obtained with ExploreDTI and FSL tool (both after distortion correction) shows that ExploreDTI results are better (See Figure 6.14). To check the correctness of extracted tensors, we ran the fiber tracking algorithm on them. A successful fiber tracking process means that the tensor direction and orientations are correct. Figure 6.15 shows an example of tensor extraction. The left image shows the FA map of the image. The middle image visualizes diffusion tensors in ellipsoid format on the FA map. Finally,

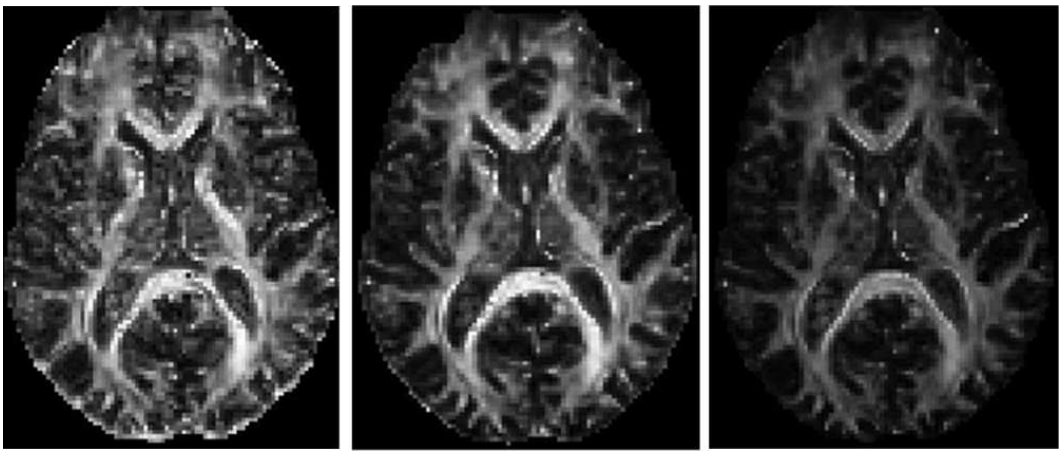

Figure 6.14: FA maps obtained with three different tensor extraction tools. Left: ExploreDTI without distortion correction. Notice the noise of the image especially in edges of the brain. Middle: ExploreDTI after distortion correction. Right: FSL tool after distortion correction.

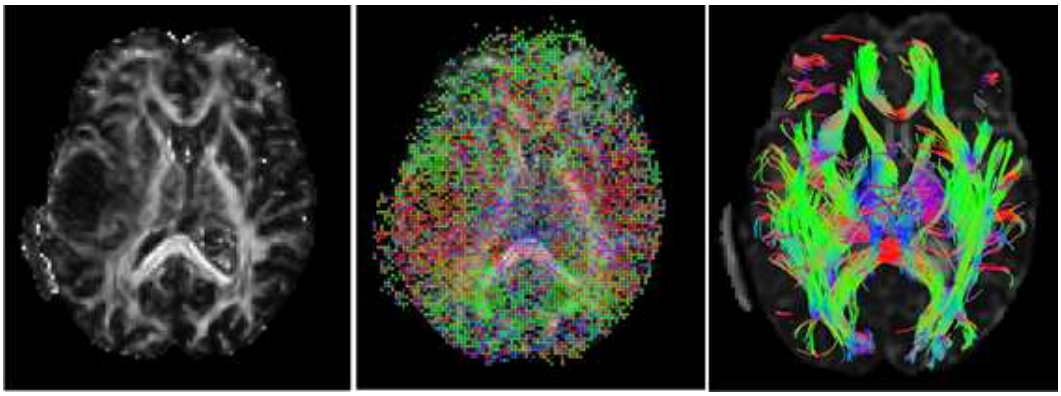

Figure 6.15: An example of tensor extraction. Left: Sample FA map of the image. Middle: Diffusion tensors visualized in ellipsoid format plotted on the FA map. Right: Fiber tracts made from the extracted tensor data; complete tracts show the correctness of the tensor data.

the right image shows the result of applying a fiber tracking algorithm on the extracted tensor data. The complete fiber tracts show the correctness of the tensor extraction process. For fiber tracking we used ExploreDTI [25].

After this point, the water tensors are extracted (DTI) and they are further processed to make tumor diffusion tensors (TDT) as shown in Figure 6.16. Different models can be used for this mapping as described in Chapter 4. We used a linear function FA values for the mapping function described in Section 4.3. After this post processing step, tumor diffusion tensor data is ready to be used in the growth simulation process.

6.3.3 Visual Results

Although as we explained in Section 6.3.1, currently 69 patients are enrolled in data acquisition process in Cross Cancer Institute, by the time this project was done, we had only access to 24

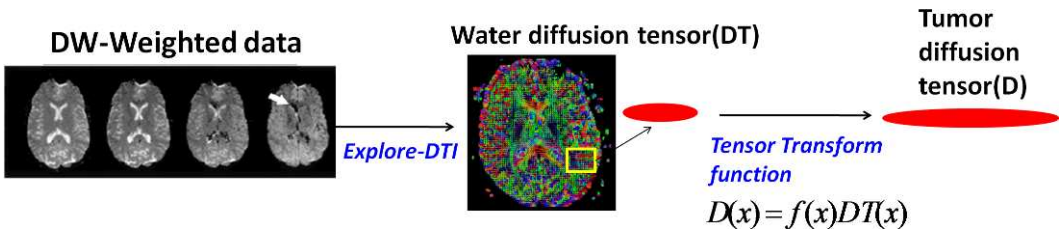

Figure 6.16: Post processing on diffusion tensors: water diffusion tenors (DTI) are processed to make tumor diffusion tensors (TDT)

datasets of patients with high grade glioma. From these 24 sets, only 8 data showed tumor growth after treatment. For the rest of patients, either their short life duration did not allow capturing further scans or the size of edema decreased due to the applied therapy. Therefore, after pre-processing these 8 datasets as explained in Section 6.3.2, we simulated the growth models on them. The three growth models we used were the non-isotropic diffusion model, the geodesic distance model and the isotropic diffusion model. Fig. 6.17 shows the comparative results of real growth from a subsequent registered *time 2* scan with geodesic and Euclidean growth simulation from *time 1* scan. Since all scans are registered in the same space, the growth simulated with one of the mathematical models can be compared with the actual tumor growth segmented in the reference follow-up scan. The results show that where the tensor values are less noisy, the geodesic distance model can track the path of fibers and therefore matches tumor growth, as opposed to when using the Euclidean model. Notice how in the last row of figure 6.17, the Euclidean distance has not reached the shown tumor slice while the geodesic distance correctly models the growth. In figure 6.18, the three models are compared together.

6.3.4 Numerical Results

To numerically compare our diffusion based models with the conventional Euclidean model, we propose three types of comparative measures. To understand these measures, we denote the volume grown by the mathematical model with A and the one actually observed with B, see Figure 6.19.

1. Precision: The number of correctly grown cells by A divided by the total number of grown cells by A. This score penalizes parts that are incorrectly grown by the mathematical model (false positives) but does not penalize parts where the follow-up scan shows growth not predicted by the model (false negatives). In other words, the score penalizes parts that are going to be unnecessarily radiated.

2. Recall: The number of correctly grown cells by A divided by the total number of grown cells in B. This score penalizes parts where the mathematical model fails to predict growth (false negatives) and does not penalize parts that are incorrectly shown as growth (false positives). It therefore penalizes parts that are supposed to be treated but are not (according to the predicted model).

3. Jaccard: The number of correctly grown tumor cells by A divided by the total number of grown cells in A and B. This score penalizes both false positives and false negatives.

4. F-measure: The harmonic-mean of Precision and Recall that accounts both measures and is defined as

$$F = \frac{2PR}{P+R}$$

where P and R respectively show precision and recall.

The calculated values of comparative measures are given in Table 6.1. As mentioned in Section 6.3.2, for reducing the mass effect problem, we applied non-linear registration to warp data from *time1* into the space of *time2*. For some patients, we have follow-up DTI scans and for others we have only follow-up T2 scans. The T2-DWI registration adds another step of registration to the whole process. So the numerical results on these datasets are less reliable and we did not include them in Table 6.1. Numerical results show that on average the scores of simulated growth using the geodesic distance is always better compared to the Euclidean distance. Especially for the case of Jaccard score which is the strictest one, it shows an improvement of $5-10\%$. Also the F-measure which is the harmonic-mean of Precision and Recall is about 5% better in geodesic model compared to Euclidean model. Diffusive model only results better for the precision measure and the two other measures are worse compared to the Euclidean distance model. The reason is that we have applied linear post processing on the tensors that makes the diffusive model unstable. If we use DTI tensors as TDT tensors without any post processing, the anisotropic diffusive model remains stable. However, the numerical measures show little improvement for both anisotropic diffusive and geodesic methods compared to Euclidean method. We implemented both methods with Matlab and the simulation time of each method is about 15 minutes. In order to increase the simulation speed, we can use narrow band and implicit finite difference method and also implement the methods in C programming environment rather than Matlab.

Patient Number		1	2	3	4	*mean*
Jaccard Score (%)	*Aniso. Diffusive*	37	65	51	59	56.5
	Geodesic dist.	65	75	72	65	69.3
	Euclidean dist.	60	66	66	62	63.5
Precision (%)	*Aniso. Diffusive*	86	90	91	74	82.3
	Geodesic dist.	72	81	81	73	76.8
	Euclidean dist.	68	80	80	75	75.8
Recall (%)	*Aniso. Diffusive*	39	70	54	74	61.8
	Geodesic dist.	87	91	87	73	84.5
	Euclidean dist.	84	81	79	78	80.5
F-measure (%)	*Aniso. Diffusive*	54	79	68	74	68
	Geodesic dist.	79	86	84	73	80
	Euclidean dist.	75	80	79	76	78

Table 6.1: Numerical scores of comparing registered ground truth of *time2* with geodesic and Euclidean and diffusive simulated growth of time1

6.4 Conclusion

In this chapter, we first tested the stability of different numerical methods proposed to solve second order parabolic diffusion equation. The results show that not all of the proposed numerical methods in the literature are stable on diffusion data. For the parabolic diffusive equation, certain conditions on the diffusion tensor should be considered to keep the model spatially stable. The geodesic distance model is better since it is unconditionally spatial stable and only its discrete time stability needs to be considered.

We also evaluated the proposed growth models on the real patient DTI data. The evaluation process includes pre-processing, simulation and comparison. In the pre-processing step, which includes segmentation, registration and tensor extraction, the data is prepared for the simulation process. In the simulation step, each of simulation models is applied to data to grow the tumor from its actual location at the initial time to its actual size at the subsequent time. Finally at the comparison step, the results of different models are visually and numerically compared to together. Comparative results between real growth in subsequent scans and simulated growths prove that the use of the geodesic distance model can improve radiation therapy treatment compared to the currently used Euclidean distance. Diffusive model only gives better result if the real tensors satisfy the stability condition.

Comparison between non-isotropic diffusion model and geodesic models show several benefits in using the Geodesic distance model. First, numerically stable and reliable methods are available for solving its final PDE, while this is not true for non-isotropic diffusion model. Second, the output of simulation is the distance from initial position not, tumor cell density. This distance corresponds to the delineation area that is visually observed in the image. So no approximation is needed to extract the tumor invasion margin from tumor cell densities. Another advantage is that it can be efficiently implemented using narrow-band methods. Finally, the visual and numerical results on real patients are better with the geodesic model. The only problem of the geodesic model is that it can only model the diffusion part. Proliferation and therapy effects are not considered in the formulation. Reformulation of the geodesic model to include therapy and proliferation effects can be considered as a future work. One can also argue that the invasion margin is the result of diffusion not proliferation, so considering proliferation is not necessarily needed in finding the invasion margin.

Another source of problem in this project was the registration process. Although the non-linear registration used between *time1* and *time2* to numerically validate results solves the problem of mass effect to a good extent, it cannot solve it completely. Hence, the error in the non-linear registration produces inaccuracies. As a future work, for better non-linear registration in the presence of mass effect we can incorporate a mechanical model into the registration (similar to [52]).

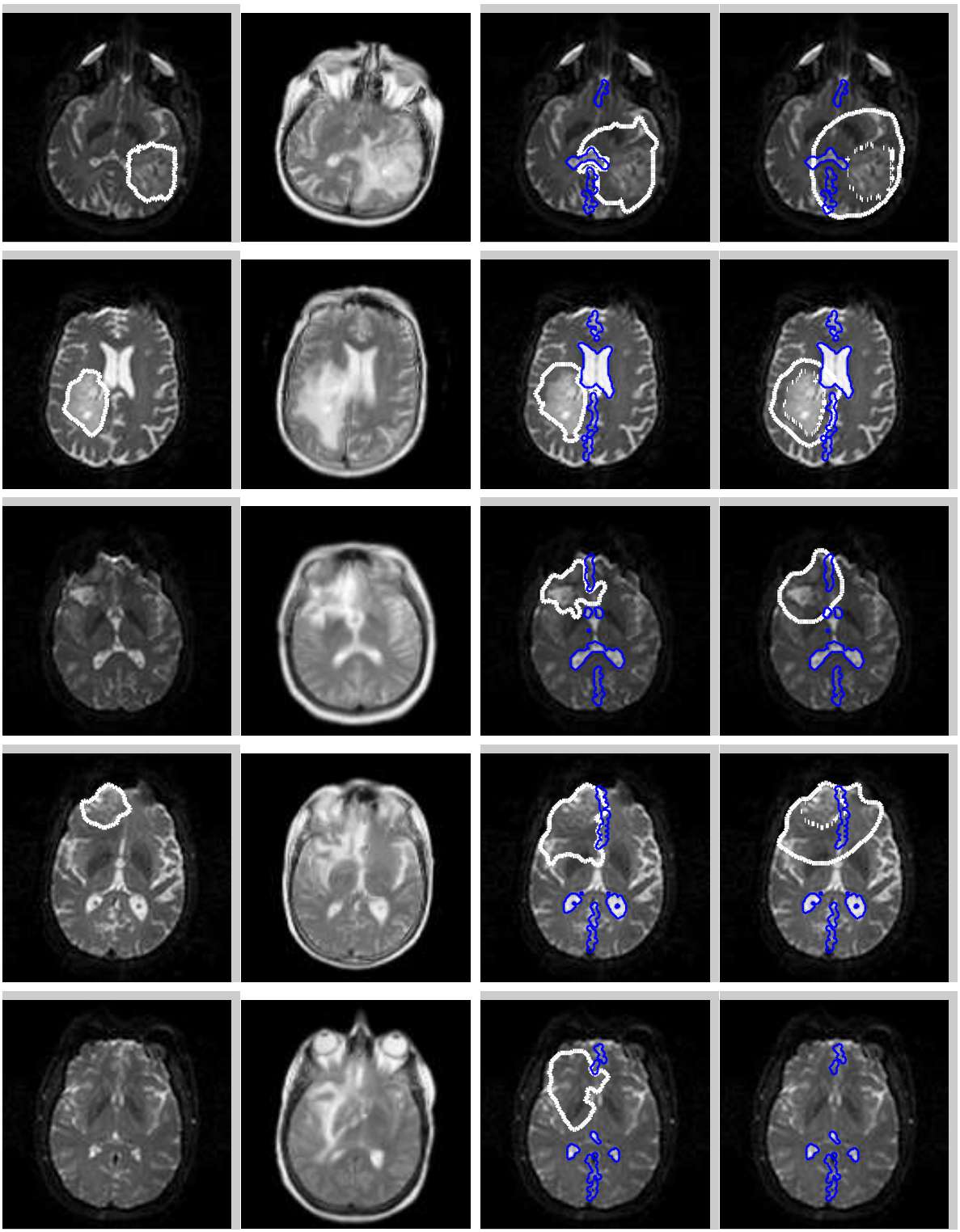

(a) Patient at *time1* Initial segm. (b) Patient at *time2* (c) Geod. dist. (d) Euclid. Dist.

Figure 6.17: Comparative results for 8 different patients of Geodesic (c) and Euclidean (d) simulated growth starting from segmented tumor at *time1* (a) and linearly registered followed up scans at *time2* (MRI-T2 or DWI) (b). Barriers are shown in blue. Notice how in the example from the last row the Euclidean distance has not reached the showed tumor location while the Geodesic distance correctly shows the growth.

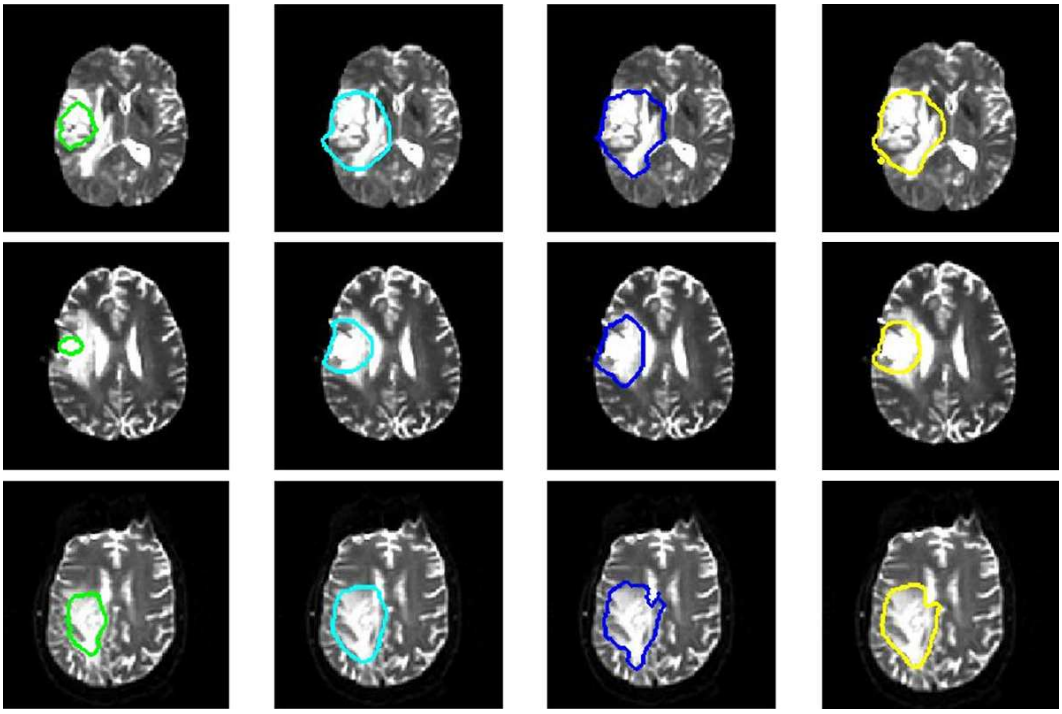

Figure 6.18: Comparative results for 8 different patients. All the images show the registered *time2* scans. The plotted contours from left to right show respectively: Initial tumor volume, Euclidean, Geodesic and anisotropic diffusive simulations result.

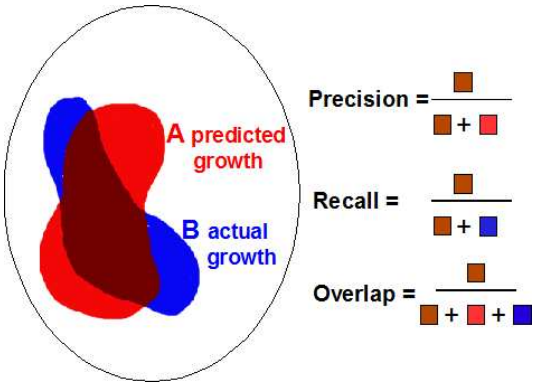

Figure 6.19: The growth predicted by the mathematical model is compared to the actual growth observed in a follow-up scan. Precision penalizes parts that are unnecessarily radiated (false positives), recall penalizes parts that should have been treated but are not (false negatives), and overlap, being the most strict, penalizes both types of mistakes

Chapter 7

Conclusion

This thesis addresses the problem of detecting the tumor invasion margin beyond the visible boundary from CT or MRI data. We proposed two models to detect the glioma brain tumor invasion margin: the anisotropic diffusive model and the geodesic distance on the Riemannian manifold of brain fibers. These models use the diffusion tensor imaging data to locate the invasion of the tumor in the direction of brain fiber tracts. The models were tested on several real patients data sets obtained from Cross Cancer Institute [15] and a DTI atlas. In contrast to previous works in the area of brain tumor growth prediction, instead of using tensor data from a registered brain atlas tensors, we used real, patient specific tensors obtained under a regular clinical protocol at the Cross Cancer Institute. Comparative results between real growth in follow up scans and simulated growth based on geodesic, anisotropic diffusive and Euclidean distance models show that DTI based models can estimate an invasion margin that more accurately reflects the visible tumour growth seen in later images, when compared to the original 2cm Euclidean distance model. This is of great clinical importance since a correct definition of invasion margin can improve the effectiveness of radiation therapy given to patients.

In this thesis, we also theoretically analyzed and experimentally evaluated the stability of the various numerical implementations of the two models on both synthetic and real data. Another contribution of the thesis was extending a stable 2D method of discretizing the anisotropic diffusive equation to 3D. Both mathematical models result in Partial Differential Equations (PDEs) which has to be numerically solved. In this thesis, we analyzed and evaluated the numerical aspects including stability and consistency of several finite difference methods used to solve these PDEs. To achieve a stable 3D method for discretizing the anisotropic diffusion equation that is a second order parabolic equation, we extended a stable 2D model to 3D.

7.1 Future Work

The main goal of this project is to find the correct margin of tumor occult cells attacked by radiation therapy. This helps to control glioma tumors more effectively. Based on the fact that tumor

cells diffuse in the same direction as water molecules, we used mathematical models to locate the tumor invasion in the direction water molecule motion. The information of water molecule motion is obtained using diffusion weighted MRI technique. The access to actual patient MRI and DTI data enables us evaluate our models on accurate and personalized information of white matter tracts, without requiring additional registration steps. The previous proposed brain tumor growth models were tested either on synthetic data or on one or two real data which cannot be a good measure of how the model works in reality. To validate a model of this type, much more patient data is needed. No brain tumor growth model has yet been generated and verified on a large set of patient DTI data. We have hitherto tested on 8 datasets, but the continuous collection of patient data at the Cross Cancer Institute will allow testing and validation of models on much larger number of patients. The access to this data set enables us to be the first to test realistic diffusion-based and transport-based tumor growth models on a large collection of patient DTI. The dataset preparation includes segmentation of tumor in all time scans, segmenting the barriers, registering time scans together and tensor extraction. We prepared the dataset of 8 patients that showed actual growth in time; the same preparation can be done for all patients. This will allow us to analyse the models of tumors in different locations of the brain, with different shapes and rates of growth.

Another shortcoming of the so far proposed models is in extracting TDT (Tumor Diffusion Tensor) from DTI. As we discussed in this thesis, the so far proposed techniques to extract TDT are rather heuristic. Their main idea in constructing the TDT is to assign isotropic diffusion to gray matter and anisotropic diffusion to white matter, with the greatest diffusion along the direction of the fiber. A future enhancement can be modeling the TDT in the form of a tumor flow map estimated from tumor growth observations of patients from several MRI scans. We already have a large collection (more than 200) of such MRI scans that would provide a good base for building a realistic model for TDT. In addition, this learned tumor flow map would also reveal brain barriers that inhibit tumor spread.

A main source of error in the validation procedure is caused by the approximate registration of several time scans of the patient data. Although the non-linear registration used between *time1* and *time2* can decrease the mass effect problem to a good extent, it cannot solve it completely. Deriving a better registration method that explicitly models the tumor mass effect can therefore improve the validation system. A proposed registration technique in the presence of mass effect, incorporates a mechanical model into the registration.

Finally, as shown by Painter [58], anisotropic diffusion might not be the optimal mathematical formulation of the cell migration process, which can be better modelled using a transport equation. So developing new mathematical models that use the full potential of DTI imaging instead of the current reaction-diffusion based models can increase the accuracy of tumor geometry and treatment margin prediction.

Bibliography

[1] Giese A., L. Kluwe, B. Laube, H. Meissner, M.E. Berens, and M. Westphal. Migration of human glioma cells on myelin. *Neurosurgery*, 38:755–764, 1996.

[2] D.C. Alexander. *An Introduction to Computational Diffusion MRI: the Diffusion Tensor and Beyond*. Springer Berlin Heidelberg, 2006.

[3] R.P. Araujo and D.L.S. McElawin. A history of the study of solid tumour growth: the contributions of mathematical modeling. *Bull. Math. Biol.*, 66:1039–1091, 2004.

[4] PJ. Basser. Inferring microstructural features and the physiological state of tissues from diffusion-weighted images. *NMR Biomed*, 8:333–344, 1995.

[5] PJ. Basser and C. Pierpaoli. Microstructural and physiological features of tissues elucidated by quantitative-diffusion-tensor. *MRI. J Magn Reson*, pages 209–219, 1996.

[6] M.S. Berger and C.B. Wilson. *The Gliomas.* Philadelphia, WB Saunders Company, 1999.

[7] D.L. Bihan, E. Breton, D. Lallemand, P. Grenier, E. Cabanis, and M. Laval-Jeantet. Mr imaging of intravoxel incoherent motions: Application to diffusion and perfusion in neurologic disorders. *Radiology*, 161(2):401–407, 1986.

[8] N. Birkbeck, D. Cobzas, M. Jagersand, A. Murtha, and T. Kesztyues. An interactive graph-cut method for brain tumour segmentation. In *Workshop on Applications of Computer Vision (WACV)*, 2009.

[9] P.K. Burgess, P.M. Kulesa, J.D. Murray, and E.C. Alvord. The interaction of growth rates and diffusion coefficients in a three-dimensional mathematical model of gliomas. *J. Neuropath Exp Neuro*, 56:704–713, 1997.

[10] A.C. Burton. Rate of growth of solid tumours as a problem of diffusion. *Growth*, 30:157–176, 1966.

[11] M. Cercignani and M.A. Horsfield. The physical basis of diffusion-weighted. *MRI. J. Neurol.*, 186(1):S11.S14, 2001.

[12] M.A.J. Chaplain. Mathematical modeling of angiogenesis. *J. Neuro Oncology*, 50:37–51, 2000.

[13] O. Clatz, M. Sermesant, P. Bondiau, H. Delingette, S.K. Warfield, G. Malandain, and N. Ayache. Realistic simulation of the 3d growth of brain tumors in MR images coupling diffusion with mass effect. *IEEE Transactions on Medical Imaging*, 24(10):1334–1346, 2005.

[14] D. Cobzas, P. Mosayebi, A. Murtha, and M. Jagersand. Tumor invasion margin on the riemannian space of brain fibers. In *MICCAI*, 2009.

[15] Cross Cancer Institute. http://www.oncology.med.ualberta.ca/.

[16] G.C. Cruywagen, D.E. Woodward, P. Tracqui, G.T. Bartoo, J.D. Murray, and E.C. Alvord. The modeling of diffusive tumour. *Journal of Biology Systems*, 3:937–945, 1995.

[17] G.C. Cruywagen, DE. Woodward, P. Tracqui, G.T. Bartoo, J.D. Murray, and E.C. Alvord. The modeling of diffusive tumours. *J. Biol. Sys*, 3:937–945, 1995.

[18] L.M. DeAngelis. Brain tumors. *The New England Journal of medicine*, 344:114–123, 2001.

[19] A. Einstein. *Investigations on the Theory of the Brownian Movement*. New York: Dover, 1956.

[20] E.Konukoglu. *Modeling Glioma Growth and Personalizing Growth Models in Medical Images*. PhD Thesis, Universite Nice Sophia-Antipolis, 2009.

[21] B. Engquist and S. Osher. One-sided difference approximations for nonlinear conservation laws. *Mathematical Computing*, 36:321–351, 1981.

[22] D.L Bihan et al. Diffusion tensor imaging: Concepts and applications. *JOURNAL OF MAGNETIC RESONANCE IMAGING*, 13:534546, 2001.

[23] H.A. Levine et al. Mathematical modeling of the onset of capillary formation initiating angiogenesis. *J. Math. Biol.*, 42:195–238, 2001.

[24] R. Stupp et al. Radiotherapy plus concomitant and adjuvant temozolomide for glioblastoma. *Engl J Med*, 352(10):987–996, 2005.

[25] ExploreDTI. http://www.exploredti.com/.

[26] FSL. tools http://www.fmrib.ox.ac.uk/fsl/.

[27] E.C. Halperin, G. Bentel, E.R. Heinz, and P.C. Burger. Radiation therapy treatment planning in supratentorial glioblastoma multiforme: an analysis based on post mortem topographic anatomy with ct correlations. *Int J Radiat Oncol Biol Phys*, 17:1347–50, 1989.

[28] R.H. Hashemi and W.O. Bradley. *MRI.The Basics*. Lippincott Williams and Wilkins, Philadelphia, 2004.

[29] H. Hatzikirou, A. Deutsch, C. Schaller, M. Simon, and K. Swanson. Mathematical modelling of glioblastoma tumor developement: A review. *Mathematical Models and Methods in Applied Sciences*, 15(11):1779–1794, 2005.

[30] M.T. Heath. *Scientific Computing, An Introdutory Survey*. McGraw-Hill, 2002.

[31] F.H. Hochberg and B. Slotnick. Neuropsychologic impairment in astxocytoma survivors. *Neurology*, 30:907–911, 1980.

[32] C. Hogea, F. Abraham, G. Biros, and C. Davatzikos. A framework for soft tissue simulations with applications to modeling brain tumor mass-effect in 3d images. In *MICCAI*, 2006.

[33] C. Hogea, C. Davatzikos, and G. Biros. Modeling glioma growth and mass effect in 3d MR images of the brain. In *MICCAI*, 2007.

[34] C. Hogea, C. Davatzikos, and G. Biros. Brain-tumor interaction biophysical models for medical image registration. *SIAM J. SCI. COMPUT.*, 30(6):793825, 2008.

[35] C. Hogea, C. Davatzikos, and G. Biros. An image-driven parameter estimation problem for a reactiondiffusion glioma growth model with mass effects. *Journal of Mathematical Biology*, 56:793825, 2008.

[36] S. Jbabdi, E. Mandonnet, H. Duffau, L. Capelle, K.R. Swanson, M. Pelegrini, R. Guillevin, and H. Benali. Simulation of anisotropic growth of low-grade gliomas using dif. tensor imag. *Magnetic Resonance in Medicine*, 54:616–624, 2005.

[37] N. Savill K. J. Painter and E. Shochat. *Computing evolutions in brain tumours*. Submitted Article, 2005.

[38] A. R. Kansal, S. Torquato, E. A. Chiocca, and T. S. Deisboeck. Emergence of a subpopulation in a computational model of tumor growth. *J. Theor. Biol.*, 207:431–441, 2000.

[39] E. Konukoglu, O. Clatz, P. Bondiau, H. Delingette, and N. Ayache. Extrapolating tumor invasion margins for physiologically determined radiotherapy regions. In *MICCAI*, 2006.

[40] E. Konukoglu, O. Clatz, B.H. Menze, Marc-André Weber, B. Stieltjes, E. Mandonnet, Hervé Delingette, and N. Ayache. Image guided personalization of reaction-diffusion type tumor growth models using modified anisotropic eikonal equations, Accepted to be published 2009.

[41] T. Kuroiwa, M. Ueki, Q. Chen, H. Suemasu, I. Taniguchi, and R. Okeda. Biomechanical characteristics of brain edema: the difference between vasogenic-type and cytotoxic-type edema. *Acta Neurochir Suppl*, 60:158–61, 1994.

[42] K. Stelios Kyriacou, Christos Davatzikos, S. James Zinreich, and R. Nick Bryan. Nonlinear elastic registration of brain images with tumor pathology using a biomechanical model. *IEEE TRANSACTIONS ON MEDICAL IMAGING*, 18(7):580–592, 1999.

[43] C. Lenglet. *Geometric and Variational Methods for Diffusion Tensor MRI Processing*. PhD Thesis, INRIA Sophia Antipolis, 2006.

[44] C. Lenglet, R. Deriche, and O. Faugeras. Diffusion tensor magnetic resonance imaging brain connectivity mapping. In *INRIA*, 2003.

[45] C. Lenglet, R. Deriche, and O. Faugeras. Inferring white matter geometry from diffusion tensor MRI: Applic. to connectivity mapping. In *MICCAI*, 2004.

[46] LONI. atlases http://www.loni.ucla.edu/atlases/.

[47] N. V. Mantzaris, S. Webb1, and H.G. Othmer. Mathematical modeling of tumor-induced angiogenesis. *Journal of Mathematical Biology*, 49:111–187, 2004.

[48] W.V. Mayneord. On a law of growth of jensen's rat sarcoma. *Am. J. Cancer*, 76:841–846, 1932.

[49] D.L.S. McElwain and L.E. Morris. poptosis as a volume loss mechanism in mathematical models of solid tumor growth. *Math. Biosciences*, 39:147–157, 1978.

[50] MedINRIA. http://www-sop.inria.fr/asclepios/software/medinria/.

[51] A. Mohamed and C. Davatzikos. Finite element modeling of brain tumor mass-effect from 3d medical images. In *MICCAI*, pages 400–408, 2005.

[52] A. Mohamed, E.I. Zacharaki, D. Shen, and C. Davatzikos. Deformable registration of brain tumor images via a statistical model of tumor-induced deformation. *Medical Image Analysis*, 10(5):752–763, 2006.

[53] J. Murray. *Mathematical Biology II: Spatial Models and Biomedical Applications*. Springer-Verlag, 3rd edition, 2003.

[54] J.D. Murray. *Mathematical Biology*. Springer-Verlag, Heidelberg, 1989.

[55] L. O'Donnell, S. Haker, and C.F. Westin. New approaches to estimation of white matter connectivity in diffusion tensor MRI: Elliptic PDEs and geodesics in a tensor-warped space. In *MICCAI*, 2002.

[56] M.E. Orme, M.A.J. Chaplain, D.L.S. McElwain, and L.E. Morris. A mathematical model of the first steps of tumour-related angiogenesis: Capillary sprout formation and secondary branching. *J. Math. Appl. Med. Biol.*, 13:73–98, 1996.

[57] S. Osher and R.P. Fedkiwh. *Level Set Methods and Dynamic Implicit Surfaces*. Springer, New York, 2002.

[58] K.R. Painter. Modelling cell migration strategies in the extracellular matrix. *Journal of Mathematical Biology*, 58:511–544, 2009.

[59] L. Preziozi. *Cancer modelling and simulation*. Chapman & Hall, CRC Mathematical Biology and Medicine Series, 2003.

[60] J.H. Rees, J.G. Smirniotopoulos, RV. Jones, and K. Wong. Glioblastoma multiforme: radiologicpathologic correlation. *Radiographics*, 16(6):14131438, 1999.

[61] S. Sanga, H.B. Frieboesb, X. Zheng, R. Gatenbyc, E.L. Bearerd, and V. Cristin. Predictive oncology: A review of multidisciplinary, multiscale in silico modeling linking phenotype, morphology and growth. *NeuroImage*, 37:S120–S134, 2007.

[62] J.G. Smirniotopoulos, F.M. Murphy, E.J. Rushing, J.H. Rees, and J.W. Schroeder. From the archives of the afip: patterns of contrast enhancement in the brain and meninges. *Radiographics*, 27(2):525551, 2007.

[63] E.O. Stejskal and J.E. Tanner. Spin diffusion measurements: spin echoes in the presence of a time-dependent field gradient. *Journal of Chemical Physics*, 42:288–292, 1965.

[64] K.R. Swanson, E.C. Alvord, and J.D. Murray. A quantitative model for differential motility of gliomas in grey and white matter. *Cell Proliferation*, 33:317–329, 2000.

[65] K.R. Swanson, E.C. Alvord, and J.D. Murray. Virtual brain tumors (gliomas) enhance the reality of medical imaging and highlight inadequacies of current therapy. *British Journal of Cancer*, 85:14–18, 2002.

[66] K.R. Swanson, E.C. Alvord, and J.D. Murray. Virtual resection of gliomas: Effects of location and extent of resection on recurrence. *Math. Comp. Model*, 37:11771190, 2003.

[67] K.R. Swanson, R.C. Rostomily, and E.C. Alvord. A mathematical modelling tool for predicting survival of individual patients following resection of glioblastoma: a proof of principl. *British Journal of Cancer*, 98:113 119, 2008.

[68] P. Tracqui, G.C. Cruywagen, D.E. Woodward, G.T. Bartoo, J.D. Murray, and E.C. Alvord. A mathematical model of glioma growth: the effect of chemotherapy on spatio-temporal growth. *Cell Prolif*, 28:17–31, 1995.

[69] D.S. Tuch. Mapping cortical connectivity with diffusion mri. In *ISBI*, page 392.394, 2002.

[70] K.E. Wallner, J.H. Galicich, G. Krol, E. Arbit, and M.G. Malkin. Patterns of failure following treatment for glioblastoma multiforme and anaplastic astrocytoma. *International Journal of Radiation Oncology, Biology, Physics*, 16:1405–1409, 1989.

[71] R. Wasserman, R. Acharya, C. Sibata, and K.H. Shin. A patient-specific in vivo tumor model. *Mathematical Biosciences*, 136(2):111–140, 1996.

[72] J. Weickert. *Anisotropic Diffusion in Image Processing*. ECMI Series, Teubner-Verlag, Stuttgart, 1998.

[73] D.E. Woodward, J. Cook, P. Tracqui, G.C. Cruywagen, J.D. Murray, and E.C. Alvord. A mathematical model of glioma growth: the effect of extent of surgical resection. *Cell Prolif*, 29:269–288, 1996.

[74] M. Wurzel, C. Schaller, M. Simon, and A. Deutsch. Cancer cell invasion of normal brain tissue: Guided by prepattern. *J. Theor. Med*, 6:21–31, 2005.